3D Extended-Range Particle-Localization Microscopy Using Airy-Beam-Based Point-Spread Functions

Yongzhuang Zhou

School of Physics & Astronomy
College of Science & Engineering
University of Glasgow

Submitted in fulfillment of the requirements for the degree of
Doctor of Philosophy

August 2019

To my mother.

Declaration

I hereby declare that except where specific reference is made to the work of others, the contents of this dissertation are original and have not been submitted in whole or in part for consideration for any other degree or qualification in this, or any other university. This dissertation is my own work and contains nothing which is the outcome of work done in collaboration with others, except as specified in the text and Attributions.

Yongzhuang Zhou
August 2019

Attributions and Publications

Attributions

Some of the work in this thesis involve collaboration with other people, and their contributions are as follows:

In the *in vivo* experiment, preparation of the zebrafish sample including the microinjection was performed by Dr Vytautas Zickus. The visualization of the light sheet images was also with his help. All the imaging and data analysis were conducted by the author. Note that animals used in this work were maintained according to the Animals (Scientific Procedures) Act 1986, United Kingdom.

The 'twin-Airy' project was proposed by Dr Paul Zammit, while the analysis and optical implementation were conducted by the author. The simulation of the 'double-helix' phase mask was with the help of Dr Zammit as well.

In the Cramer-Rao lower bound analysis, the 'tetrapod' phase mask was obtained with the help of Dr Guillem Carles.

The time-resolved traction-force microscopy is an ongoing collaboration with professor Manuel Salmeron-Sanchez's group and the samples are provided by his research assistants and students: Dr Oana Dobre, Dr Sara Trujillo Munoz and Ana San Felix Garcia-Obregon.

Some of the figures were reproduced from other publications with permission; some were reproduced under Creative Commons licence. These are all clearly stated as 'adapted/ reproduced from' followed by their corresponding references in the figure captions.

Publications

Some of the work presented in this thesis have been published or are being considered for publication, which are listed below.

Journal articles

- Y. Zhou, P. Zammit, G. Carles, and A. R. Harvey, "Computational localization microscopy with extended axial range," Opt. Express 26, 7563-7577 (2018).
- Y. Zhou, V. Zickus, P. Zammit, J. M. Taylor, and A. R. Harvey, "High-speed extended-volume blood flow measurement using engineered point-spread function," Biomed. Opt. Express 9, 6444-6454 (2018).
- Y. Zhou, M. Handley, G. Carles and A. R. Harvey, "Advances in 3D single particle localization microscopy," APL Photonics 4, 060901 (2019). Featured as Cover Article.
- Y. Zhou, P. Zammit, V. Zickus, J. M. Taylor, and A. R. Harvey, "Twin-Airy point-spread function for extended-volume localization microscopy," In review.

Conference proceedings

- Y. Zhou, P. Zammit, and A. R. Harvey, "3D microfluidic particle image velocimetry with extended depth-of-field and a single camera," in Imaging and Applied Optics 2016, OSA Technical Digest (online) (Optical Society of America, 2016), paper JT3A.40.
- S. H. Wilson, Y. Zhou, P. Zammit, and A. R. Harvey, "Enhanced computational imaging for microendoscopy," in Imaging and Applied Optics 2017, OSA Technical Digest (online) (Optical Society of America, 2017), paper JTu5A.19.
- Y. Zhou, P. Zammit, V. Zickus, G. Carles, J. Taylor, and A. R. Harvey, "Video-rate 3D particle tracking with extended depth-of-field in thick biological samples," in Imaging and Applied Optics 2017, OSA Technical Digest (online) (Optical Society of America, 2017), paper CM3B.3.
- Y. Zhou, V. Zickus, A. R. Harvey, and P. Zammit, "Double-cubic point spread function for 3D extended-depth localization microscopy," in Imaging and Applied Optics 2018, OSA Technical Digest (Optical Society of America, 2018), paper CM3E.4.

Acknowledgements

I am extremely grateful to my supervisor Professor Andrew Harvey for his continuous guidance and generous support during my PhD study. His optimistic attitude towards research and life always inspires me.

Many thanks to my fellow officemates in the Imaging Concepts Group, it has been an honor to work with them. In particular, I wish to thank Dr Paul Zammit and Dr Guillem Carles for their mentorship and help during the early stages of my PhD and for those inspiring discussions. I would like to thank Dr Jonathan Taylor for his guidance on the *in vivo* experiments and for his helpful input into several of my works. I am also grateful to Dr Pavan Chandra Konda and Dr Vytautas Zickus for their oftentimes help throughout my study.

I thank all my friends who made my stay in Glasgow delightful. I must express my gratitude to my wife Jing for her wholehearted support and my son Arran for the happiness he brings to me. I am deeply indebted to all my family members who care and support me spiritually throughout my life.

Abstract

The precise localization of point emitters in optical microscopy has revolutionized our ability to super resolve subcellular structures beyond the diffraction limit and to study fundamental biological dynamics through single-molecule tracking. It also found its applications on a larger scale in blood-flow characterization, traction-force microscopy and microfluidic research including lab-on-chip experiments. However, traditional optical microscopy is typified by a restrictively small depth of field, i.e. the operable range in the axial direction is severely limited by diffraction to a thin layer in contrast to the relatively large field of view in the *xy* directions. This precludes the probing of three-dimensional (3D) behaviors of the sample. A number of techniques have emerged recently for 3D point localization, typically exploiting characteristic axial variations in the optical point-spread function (PSF) to deduce the axial coordinate of the emitter. However, existing approaches suffer from limitations such as small depth ranges, low optical throughput, complicated implementations or degraded performance in presence of overlapping PSFs.

In this work, the lateral translation of the Airy beam is exploited to encode the emitters' axial coordinates and two novel approaches, namely the Airy-CKM (i.e. complementary kernel matching) and the twin-Airy techniques, are reported for 3D point-localization microscopy. The following advantages are clearly demonstrated: (1) The Airy-beam-based PSFs yield diffraction-free propagation, i.e. little diffractive spreading, which provides a greater axial range than existing techniques and makes them suitable for imaging thick samples. (2) Deconvolution-based localization algorithms are utilized, allowing for imaging of high emitter densities with overlapping PSFs. (3) The continuous phase profiles used to generate the Airy-beam-based PSFs can be implemented with refractive phase masks, which yield nearly 100% broadband optical throughput avoiding the photon inefficiency of spatial light modulators. (4) The simplicity in implementations (especially the twin-Airy technique) makes them applicable to most fluorescence microscopes.

A statistical comparison to existing methods is performed by calculating their Cramer-Rao lower bounds, where the proposed approaches compare favorably to the state-of-the-art. The reported techniques are demonstrated to *in vivo* measurement of blood-flow dynamics in zebrafish embryos, which, to the best of the author's knowledge, is the first the application of pupil-engineered PSFs to hemodynamic measurements. In addition, time-resolved traction-force microscopy will be discussed briefly as an ongoing work.

Table of contents

List of figures

List of tables

Abbreviations

Acronyms / Abbreviations

AB-PSF Airy-beam point-spread function

BFP Back-focal plane

CCV Common cardinal vein

CKM Complementary-kernel matching

CRLB Cramer-Rao lower bound

DH-PSF Double-helix point-spread function

DL-PSF Diffraction-limited point-spread function

DOF Depth of field

dSTORM Direct stochastic optical reconstruction microscopy

FEP Fluorinated ethylene propylene

FOV Field of view

GFP Green fluorescent protein

LSFM Light-sheet-based fluorescence microscopy

MLE Maximum-likelihood estimation

MTF Modulation-transfer function

NA Numerical aperture

OTF Optical-transfer function

PBS Phosphate-buffered saline

PIV Particle-image velocimetry

PR-MLE Phase-retrieval-based maximum-likelihood estimation

PSF Point-spread function

PTV Particle-tracking velocimetry

ROI Region of interest

SB-PSF Self-bending point-spread function

SLM Spatial light modulator

SNR Signal-to-noise ratio

SPIM Selective-plane-illumination microscopy

TA-PSF Twin-Airy point-spread function

TCD Two-channel disparity

TFM Traction-force microscopy

TLD Two-lobe disparity

WFC Wavefront coding

Chapter 1

Introduction

Point emitters are widely used in science and engineering as tracers of three-dimensional velocity fields, indicators of mechanical forces or labels of biomedical structures. Precise localization of microscopic or nanoscopic point emitters has aroused broad interest over the past decade, particularly because of its applications in life sciences to super-resolution microscopy[1–3] and single-molecule tracking experiments[4–6], which have revolutionized our ability to resolve subcellular structures beyond the diffraction limit and to study fundamental biological dynamics such as folding and unfolding of proteins, protein-DNA interaction and dynamic processes on cell membranes[7]. Moreover, it found its application on a larger scale in blood-flow characterization[8–10], traction-force microscopy (TFM)[11, 12] and microfluidic research[13] including lab-on-chip experiments[14, 15].

Optical microscopes are the most commonly used equipment to achieve high-resolution imaging of microstructure or high precision localization of point emitters. However, traditional microscopy is typified by a restrictively small depth of field (DOF), i.e. the operable range in the axial direction is severely limited by diffraction to a thin layer in contrast to the relatively large field of view (FOV) in the *xy* directions. This precludes the probing of three-dimensional (3D) behaviors of the sample: For high numerical aperture (NA) systems (e.g. 1.4NA), the depth range achieved by conventional approaches is usually limited to below a micron which is smaller than the dimension of a cell (normally several microns to tens of microns); and for relatively low NA systems (e.g. 0.4 NA), the achievable axial range is normally below 10 µm which precludes imaging of thick samples such as the vasculature of a zebrafish, a cell-seeded hydrogel to study 3D traction forces and many microfluidic devices. Although the axial range can be extended by reducing the NA of the imaging system, this will inevitably lower the spatial resolution and the optical throughput, resulting in a degraded localization precision. In fact, precise localization of point emitters throughout a useful depth range of the third dimension has remained, until recently, a significant challenge.

A number of 3D techniques have emerged in recent years in the field of point-localization microscopy, typically exploiting characteristic axial variations in the optical point-spread function (PSF) which carries information of the defocus of the point source and allows its z (axial) coordinate to be deduced. The most promising approaches are the pupil-engineered PSFs (or engineered PSFs) which employ a specific amplitude or phase modulation at the pupil plane to yield PSFs with desired properties; some of these PSFs can additionally enable localization through an axial range that exceeds the conventional diffraction-limited system. For example, the double-helix PSF (DH-PSF)[16] consists of two main lobes which rotate about a common center with changing defocus; the self-bending PSF (SB-PSF)[17] displays two main lobes diverging with changing defocus. However, these techniques suffer from their own limitations as will be further discussed in the literature review and have not been reported for an operable axial range larger than 3 µm. The tetrapod PSF encodes the depth information in its changing intensity profile and can work with much larger depth ranges, however, the maximum-likelihood estimation (MLE) required to extract the z coordinate is computationally expensive and suffers from degraded precision in the existence of overlapping PSFs.

In this thesis, the depth-dependent translation of the Airy beam is investigated and utilized to encode the emitters' axial coordinates and two novel approaches, namely the Airy-CKM (i.e. complementary kernel matching) and the twin-Airy techniques, are reported for 3D point-localization microscopy. Compared to the existing approaches, the following advantages are clearly demonstrated: (1) The Airy-beam-based PSFs yield diffraction-free propagation, which provides a greater axial range than most existing techniques and makes them pertinent for imaging thick samples. (2) Deconvolution-based localization algorithms are utilized, allowing for imaging of high emitter densities with overlapping PSFs. (3) The continuous phase profiles used to generate the Airy-beam-based PSFs can be implemented with refractive phase masks, which yield nearly 100% broadband optical throughput and avoid the photon inefficiency of spatial light modulators (SLM). (4) The simplicity in their implementations (especially the twin-Airy technique) makes them applicable to most fluorescence microscopes. Comparisons are made to state-of-the-art techniques in terms of axial range and localization precision by means of Cramer-Rao lower bound (CRLB) simulations, and experimental assessment is also performed by imaging quantum dots. In addition to the emphasis on low-photon-level scenarios, this work explores the possible applications to relatively low numerical aperture experiments such as *in vivo* measurement of blood flow dynamics in zebrafish and time-resolved TFM.

1.1 Thesis outline

This chapter gives a general background of particle-localization microscopy, an outline of this thesis, a literature review on several 3D point-imaging techniques, and the theoretical background of pupil-engineering microscopy.

In chapter 2, the z-dependent image translation associated with the Airy-beam PSF (AB-PSF) is investigated theoretically and by simulation, following which a new approach is proposed for 3D point-localization microscopy, termed as the Airy-CKM. A deconvolution-based algorithm is utilized to deduce emitters' xyz coordinates. Proof-of-concept experiments are discussed at the end of this chapter including assessment of the depth-dependent translation in the AB-PSF and its extended depth range, and measurement of velocity field in microfluidics. In addition, the possibility of 3D point localization using a single intact AB-PSF will also be discussed.

In chapter 3, another Airy-beam-based technique is introduced for 3D localization microscopy over extended depth range, namely the twin-Airy PSF (TA-PSF) which enables deducing of emitters' 3D coordinates using a single imaging channel and thus provides more simplicity than the Airy-CKM technique. The design of the twin-Airy phase mask is firstly discussed, followed by the 3D localization algorithms for the TA-PSF. It is then demonstrated for localization of quantum dots on a $60\times$, 1.4NA system to assess its performance for low-photon-count experiments such as single-molecule tracking. To better compare the performance of the proposed the Airy-beam-based techniques with the existing techniques, their statistically best precision, the CRLBs, are calculated. Technical issues including pupil-size mismatching and phase-mask misalignment will also be discussed in this chapter.

Chapter 4 describes the application of the Airy-CKM technique and the TA-PSF to the *in vivo* measurement of blood flow in zebrafish embryos, starting with a short introduction to the existing methods for *in vivo* blood-flow characterizations. Details of the sample preparation will be described, especially the microinjection of tracer beads in the zebrafish blood circulation. It will be shown that the Airy-beam-based techniques enable high-speed extended-volume imaging of blood-flow dynamics, and the tracer trajectories can be well reconstructed using the algorithms described in the previous chapters. At the end of this chapter, 3D images of the zebrafish blood vessels obtained from a modified selective-plane-illumination microscopy (SPIM) system will be presented as a validation of the reconstructed tracer trajectories.

Chapter 5 summarizes this work by revisiting the main achievements of this PhD and by discussing the remaining challenges in the experiments and several aspects to be improved. Some ongoing and future work will also be discussed including the time-resolved TFM and extended-depth super-resolution microscopy. Some preliminary results will be presented for the traction-force experiment.

1.2 Literature review

This section will start with an overview of the available 3D imaging modalities for general objects and then focus on 3D point imaging approaches that enable single-shot detection, in contrast to the conventional scanning-based approaches. The mainstream techniques lie in the engineered PSFs, which employ engineering of the pupil function to alter the PSF and to encode the axial information in various ways. Based on different depth-encoding methods, these techniques can be divided into three groups: namely rotation-based techniques, translation-based techniques and MLE-based techniques (z information is encoded in the varying intensity profile). While the review here is more qualitative, a quantitative comparison will be made in chapter 3.

1.2.1 Scanning-based techniques

Confocal microscopy

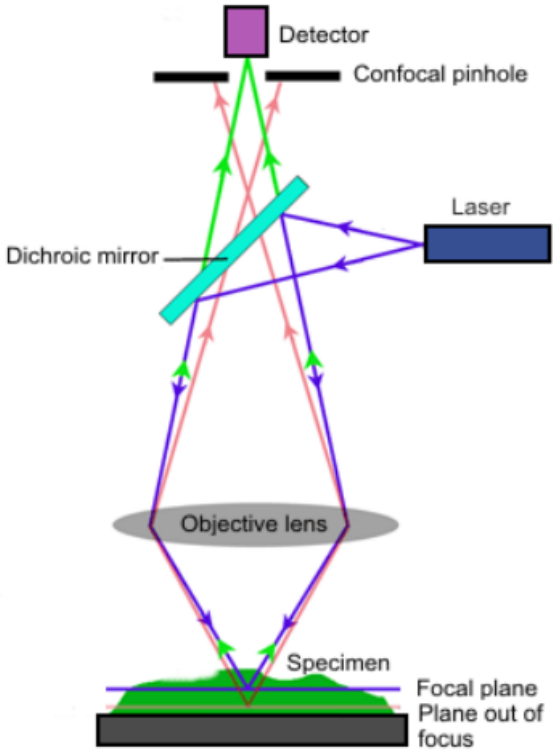

Fig. 1.1 Confocal microscope configuration. Image reprinted from Stanciu et al.[18], material under the Creative Commons Attribution 3.0 License.

A widely used 3D imaging technique is confocal microscopy. It dates back to 1950s[19] but is still very popular in the scientific and industrial communities, especially in life science with applications ranging from cell biology and genetics to microbiology and developmental biology. Of particular interest to this thesis, confocal microscopy is intensively used for tracking of indicator particles in TFM.

The principle of confocal microscopy differs from conventional microscopes with wide-field epi-illumination in two ways: Firstly, the illumination beam is focused to a diffraction-limited spot rather than uniformly illuminating the whole sample; secondly, a pinhole aperture is placed at the image plane conjugate to the point illumination which stops most of the out-of-focus light as shown in Fig. 1.1. This improves the contrast in the image and enhances the optical resolution especially in the z direction, at the cost of the optical throughput and imaging speed. The focused illumination is scanned through the sample volume to reconstruct an image in a point-by-point manner. Various ways have been exploited to improve the scanning speed such as the spinning disk, however, the scanning nature of confocal microscopes introduces artefacts in the image as the voxels are not exposed at the same time; thus, making it unsuitable for imaging transient phenomenon.

Two-photon scanning

Two-photon excitation microscopy is another way to achieve 3D optical sectioning of the sample. It is similar to confocal microscopy in the sense that they both use focused laser beams scanned within the sample, but it offers several advantages. Two-photon microscopy employs the absorption of two photons in order to excite a molecule from the ground state to the excited state. Unlike conventional fluorescence microscope where excitation wavelength is shorter than emission, a two-photon excitation process absorbs two long-wavelength photons and emits at a shorter wavelength[21] (Fig. 1.2a). The longer wavelength excitation (usually in infrared) has less toxic effect in biological samples and minimizes scattering and absorption in the tissue, thus provides deeper penetration. The two-photon absorption is a non-linear process and only happens near the focus of the objective due to the required high photon density and flux. Therefore, it yields a more compact excitation volume especially in the z direction (Fig. 1.2b) and reduced photo-bleaching in the sample compared to the confocal microscopy. Besides, the pin hole detection is not required, which gives high efficiency in light detection. Note that the high photon density needed for two-photon absorption often requires high power short pulsed laser to be used.

Overall, the advantages of two-photon microscopes make it suitable for observing thick samples and living cells or tissues; it is, however, also point-scanning-based imaging technique, which is not capable of imaging transient phenomenon and dynamic processes as the voxels are not exposed at the same time. The longer wavelength used for excitation also makes its lateral resolution slightly worse than confocal microscopy when the same fluorophore is considered[22].

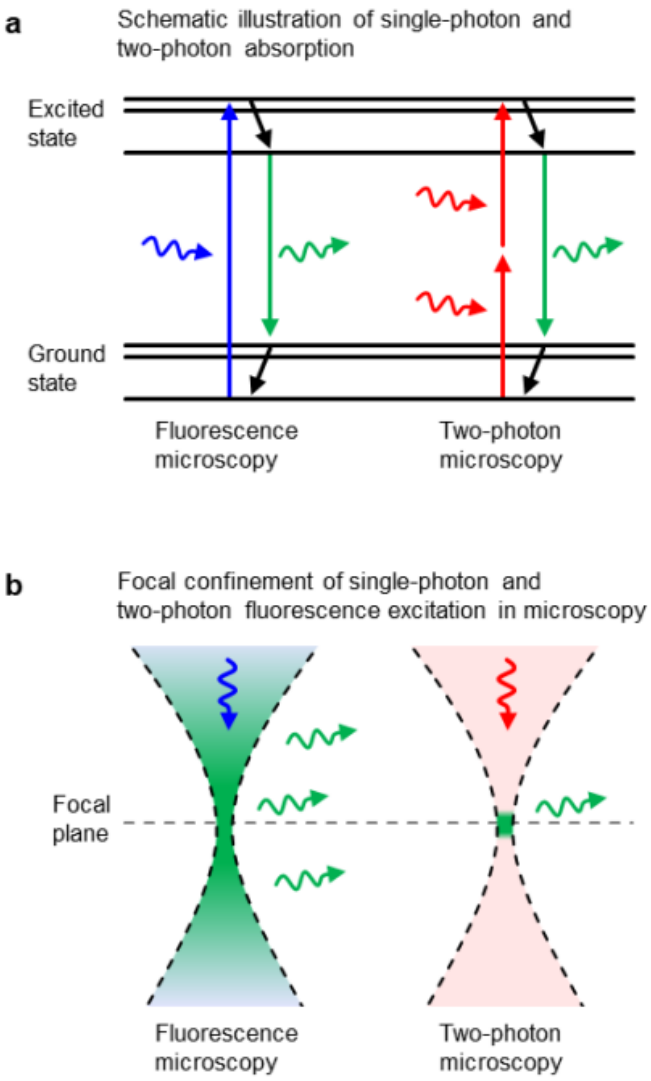

Fig. 1.2 (a) Illustration of the single-photon and two-photon absorption process for fluorescence excitation. (b) Spatial confinement of fluorescence signal generation in conventional fluorescence microscopy and two-photon microscopy. Image adapted from ref[20].

Light-sheet microscopy

An alternative way to achieve optical sectioning and thus 3D imaging is the light-sheet-based fluorescence microscopy (LSFM), which employs a thin sheet of light from the side of the sample as illumination (Fig. 1.3)[24]. Various configurations have been reported namely the SPIM or digital scanned laser light-sheet fluorescence microscopy.

Compared to confocal or two-photon microscopy, LSFM provides a greatly increased acquisition speed as an entire *xy* plane is detected per frame. A one-dimensional *z* scan of the sample is usually performed to reconstruct a volume image of the sample, compared to the three-dimensional point-scanning in confocal or two-photon methods. In LSFM, only the in-focus object plane is illuminated, which significantly reduces the back-

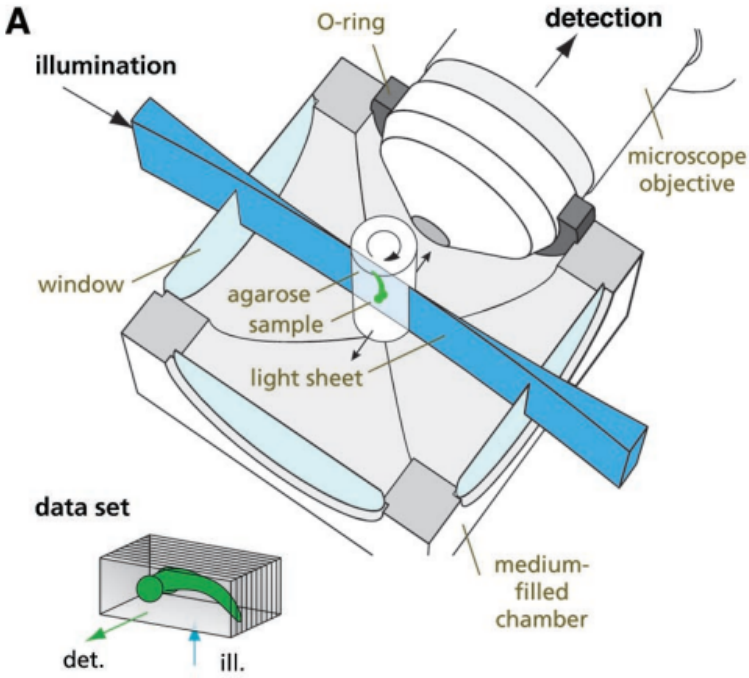

Fig. 1.3 Light-sheet microscope configuration. A cylindrical lens focuses the excitation light to a thin light sheet that is perpendicular to the optical axis of the detection objective. Image reprinted with permission from Huisken et al.[23]. Copyright 2004, American Association for the Advancement of Science.

ground fluorescence; and no light is rejected by a pinhole, providing an improved optical throughput. This results in a much higher signal-to-noise ratio (SNR) than confocal-based techniques and also reduced photobleaching and photodamage to the sample. LSFM has found its wide applications in developmental biology, three-dimensional cell cultures and biophysics[25].

However, the axial resolution of LSFM is limited by the thickness of the light sheet. A thinner light sheet gives a better axial resolution at the cost of a more limited FOV. Also, the z scan still stops it from imaging transient phenomenon and dynamic process. Although the recent work by Zickus and Taylor[26] uses high-speed multi-depth acquisition combined with digital synchronization with the beating heart to enable 3D measurement of the blood-flow dynamics in zebrafish, the multi-depth acquisition limits the axial component of the flow field to be deduced.

1.2.2 Single-shot approaches for 3D point localization

The above mentioned techniques are for 3D imaging in general (not limited to point sources but also for spatially extended objects), this section will focus on 3D point-imaging techniques. Especially, the emphasis is on ‘single-shot’ techniques which encode emitters’ 3D positions in a single detected image, eliminating the need for scanning and allowing high-speed acquisition. This is important for imaging of dynamic processes

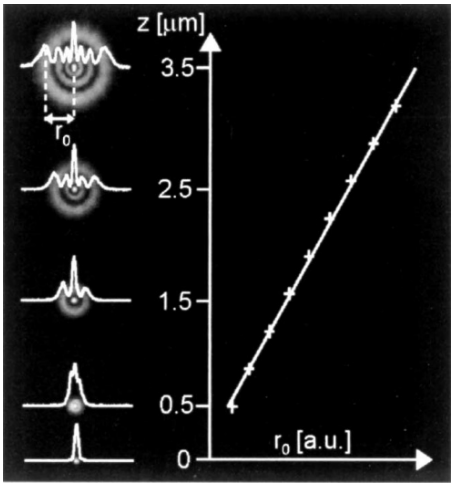

Fig. 1.4 Depth estimation based on the radius of an Airy disk. The radius r_0 of the outermost ring in the images scales linearly with z. Image adapted from ref[27] with permission. Copyright 2003 Optical Society of America.

and for applications like direct stochastic optical reconstruction microscopy (dSTORM) where the emitters are blinking in time.

3D point localization with Airy disks and Multi-focal plane imaging

The 3D coordinates of an emitter can be directly deduced from the conventional diffraction-limited PSF (DL-PSF), by measuring the radius of the Airy disk or by fitting a model to the measured PSF[27–31], as shown in Fig. 1.4. However, the DL-PSF expands rapidly in size as defocus increases, resulting in a decreased SNR at large defocus and thus a very limited depth range. Moreover, the DL-PSF is symmetrical above and below the focal plane, making it difficult to assign a unique z to the emitter position and effectively halving the useful depth range. This precludes its application to imaging thick samples. In addition, the large PSF size also makes it unsuitable for imaging high emitter densities. Note that lower NA can be used to extend the useful depth range, but this will inevitably reduce the number of collected photons, the SNR and thus the localization precision. A lower NA also means a larger PSF profile, which further limits the emitter densities.

The use of multifocal planes can eliminate the above mentioned ambiguity of the DL-PSF and extend the useful depth range. Prabhat et al.[32] first reported a biplane configuration using just two separate levels of defocus. The idea has since been developed into a wider framework, which covers various number of focal planes[33–35]. A model PSF is fit simultaneously to each image, accounting for the fixed level of defocus between each plane. This results in a more precise estimation over a larger depth range. Multifocal plane has been used in 3D super-resolution[36] and imaging of fast intracellular dynamics in live cells[35].

The number of focal planes and the spacing between them factor into the achievable precision and axial range, as well as the consistency over the axial range. Planes which are too close together do not cover a very wide range in z; but if they are too far apart then the localization precision suffers in the case that an emitter lies in the middle. Adding more focal planes can increase the range over which localization precision is consistent, but each added plane decreases the amount of light reaching every detector. The drop in the SNR generally results in a decreased overall localization precision with each added plane[37].

Astigmatic PSF

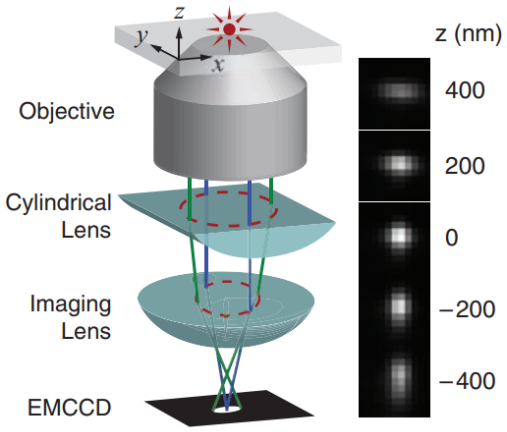

Fig. 1.5 Astigmatic PSF generated using a cylindrical lens. Image adapted from Huang et al.[38] with permission. Copyright 2008, American Association for the Advancement of Science.

One of the earliest single-shot configurations for 3D particle tracking, introduced by Kao et al. in 1994[39], employed an astigmatic PSF by placing a cylindrical lens into the imaging pathway (Fig. 1.5). The transverse dimension and ellipticity of the PSF enable determination of the magnitude and sign of the axial displacement of the emitter from the nominal focus. This technique is one of the most used techniques for 3D particle localization due to its simplicity and low cost in implementation, and has found broad employment, such as in the tracking of individual quantum dots in cells[40], micro-particle-tracking velocimetry (μ-PTV) in microchannel chips and other systems[41–45] and super-resolution microscopy[38, 46–48]. Significant disadvantages, similar to the Airy disks, are that the rapid increase in size of the PSF with the increasing defocus reduces SNR, limiting the achievable depth range and the emitter concentration[42].

Defocusing digital particle-image velocimetry

Particle localization in 3D can also be achieved by triangulation of the three lobes formed when a three-pinhole mask is located close to the pupil of the microscope[49–53]

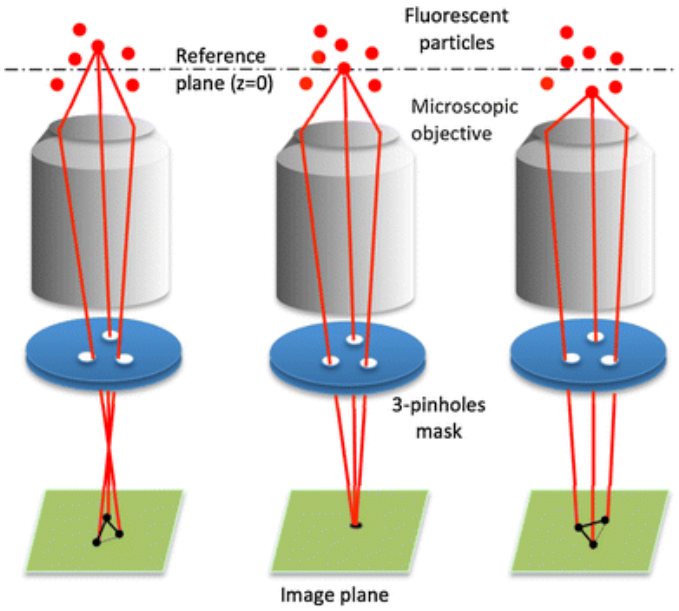

Fig. 1.6 Schematic of particle localization using the three-pinhole mask. Image adapted from ref[49], material under Creative Commons licence CC BY.

(Fig. 1.6). The orientation and scale of the resultant triplet PSF yield the sign and magnitude of the defocus parameter, which is more robust than measuring the ellipticity of an elliptical PSF. This configuration was first realized in measurements of fluid flow in a vortex ring[50] and has recently found uses in 3D flow characterization[49], in sensors for microfluidic devices[54], and in the macroscale for tracking the motion of zooplankton[55]. The use of the pinhole mask in the pupil severely limits the NA of the system however, which in turn lowers the optical throughput, the SNR [42] and precision. The particle concentration is also compromised by the expansion of the triplet PSF at large defocus due to overlap in the three PSF lobes.

Rotating PSFs

The rotating PSFs for depth estimation was first proposed by Greengard et al.[57]. A superposition of five Gauss-Laguerre (GL) modes was used to produce the PSF which continuously rotates around a common center as defocus changes. Such a PSF, however, yields low photon efficiency as large fraction of energy is distributed in the side lobes. Pavani and Piestun further optimized the design to improve the photon efficiency, resulting in the high-efficiency rotating PSF[16, 56]. In this design, they used the rotating PSF in ref[57] as a first estimation and optimize iteratively in spatial domain by maximizing the energy in the main lobes of the PSF; in Fourier domain by making sure the transfer function is phase-only; and in the GL-mode domain by multiplying the GL modal decomposition with a weight function. The optimization process gives rise to an increased photon efficiency and results in 30 times more energy in the main lobes compared to the initial rotating PSF[16], which gives it potential for low-photon-level experiments. This

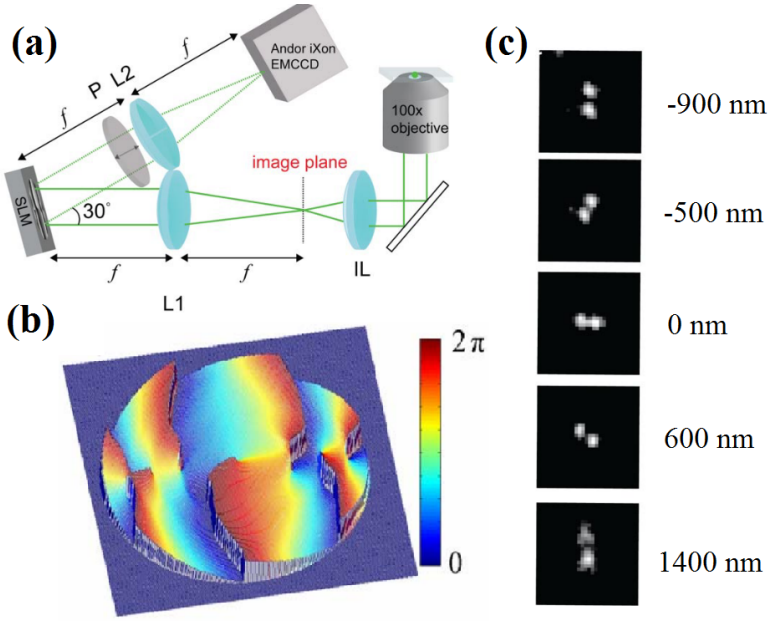

Fig. 1.7 (a) Imaging setup for the double-helix PSF (DH-PSF). The DH phase mask is introduced using a spatial light modulator (SLM) placed at the Fourier plane of a $4f$ system. (b) The DH phase mask profile. (c) Experimental DH-PSFs. Image adapted from Pavani et al.[56] with permission.

PSF was then termed as the 'double-helix PSF' (Fig. 1.7) and used for three-dimensional single-molecule imaging[56].

To avoid the photon inefficiency of an SLM, Grover et al. employed a fabricated phase mask using gray-level lithography[58]. Such a fabricated phase mask avoids the single polarization modulation and high-diffraction-order photon loss of an SLM, yielding a transmission efficiency of 87% which is around twice that of the SLM. It is worth noting that the DH-PSF is perhaps the most widely used 3D localization technique after astigmatism.

Another version of DH-PSF was reported later with the effort to generate the DH-PSF with an analytic expression[60]. The analytic pupil function is formed by a set of vortex singularities distributed on a straight line along a diameter of the pupil, which reduces the PSF design to two parameters: the number of vortex singularities N and the constant spacing d between them. The two parameters were then optimized with respect to the averaged CRLB. Such a PSF design improves the localization precision at high background, however with a compromise in the depth range compared to the original DH-PSF.

Based on the same optimization process as described in the DH-PSF work, Lew et al. reported a Corksrew PSF design which displays a single rotating lobe[59] (Fig. 1.8). The energy in this PSF is more concentrated than the DH-PSF for having only one lobe, however, imaging twice with a 180°-rotated phase mask is needed for a single depth estimation because the rotation angle can not be determined from a single image.

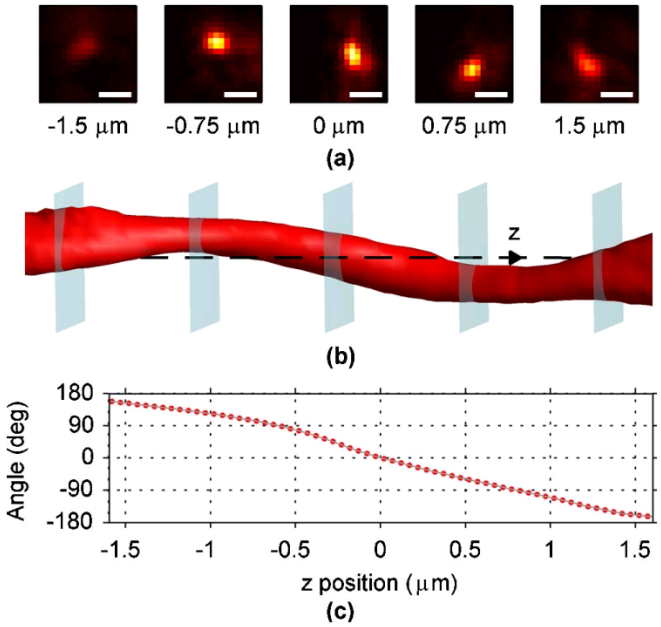

Fig. 1.8 (a) Corkscrew PSFs at various z positions. Scale bars are 1 μm. (b) 3D isosurface rendering of the corkscrew PSF, where the z positions of the blue planes correspond to the cross sections in (a). (c) Calibration curve measured at discrete z positions. Image adapted from Lew et al.[59] with permission. Copyright 2011 Optical Society of America.

The sequential image acquisition precludes the application of this method to tracking of fast-moving emitters and super-resolution experiments with blinking dyes as a fluorescent molecule could be switched off in the second frame. Although it is noted in ref[59] that two $4f$ sections can be used to avoid the sequential imaging as in the biplane imaging, however, this will lower the signal by splitting the photons in two lobes.

Higher-order helical PSFs such as triple helix and tetra helix have also been reported more recently[61], and these have been shown to have superior robustness with respect to optical aberrations. For low-photon-count experiments, these higher-order PSFs will yield lower SNR, due to the distribution of the energy among a higher number of lobes, but aberration-robust PSFs could potentially offer enhanced localization precision through refractive or turbid thick biological samples.

Translating PSFs

Similar to encoding the depth information into PSF rotation, translation properties in the PSF have also been exploited for localizing point sources in 3D space.

Yajima et al. developed a technique for 3D particle localization using a wedge prism located at the back-focal plane (BFP) of the objective, forming two split images at the image plane[63]. The linear phase introduced by the prism separates the two lobes apart in the y direction. The z-directed movement of the point source around the sample plane is then converted into an x-directed disparity in the two split images. A year later, Sun

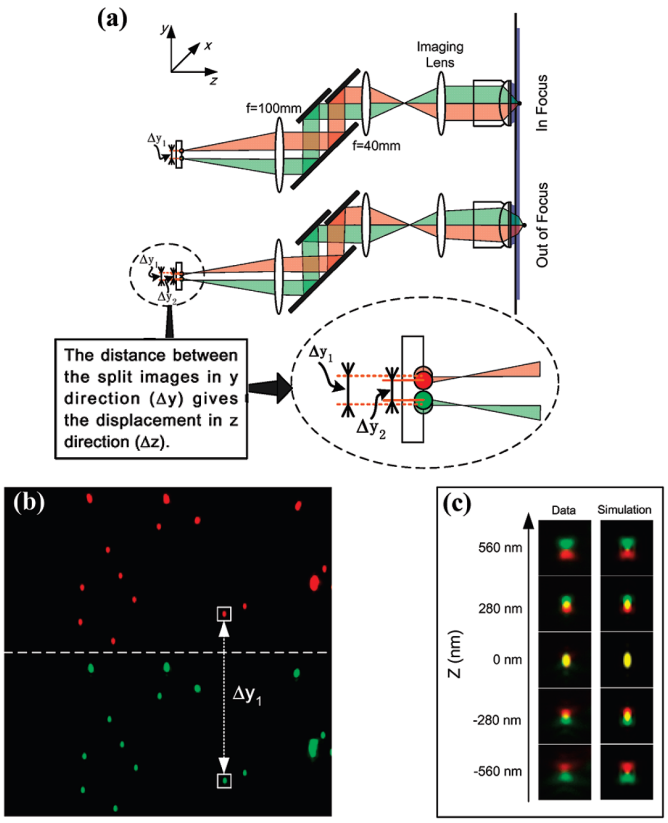

Fig. 1.9 A schematic illustration of the *parallax* technique. The red and green colors denote separate portions of the split light paths (a) and resulting pairs of images (b and c). Image adapted with permission from ref[62] Copyright (2009) American Chemical Society.

et al. reported a similar technique termed as '*parallax*' using a set of closely spaced mirrors instead of the prism to split the images[62] (Fig. 1.9). The mirrors are located at the re-imaged BFP of the objective without accessing the inside of the microscope. This offers more flexibility in terms of positioning the split views on the camera chip and transferring between different optical microscopy systems. The technique was then used to study glucose-transporter-containing vesicles in living adipocytes. It is worth noting that another similar technique, the *bisected pupil* employs an SLM to display two linear phase ramps, resulting in a two-lobe PSF similar to the above discussed techniques[64]. In this case, two orthogonal linear polarizations of light are recorded to enable correction of localization errors induced by the orientation of the dipole emitters. When imaging isotropic emitters, this technique also enables 3D localization from image disparities. These three techniques are all based on splitting the pupil of a conventional microscope (by using wedge prism, mirrors and SLM respectively), therefore, they suffer from limited depth ranges as the diffraction-limited PSF does.

In order to extend the operable depth range, Airy beams have been utilized for 3D localization microscopy[17, 65, 66]. The self-accelerating translation enables encoding of the emitter's axial position while the diffraction-free propagation gives rise to the depth

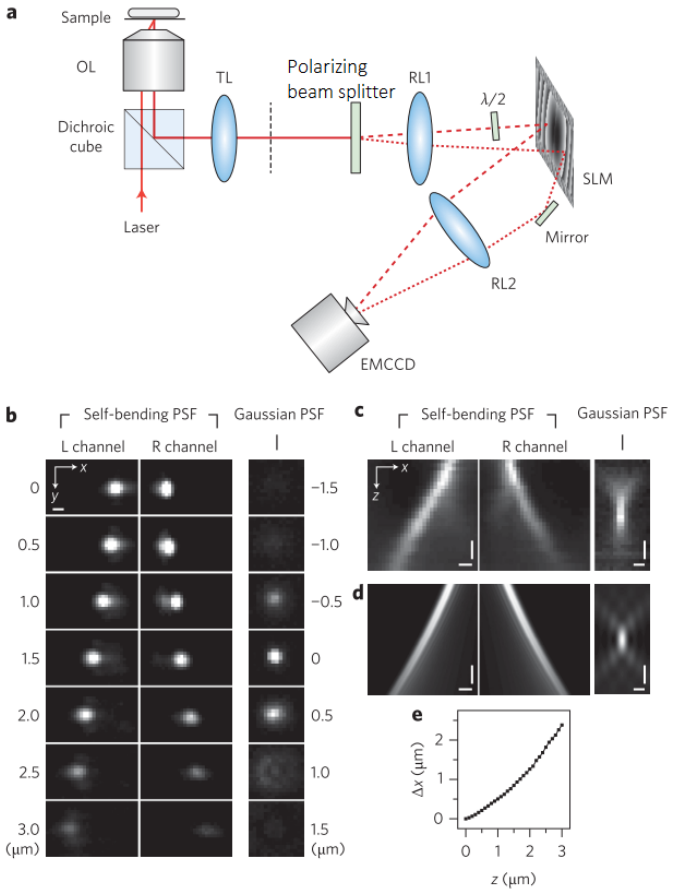

Fig. 1.10 Self-bending PSF (SB-PSF) and the schematic of its imaging setup. The collected photons are split into two imaging channels with a polarizing beam splitter and guided onto the two halves of an SLM respectively. A half-wave plate (marked as '$\lambda/2$') is used in one of the channels because the SLM modulates only single polarization. OL: objective lens; TL: tube lens; RL: relay lens. Image adapted from Jia et al.[17] with permission. Copyright 2014, Springer Nature.

range[67, 68]. However, the extended lateral profile of the Airy beam introduces difficulty in PSF fitting and reduces the peak SNR. Jia et al. modified the Airy beam to produce a self-bending PSF for 3D localization microscopy[17]. An SLM was located at the re-imaged pupil plane of a $4f$ relay system to display a truncated cubic phase mask for generation of the SB-PSF. The pupil truncation was for eliminating the side lobes of the PSF, so that simple Gaussian functions can be used to fit the PSF profile. To measure the PSF translations, a two-channel configuration was used with two phase masks being 180° rotation to each other yielding two diverging lobes as shown in Fig. 1.10. This technique offers more depth range than a conventional microscope, however, it suffers from the following disadvantages: (1) The pupil truncation is not photon efficient and accounts for about 30% of photon loss, which is not ideal for low-photon-count experiments. (2) Only half of the diffraction-free range of the PSF can be utilized due to the fact that the PSF is symmetrical on the two sides of the focal plane. (3) The latter shift in the PSF varies parabolically with the amount of defocus, which means its depth sensitivity is not uniform and in particular it can not be used near the focal plane.

We proposed recently a different technique using intact Airy-beam PSF (AB-PSF) combined with image recovery based on Wiener deconvolution for 3D particle localization[65], termed as 'Airy-CKM'. Instead of using two phase masks with 180° rotation, a single cubic phase mask is used in the imaging system before the light is split into two channels. The two channels has a fixed mutual offset in defocus, which enables the deduction of the axial coordinate. The Airy-CKM technique yields the following advantages over the SB-PSF. Firstly, it provides a constant z-sensitivity. Secondly, it has no sign ambiguity, meaning almost the whole diffraction-free range of the AB-PSF can be utilized. Wiener deconvolution was performed to turn the extended intensity profile of the AB-PSF into a compact Gaussian-like recovered PSF. This allows us to work with high emitter concentration. This technique was then applied to tracking blood flow in a living zebrafish[66]. The Airy-CKM technique, as one of the main results of this thesis, will be further discussed in the following chapters.

PR-MLE-based PSFs

Unlike the previously discussed PSFs, some PSFs with a z-dependent intensity profile do not have a single quantifiable feature (e.g. diameter, rotation angle, translation) that can be related to the z coordinate of the emitter. In this case, the phase-retrieval-based maximum-likelihood estimation (PR-MLE) reported by Quirin et al.[69] is often used to extract the 3D coordinates. An example of this kind is the CRLB-optimized PSFs.

Fisher information has been demonstrated in microscopy as a way to quantify the statistical limit of the achievable localization precision of a certain PSF, i.e. the CRLB[70, 71]. Shechtman et al. proposed an information-optimized PSF family: the tetrapod PSFs[72, 73]. The first 55 Zernike polynomials were used as a basis set to search for an optimized pupil function that can generate a PSF with the best localization precision, or in other words the minimal CRLBs. The optimization process can be done over arbitrary depth ranges. They first reported phase masks optimized for 3 μm depth (termed as the 'saddle-point phase mask') and 6 μm depth (termed as the 'cat mask') respectively, and then a family of CRLB-optimized PSFs termed as 'tetrapod PSFs' were reported as shown in Fig. 1.11.

To extract the 3D coordinates, a stack of calibration PSFs with known z spacing is firstly used to retrieve the pupil function of the imaging system which can be then used to generate the PSFs on a computer with a set of parameters (x, y, z coordinates, total number of photons N_{ph} and average number of photons per pixel N_{bg}). By minimizing the log-likelihood function between the experimentally recorded PSF and the computer-generated PSF, one can determine those five above mentioned parameters. However, the minimization process of the likelihood function is computationally intense, especially if the PSF shape is self-similar and induces many local minima in the optimization process.

In addition, overlapping PSFs will inevitably alter the likelihood function and therefore degrade the achievable localization precision. This precludes the application of this approach to imaging of high-density emitters.

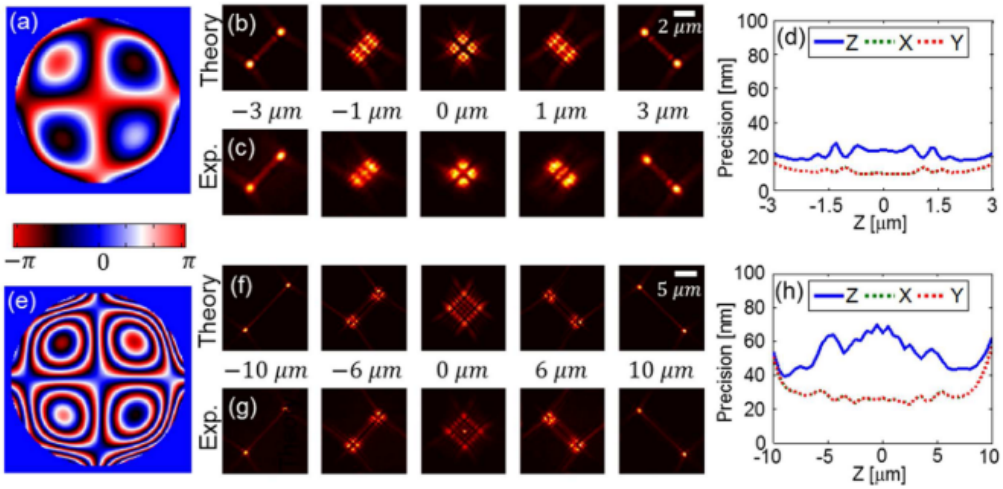

Fig. 1.11 Tetrapod phase masks (left), corresponding PSFs (middle) and simulated CRLBs (right), optimized for 6 µm (upper) and 20 µm (lower) respectively. Image adapted from Shechtman et al.[72] with permission. Copyright 2015 American Chemical Society, material under an ACS AuthorChoice License.

1.3 Theoretical background material

1.3.1 Point-spread function, convolution and deconvolution

The intensity point-spread function (PSF) describes the response of an imaging system to a sub-resolution point source. For a conventional imaging system, the image of a point source is an Airy disk due to the low-pass filtering of the imaging system and the wave nature of the light. The image of an object is thus a convolution of the object profile with the Airy disk which describes the PSF. In the case of a pupil engineered system as reviewed in the previous section, the image will be a convolution of the object with the corresponding engineered PSF. For an incoherent imaging system, the relationship between the image and the object in real space and Fourier space can be described as,

$$I = PSF \circledast O, \;\; \mathscr{F}\{I\} = \mathscr{F}\{PSF\} \times \mathscr{F}\{O\}, \tag{1.1}$$

where I is the detected image and O is the object. $\circledast$ and $\mathscr{F}$ denote convolution and Fourier transform respectively.

Provided that the PSF of an imaging system is known, the object can be recovered from a PSF-encoded image following deconvolution, i.e. a simple division in the Fourier space based on equation 1.1, as has been investigated in literature[74]:

$$H = \frac{1}{\mathscr{F}\{PSF\}},\ I_r = \mathscr{F}^{-1}\{\mathscr{F}\{I\} \times H\}, \tag{1.2}$$

where I_r is the recovery of the object. However, such an 'inverse filter' will cause infinitely high values if there are zeros in the Fourier transform of the PSF. In addition, the inverse filter is found to amplify the noise[74]; thus, it is non-preferred for image deconvolution as the imaging process will inevitably introduce noise.

The drawbacks of the inverse filter can be overcome by performing the image deconvolution with a Wiener filter:

$$H = \frac{(\mathscr{F}\{PSF\})^*}{|\mathscr{F}\{PSF\}|^2 + nsr},\ I_r = \mathscr{F}^{-1}\{\mathscr{F}\{I\} \times H\}, \tag{1.3}$$

where *nsr* is a regularization parameter which represents the noise-to-signal ratio. Large *nsr* causes the image to be smoothed, reducing contrast while also reducing noise. Conversely, a low value of *nsr* causes the image to be noisier but boosts contrast at higher spatial frequencies. It is often chosen empirically and is assumed to be constant[74, 75]. In the this work, unless elsewhere stated, deconvolution refers to the Wiener deconvolution using equation 1.3.

1.3.2 Other characterizations of the imaging system

The PSF which can be recorded by a detector is the magnitude-square of the complex-valued amplitude PSF (APSF). Note that PSF refers to the intensity point-spread function throughout this thesis. The PSF and the optical-transfer function (OTF) are each other's Fourier transforms, thus they carry the same amount of information. However, both are incomplete descriptions of the imaging system as they do not contain the phase information of the optical field. The OTF is the auto-correlation of the complex-valued amplitude OTF (AOTF), which is the Fourier transform of APSF (Fig. 1.12). AOTF is non-zero only on a spherical shell of radius $k = 2\pi n/\lambda$[77] in the spatial frequency space, where n is the refractive index of the medium and λ is the wavelength. Thus it can be written as a two-variable function with spatial frequency component k_z expressed as a function of k_x and k_y: $k_z(k_x,k_y) = \sqrt{(2\pi n/\lambda)^2 - k_x^2 - k_y^2}$. Therefore, the amplitude PSF can be written as follows:

$$\begin{aligned} APSF(x,y,z) &= \int\int\int AOTF(k_x,k_y,k_z)\ \mathrm{e}^{\mathrm{i}(k_x x + k_y y + k_z z)} \mathrm{d}k_x \mathrm{d}k_y \mathrm{d}k_z \\ &= \int\int P(k_x,k_y)\ \mathrm{e}^{\mathrm{i}(k_z(k_x,k_y)z)}\ \mathrm{e}^{\mathrm{i}(k_x x + k_y y)} \mathrm{d}k_x \mathrm{d}k_y, \end{aligned} \tag{1.4}$$

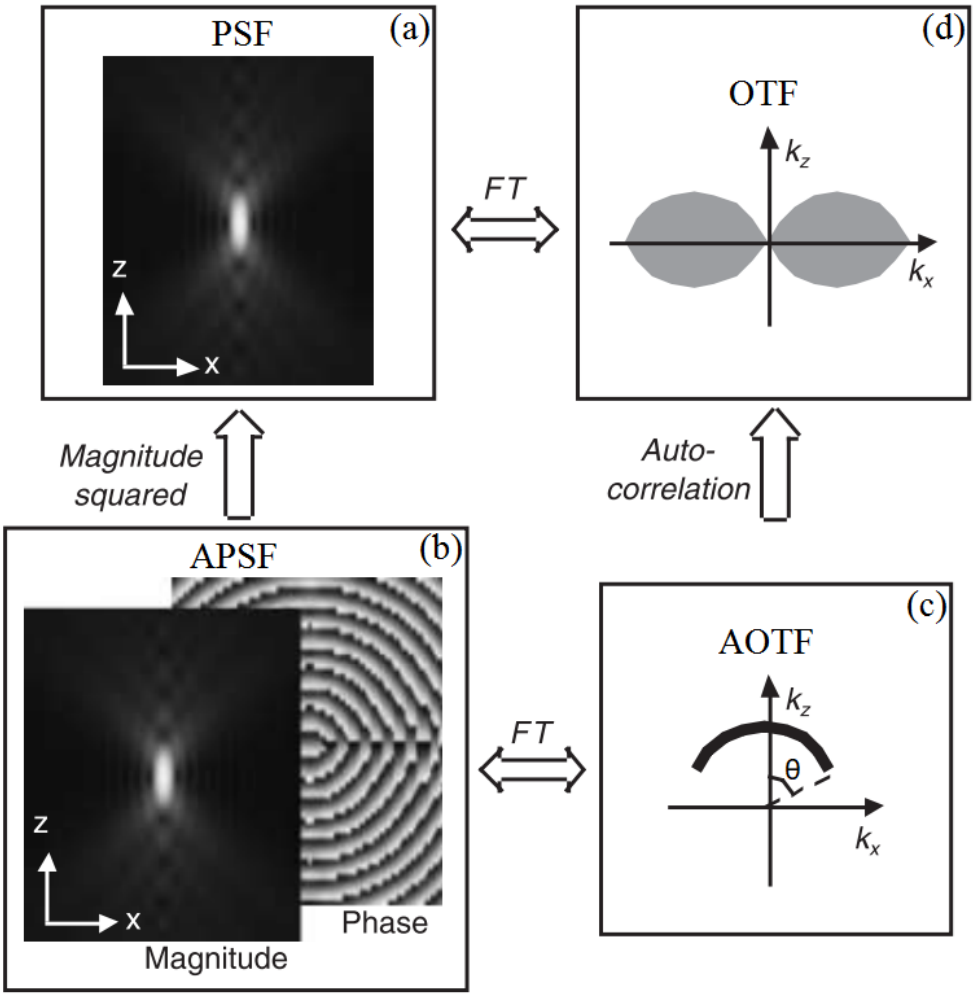

Fig. 1.12 Relations between (a) PSF, (b) amplitude PSF, (c) amplitude OTF, and (d) OTF. FT: Fourier transform. Image adapted from Hanser et al.[76] with permission, copyright 2003 Optical Society of America.

where $e^{i(k_z(k_x,k_y)z)}$ can be seen as a phase term resulting from the defocus of the imaging system by a distance z and the two-variable function $P(k_x,k_y)$ denotes the pupil function which is also the projection of AOTF on the k_x-k_y plane. Equation 1.4 shows that the pupil function multiplied by the defocus phase is the Fourier transform of the amplitude PSF. This is the basis of the emerging field of engineered PSFs or pupil-engineering microscopy. The pupil function, the APSF and the AOTF contain both the intensity and phase information of the optical field; thus, they are considered complete descriptions of the imaging system within the scalar theory of light. For the paraxial scenario, the k_z can be simplified. Let $k_\rho^2 = k_x^2 + k_y^2$, we have

$$k_z(k_x,k_y) = \sqrt{k^2 - k_\rho^2} = k\sqrt{1-(\frac{k_\rho}{k})^2} \approx k(1-\frac{1}{2}\frac{k_\rho^2}{k^2}),\ \ k_\rho \ll k, \tag{1.5}$$

where one can observe that the first term is constant resulting in a plane wave, while the second term is proportional to k_ρ^2 producing a parabolic wavefront.

1.3.3 Pupil engineering

As discussed above, the complex field at the image plane (i.e. the APSF) can be altered by modifying the pupil function $P(k_x, k_y)$. As a result, the intensity PSF that is recorded by a camera is also altered. This provides a way to design the PSF of an imaging system to yield some desired properties such as the extended DOF in wavefront coding (WFC) imaging[78, 79] and the rotating PSF for encoding of particles' 3D coordinates[16]. For most modern microscopes, the pupil plane is conjugate to the BFP of the objective. Thus, to modulate the pupil function, one needs to locate and access the BFP. However, the BFP is situated inside the objective in most cases, especially for high NA, high magnification objectives. Therefore, a $4f$ relay system is most commonly used to reimage the BFP where additional optical elements can be easily added to modulate the pupil function as shown in Fig.1.13.

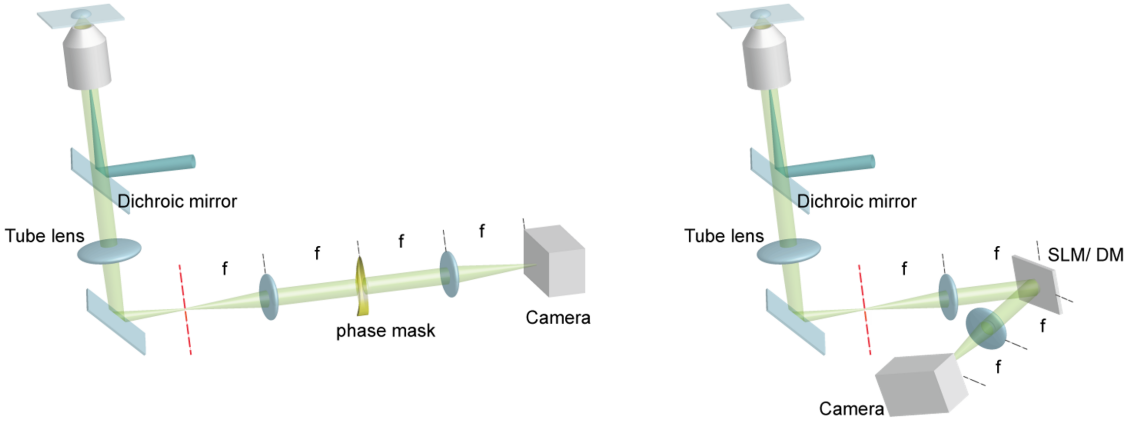

Fig. 1.13 Pupil engineering using $4f$ relay system. Either a physically fabricated mask (a) or a digitally displayed mask on an SLM or a deformable mirror (b) can be used. Red dashed lines indicate the intermediate image planes.

SLMs provide flexibility in PSF design and change of modulation strength, making them the most popular device in this field. However, SLMs are expensive and can modulate only one polarization of the light, which effectively wastes half of the collected photons. Additionally, the diffractive nature of the SLM also results in multi-order-diffraction losses. Special optical configurations have been reported to make use of both polarization directions[64], however, loss through diffraction is inevitable. An alternative way to modulate the pupil function is by using a fabricated mask, which provides higher optical efficiency (up to 100% using modern laser polishing and anti-reflection coating). However, there is no flexibility in the design of the PSF once the mask is fabricated.

Both amplitude[49] and phase[16] modulations can be utilized, however, an amplitude mask will inevitably lower the overall optical throughput, which is non-preferred in low-photon-level experiments such as super resolution and single-molecule tracking. Phase-only masks are by-far the most commonly used for PSF-engineering purposes.

1.4 Simulation setup

The following chapters of this thesis involve extensive simulations on the PSF variations resulting from various pupil functions. Thus it is worth specifying the imaging model, assumptions and simulation settings before the discussions. The PSF formation of a pupil-engineered microscope is simulated with the parameters approximating that of the state-of-the-art commercially available equipment. Two planes, namely the pupil plane and the image plane, are considered which are related by Fourier transformation highlighted in equation 1.4.

The image plane is sampled according to the pixel size and the size of the detector, a $N_{pxl} \times N_{pxl}$ detector is assumed with square pixel size of $\mathrm{d}x \times \mathrm{d}x$ (the fill factor of the detector is assumed to be one). Images or PSFs are thus a $N_{pxl} \times N_{pxl}$ real-valued matrix and the amplitude PSF is a complex-valued matrix of same size. If otherwise stated, $N_{pxl} = 512$ and $\mathrm{d}x = 16\,\mu\mathrm{m}$ to approximate the Andor iXon 897 EMCCD camera. The pupil plane has the same number of data points (i.e. $N_{pxl} \times N_{pxl}$) as the image plane with the maximum frequency being $1/\mathrm{d}x$ and the spacing between discrete frequency coordinates being $\mathrm{d}f = 1/(\mathrm{d}x \times N_{pxl})$ (in inverse microns). For a microscope with magnification of M and numerical aperture of NA, the highest spatial frequency that can pass the imaging system, i.e. the radius of the pupil aperture in the Fourier space is therefore:

$$R_{pupil} = \frac{NA}{\lambda}, \tag{1.6}$$

with λ being the wavelength of the collected light.

A schematic of this process is shown in Fig. 1.14. The pupil function $P(k_x, k_y)$ is a clear aperture if no additional phase modulation is added to it. Such a pupil function will result in an Airy disk on the image plane. In the presence of defocus, a defocus phase term that is described by $k_z(k_x, k_y)z$ is added to the clear aperture. And in the case of the pupil-engineered PSFs, a corresponding phase term is added to the pupil function to generate the desired PSF. The pipeline for the PSF formation used in the simulation can be simplified as follows:

- Given a specific amplitude or phase function $A\mathrm{e}^{\mathrm{i}\phi}$, combine it with the pupil aperture to get the new pupil function $P = P_0\, A\mathrm{e}^{\mathrm{i}\phi}$.
- A defocus phase profile described in equation 1.4 is then combined with the pupil function to account for wavefront curvature caused by axial displacement of the point source. $P = P\ \mathrm{e}^{\mathrm{i}k_z z}$ or $P = P\ \mathrm{e}^{\mathrm{i}k_\rho^2 \psi}$, where ψ is the defocus parameter.
- Fourier transform the pupil function using 2D fast Fourier transform with the built-in *fft2* function in Matlab to get the complex field at the image plane, i.e. the amplitude PSF. $APSF = FFT(P)$.

- The amplitude PSF is squared to get the intensity PSF that can be measured by a camera.
- The intensity PSF is then normalized (sum to 1) and multiplied by the total number of photons N_{ph}, following which a certain number of background photons N_b is added to each pixel.
- Shot noise is added by taking random numbers from the Poisson distribution with mean parameter being the number of photons on each pixel.
- The obtained PSF is then used for other calculations such as the CRLB or for analysis.

The simulations in this thesis assume the imaging process to be shot-noise limited unless otherwise stated in the text.

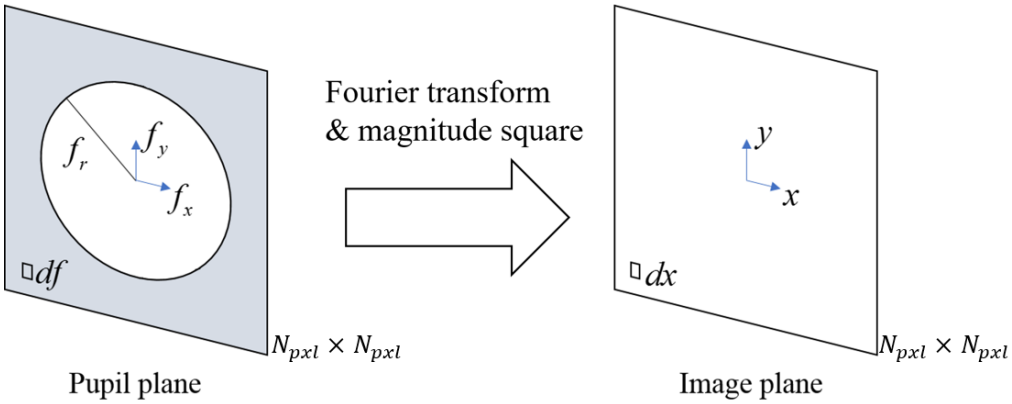

Fig. 1.14 Schematic of the sampling of the pupil plane and the image plane assuming a circular pupil. dx: pixel size of the detector; N_{pxl}: number of pixels; df: 'pixel size' in the spatial frequency domain. Figure inspired by ref[74].

1.5 Summary and original contributions

In this chapter, we emphasize the importance of precise point localization in various fields, followed by the motivation and an outline of this research. A detailed literature review is provided on state-of-the-art 3D imaging techniques and 3D point localization techniques in microscopy, in particular the focus is on several 'single-shot' techniques that are based on pupil engineering including the widely used DH-PSF, and the tetrapod PSF. The theoretical background of pupil-engineering is also discussed, followed by an introduction of the simulation settings and PSF generation pipeline.

The original contributions reported in this thesis are the following:

- Development of a new technique for 3D point-localization microscopy over extended depth range using AB-PSF (the 'Airy-CKM' technique).

- Development of a new 'twin-Airy' technique for 3D extended-depth point-localization microscopy. As stated in the Attributions, Dr Paul Zammit first proposed the project. All the analysis and experiments were conducted by the author.
- The first use of pupil-engineered PSFs for *in vivo* blood-flow measurement. The sample preparation was done by Dr Vytautas Zickus. The imaging and analysis were conducted by the author.
- Comparison of the state-of-the-art pupil-engineered PSFs by means of CRLB.
- Proposing the use of pupil-engineered PSFs for traction-force microscopy to increase imaging speed and resolution.
- Proposing the use of a single intact AB-PSF for 3D particle localization.

Chapter 2

Point localization using Airy-beam PSF

Airy beams yield the combined properties of diffraction-free propagation and accelerating self-translation[67, 80, 68], which is pertinent for 3D particle localization over extended depth range[65, 66]. In this chapter we investigate the Airy-beam PSF (AB-PSF) generated by a cubic phase mask and its depth-dependent image translations by theoretical analysis and numerical simulations, based on which a new method for 3D point-localization microscopy is developed, i.e. the Airy-CKM technique. Compared to conventional approaches, this technique provides significantly improved depth range, simple implementation and nearly 100% optical throughput. Besides, a deconvolution-based data processing algorithm is proposed which enables the recovery of compact PSF profiles and thus imaging of high emitter densities. Measurement of fluid flow dynamics is performed as a proof of concept, which will be discussed at the end of this chapter.

2.1 Cubic phase mask and the Airy-beam PSF

In 1995, Dowski and Cathey introduced a cubic phase mask to extend the depth of field (DOF) of optical imaging systems[78], which is known as wavefront coding (WFC). The cubic phase mask for WFC is placed at the pupil plane of the imaging system and can be expressed as $\alpha(x^3+y^3)$. x and y are coordinates normalized to the radius of the phase mask, and α is a constant that defines the peak modulation or the peak optical path difference introduced by the phase mask. Such an additional phase modulation produces an 'L'-shaped PSF as shown in Fig. 2.1a. Compared to the conventional diffraction-limited PSF (DL-PSF), which rapidly expands in size and decreases in intensity with the increasing defocus, the PSF generated with a cubic phase mask yields an insensitivity to defocus changes. Such depth-insensitivity enables the 'L'-shaped PSF image to be deconvolved with a single pre-recorded PSF as deconvolution kernel, yielding a compact recovered profile regardless of the defocus of the imaging system (right column of Fig. 2.1a).

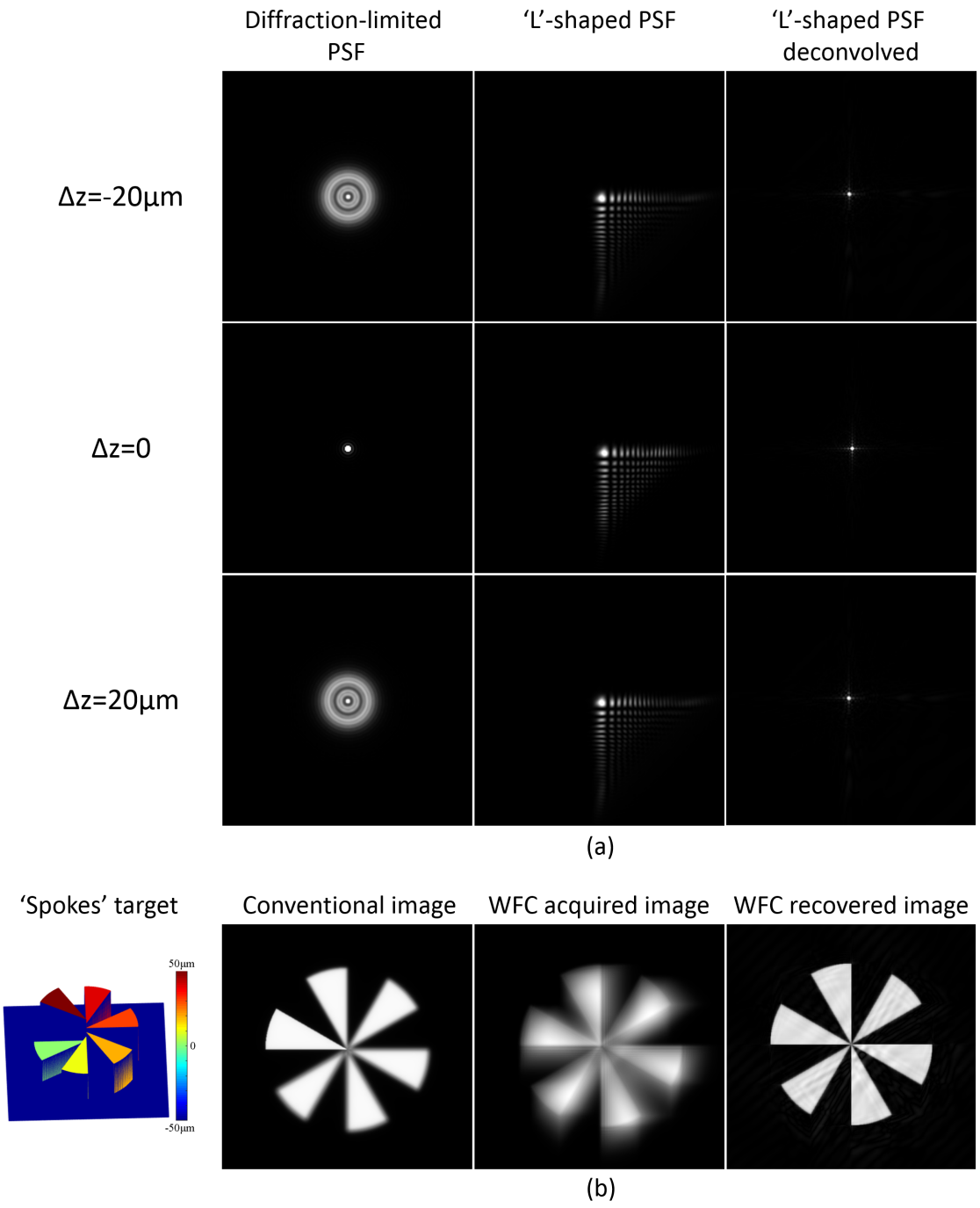

Fig. 2.1 (a) Simulation comparison of the diffraction-limited PSF, the 'L'-shaped PSF generated with a cubic phase mask ($\alpha = 5\lambda$) and its corresponding deconvolved PSF. Wiener filter is used for deconvolution with the in-focus 'L'-shaped PSF as deconvolution kernel. Monochromatic light at 650 nm is assumed, with 20×, 0.4NA objective and 6.5 μm pixel size. (b) Imaging of a 'spokes' target with varying depths using conventional system and WFC system.

The spatial expansion of the out-of-focus DL-PSF blurs the image, thus conventional imaging systems have very limited DOF. On the contrary, although the image recorded using a WFC system is blurred as the object is convolved with the 'L'-shaped PSF, the acquired image also carries the depth-insensitivity of the PSF. Similarly, this depth-insensitivity enables the acquired image to be digitally recovered with a single pre-recorded deconvolution kernel to produce a sharp image with a significantly extended DOF compared to conventional systems[78]. As shown in simulations (Fig. 2.1b), a 3D 'spokes' target with each spoke at different depth is imaged using both the conventional and WFC systems. Both imaging systems are focused at $z = 0$. Because the conventional system has a small depth range, only the image of the in-focus spoke has good contrast while the others are blurred to various degrees depending on the amount of defocus. As expected, the 'intermediate image' (acquired image) from the WFC system which is encoded by the 'L'-shaped PSF appears to be blurred; but the recovered image following image deconvolution (using the in-focus PSF as deconvolution kernel) is sharp and with high contrast. High spatial frequency components are preserved which can be seen from the central part of the spokes pattern.

However, the 'L'-shaped PSF is not completely insensitive to defocus. Despite the little variation in its intensity profile with respect to the in-focus profile, such a PSF yields a depth-dependent translation along the image diagonal. This leads to the artefacts in the WFC systems, as can be observed from the 'ripple-like' pattern in the recovered image of spokes in Fig. 2.1b. In this example, the acquired image is deconvolved with a single pre-recorded PSF as deconvolution kernel, however, the object contains a lot of depth variations. Zammit et al. reported the complementary-kernel matching (CKM) technique to eliminate the artefacts in WFC systems[81]. Instead of using a single pre-recorded PSF for image recovery, a stack of pre-recorded PSFs are utilized to search for the exact defocus for each pixel. The CKM-recovered image are in principle free of artefacts since each pixel is recovered with a PSF that is matched to the amount of defocus at that pixel (evaluation is in fact performed in a small neighborhood of each pixel). In this chapter, instead of trying to eliminate the PSF-translation-induced artefacts in the image, it will be shown that the PSF translations can be utilized to localize point emitters in 3D space.

The fact that the cubic phase is optimal for generating a defocus-invariant PSF to extend the DOF agrees with the findings of the Airy-beam community. Nondiffracting accelerated Airy beam is a solution to the paraxial wave equation in Cartesian coordinates[67], and the Fourier transform of the finite-energy Airy beam is a Gaussian beam modulated by a cubic phase[80, 68]. The PSF resulting from a cubic phase mask and a clear aperture (i.e. constant amplitude) yields very similar properties to the finite-energy Airy beams, in terms of not only the intensity profile but also the parabolic lateral translation and extended propagation range. Thus in this work, the 'L'-shaped PSF generated with a cubic phase mask will be referred to as the Airy-beam PSF (AB-PSF).

2.2 Optical-transfer function of the AB-PSF

The pupil function for a WFC system is the combination of the cubic phase and a phase accounting for the defocus of the imaging system. For simplicity, we consider here only one dimension. Under the paraxial approximation, the pupil function can be written as:

$$P(x) = \begin{cases} e^{ix^2\psi} e^{i\alpha x^3} & |x| \leq 1 \\ 0 & |x| > 1, \end{cases} \tag{2.1}$$

where x is the spatial coordinate normalized to the pupil size, ψ is the defocus parameter in rad and α is the peak modulation introduced by the cubic phase mask in rad.

The OTF of an imaging system is the auto-correlation of the pupil function[82]:

$$\begin{aligned} OTF(u,\psi) &= \int P(x+u/2)P^*(x-u/2)\mathrm{d}x \\ &= \int_{-1+|u|/2}^{1-|u|/2} e^{i(x+u/2)^2\psi} e^{i\alpha(x+u/2)^3} e^{-i(x-u/2)^2\psi} e^{-i\alpha(x-u/2)^3} \mathrm{d}x \\ &= e^{i\frac{\alpha u 3}{4}} \int_{-1+|u|/2}^{1-|u|/2} e^{i3\alpha u x^2} e^{i2u\psi x} \mathrm{d}x, \end{aligned} \tag{2.2}$$

where u refers to the spatial frequency. The phase term $\exp(i3\alpha u x^2)\exp(i2u\psi x)$ oscillates fast when α is large, an example is shown in Fig. 2.2. Therefore, the above integral can be estimated using the stationary-phase approximation[78]. Let

$$\phi(x) = 3\alpha u x^2 + 2u\psi x. \tag{2.3}$$

The stationary point of this phase therefore satisfies:

$$\frac{\partial\phi(x)}{\partial x} = 6\alpha u x + 2u\psi = 0, \;\; x_s = -\frac{\psi}{3\alpha}, \tag{2.4}$$

with x_s being the stationary point. Thus the OTF can be approximated as:

$$\begin{aligned} OTF(u,\psi) &\approx e^{i\frac{\alpha u 3}{4}} e^{i\phi(x_s)} \sqrt{\frac{2\pi i}{|\phi''(x_s)|}} \\ &= e^{i\frac{\alpha u 3}{4}} e^{-i\frac{\psi^2 u}{3\alpha}} e^{i\frac{\pi}{4}} \sqrt{\frac{\pi}{3\alpha|u|}}, \;\; u \neq 0. \end{aligned} \tag{2.5}$$

The phase of the OTF contains a cubic term and a linear term of the spatial frequency u. The cubic term is independent of the defocus parameter ψ while the linear term is

quadratic to the defocus of the imaging system. It will be shown later this term contributes to a lateral translation in the image. The absolute value of the amplitude of the optical-transfer function (which is also known as the modulation-transfer function (MTF) and describes the spatial frequency response of an imaging system) is also independent of the defocus parameter ψ. This is the property that WFC systems utilize to provide extended depth of field. For conventional systems, the OTF can be obtained from equation 2.2 by setting α to zero:

$$\begin{aligned} OTF(u,\psi) &= \int_{-1+|u|/2}^{1-|u|/2} e^{i2u\psi x} dx \\ &= \begin{cases} \frac{\sin(\psi u(2-|u|))}{\psi u} & \psi > 0 \\ (2-|u|) & \psi = 0. \end{cases} \end{aligned} \tag{2.6}$$

From equation 2.6 one can see that the amplitude of the OTF of a conventional imaging system degrades in presence of defocus, it exhibits nulls when:

$$\begin{aligned} &\frac{\sin(\psi u(2-|u|))}{\psi u} = 0 \\ &u = \pm 1 \pm \sqrt{1 - \frac{n\pi}{\psi}}, \end{aligned} \tag{2.7}$$

where n is any integer satisfying $0 < n \leq \frac{\psi}{\pi}$. The larger the defocus, the more nulls in the MTF of the conventional system (Fig. 2.3a), and thus a greater band of spatial frequency will be lost in the image. This is observed in the simulations in Fig. 2.1b (result with conventional system), the central area with the high spatial frequencies is blurred. In contrast, the spatial frequency of a wavefront coding system is well preserved (Fig. 2.3b), thus the same area of the spoke image is of high contrast as shown in Fig. 2.1b (WFC recovered image).

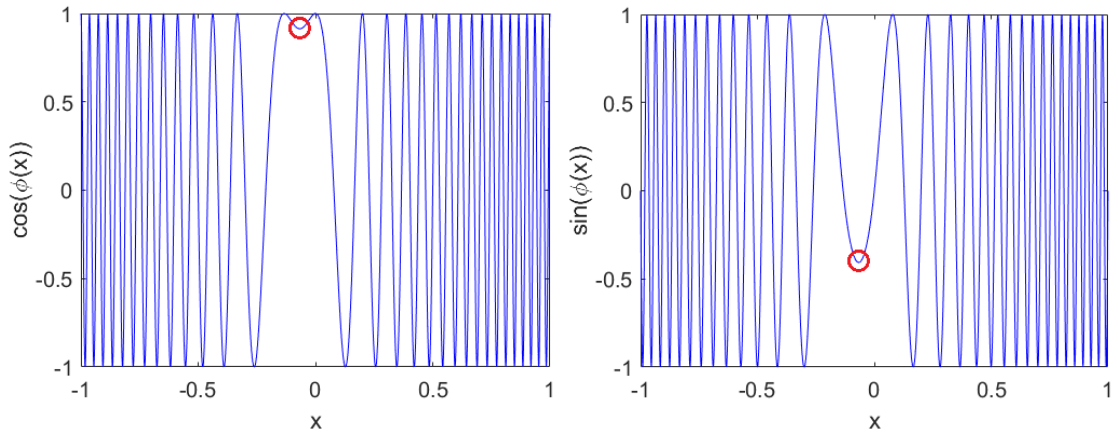

Fig. 2.2 The real part and the imaginary part of the phase $\phi(x)$, for a peak modulation of 5λ (i.e. $\alpha = 5 \times 2\pi$ rad), $u = 1$ and a defocus of 2λ ($\psi = 2 \times 2\pi$ rad). The stationary point is indicated in red circles.

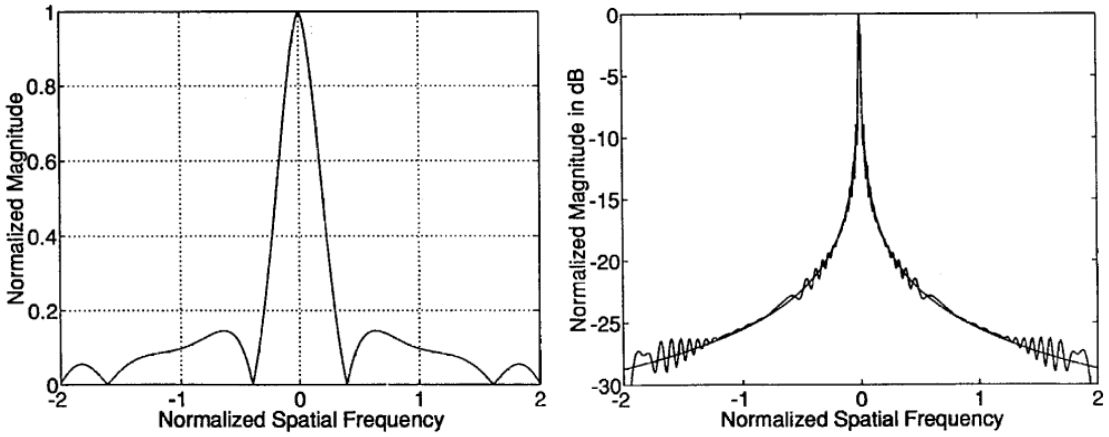

(a) (b)

Fig. 2.3 (a) The MTF of a defocused conventional imaging system. (b) The MTF of the WFC system. Images adapted from Dowski and Cathey[78] with permission.

2.3 Lateral translation properties of the AB-PSF

2.3.1 The quadratic depth-dependent translation

From equation 2.5, the OTF of an imaging system with a cubic phase mask placed at the pupil plane contains a linear term: $\exp(-\mathrm{i}\frac{\psi^2 u}{3\alpha})$. From the fact that the OTF is the Fourier transform of the PSF and the Fourier-shift theorem

$$\mathscr{F}\{f(x-x_0)\}(u) = \mathrm{e}^{-\mathrm{i}2\pi u x_0} F(u), \tag{2.8}$$

we can conclude that the linear-phase term in the OTF corresponds to a defocus-dependent lateral translation in the PSF given by

$$\left(\frac{\psi^2 u}{3\alpha}/2\pi u\right) = \psi^2/6\pi\alpha. \tag{2.9}$$

Therefore, the AB-PSF encodes depth information of the object as a translation of its image, which is similar to those techniques employing defocus-related variations in the PSFs highlighted in the chapter 1. The amount of translation is proportional to the square of the defocus parameter, thus the AB-PSF yields a lateral translation that is quadratic to the amount of defocus.

As discussed in chapter 1, the object can be deconvolved from an image if the exact PSF or OTF is known, based on the following relations:

$$I = PSF \circledast O, \;\; \mathscr{F}\{I\} = H \times \mathscr{F}\{O\}, \tag{2.10}$$

where I refers to the image and O refers to the object. However, in most cases the PSF or OTF is unknown due to the unknown defocus. The AB-PSF maintains its profile over

large depth range and thus can be deconvolved with a single pre-recorded PSF even if their defocus parameters are mismatched.

Assume that H_r is the Fourier transform of the pre-recorded PSF used for deconvolution, the recovered object profile O_r following deconvolution satisfies

$$\mathscr{F}\{I\} = H_r \times \mathscr{F}\{O_r\}. \tag{2.11}$$

Combining equation 2.11 with equation 2.10 and 2.5, we have

$$\begin{aligned} \mathscr{F}\{O_r\} &= \frac{H}{H_r} \times \mathscr{F}\{O\} \\ &= \mathrm{e}^{-\mathrm{i}\frac{u(\psi^2-\psi_r^2)}{3\alpha}} \times \mathscr{F}\{O\}, \end{aligned} \tag{2.12}$$

where ψ_r is the defocus parameter of the pre-recorded PSF used in deconvolution. The linear phase term $\exp(-\mathrm{i}u(\psi^2-\psi_r^2)/3\alpha)$ in the Fourier space results in a depth-dependent lateral translation in the recovered image similar to that in the recorded image,

$$T(\psi,\psi_r) = \frac{\psi^2-\psi_r^2}{6\pi\alpha}, \tag{2.13}$$

where $T(\psi,\psi_r)$ is the amount of translation in the recovered image compared to an in-focus image recorded using conventional systems.

2.3.2 Simulated PSF translations and the influence of different phase mask strengths

The lateral translations associated with the AB-PSF and its corresponding deconvolved PSF are observed in simulations. A 20×, 0.4NA system is assumed with the defocus varying from 0 to 10 and 20 waves. The left column in Fig. 2.4 shows superimposed PSFs for two-dimensional cubic phase masks with various peak modulations of 5λ, 6λ, and 7λ; and their corresponding images deconvolved using an in-focus AB-PSF are shown on the right. The lateral translation of the PSFs is depth-dependent, which can be used to encode the defocus and axial displacement of point sources. One can also observe that the PSF translation is along the negative-unity gradient due to the same amount of translations in the x and y directions. The amount of translation in the deconvolved PSFs is the same as that in the AB-PSF if the in-focus AB-PSF is used as deconvolution kernel. This is equivalently setting the ψ_r to 0 in equation 2.13. In addition to the fact that the deconvolved AB-PSF displays a compact profile that resembles the in-focus DL-PSF, it can be observed that the deconvolved AB-PSF also yields a certain amount of ellipticity when the defocus of the deconvolution kernel is not matched with the defocus in the AB-PSF. The ellipticity grows as the mismatch increases. This property can be used as a

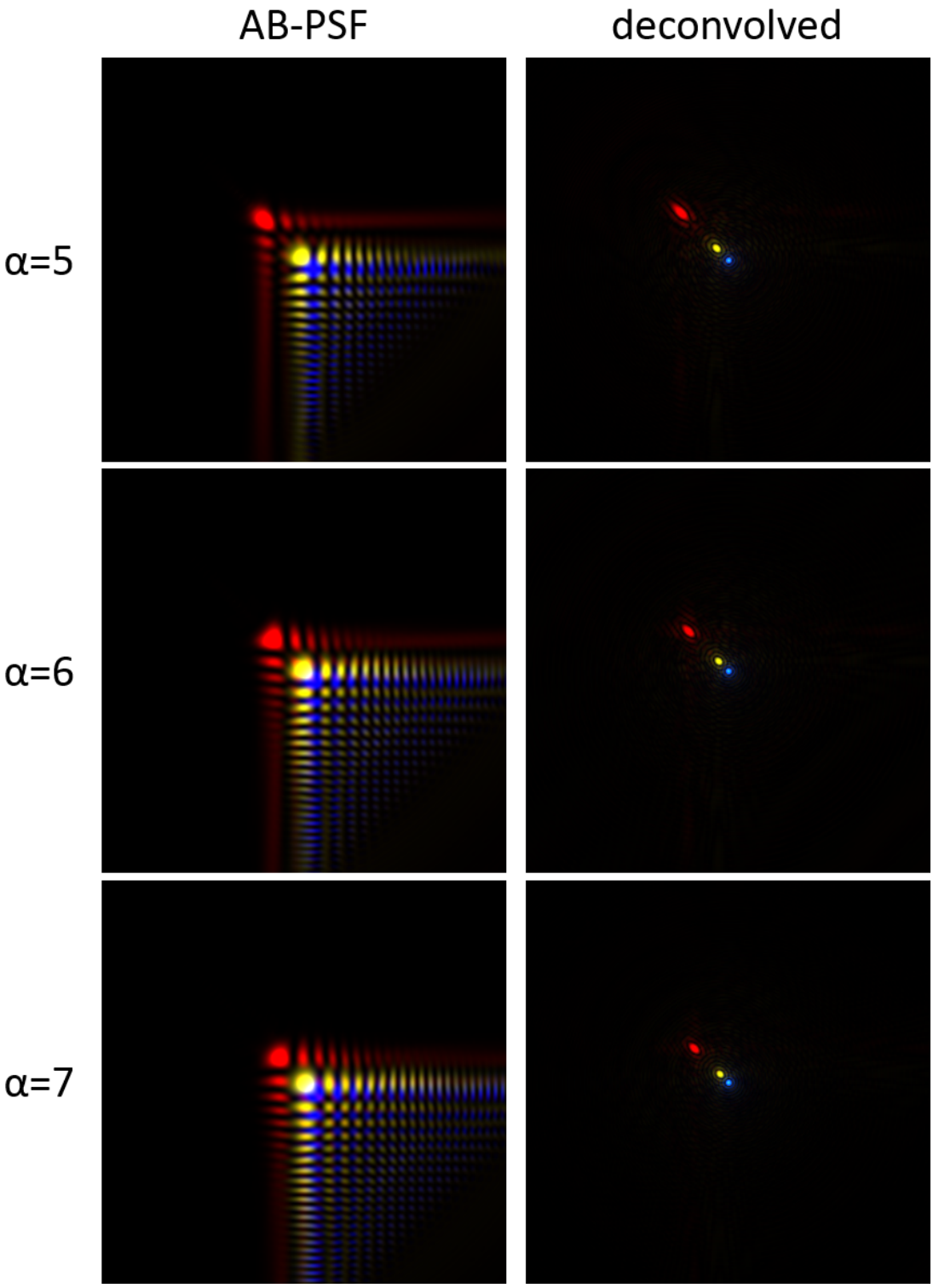

Fig. 2.4 Simulation of the lateral translations in the AB-PSFs with various peak modulation α (in waves), and corresponding translations in the recovered PSFs deconvolved with an in-focus AB-PSF ($\psi_r = 0$). Colors indicate various defocus values with blue, yellow and red representing defocus of $\psi = 0$, 10λ and 20λ respectively.

criterion in matching the two lobes in the 'twin-Airy' PSF as will be described in chapter 3.

Equation 2.9 and 2.13 reveal that a larger peak modulation (α) in the cubic phase mask gives less lateral translation in the AB-PSF and its deconvolved image. This is in agreement with simulation where the amount of translation decreases with the peak modulation increasing from $\alpha = 5\lambda$ to $\alpha = 7\lambda$ as shown in Fig. 2.4. In addition to the different lateral translation, a stronger cubic phase mask gives an AB-PSF with a larger depth range over which its intensity profile is invariant and thus can be deconvolved using a single pre-recorded PSF. It also results in an AB-PSF that is bigger in size with more lobes and thus a lower peak signal level in the acquired image.

2.4 Airy-CKM technique

2.4.1 Deducing the z with bi-plane arrangement

Although the AB-PSF and its deconvolved image yield a depth-dependant translation, it is practically difficult to measure this translation (and thus the depth of the emitter) without a reference. To this end, bi-plane imaging has been utilized in this work for measuring the image translation associated with the AB-PSF and its deconvolved image. This can be achieved by acquiring two images of the same object simultaneously through two imaging channels with dissimilar defocus parameters (and thus dissimilar image translations) followed by determination of the resultant disparity. As shown in Fig. 2.6, a dual-focal-plane arrangement implements two distinct offsets from a nominal plane with defocus ψ to yield images with defocuses: $\psi + \Delta\psi$ and $\psi - \Delta\psi$ on the same sensor. If we assume the image captured at $\psi + \Delta\psi$ is deconvolved with a PSF measured at a defocus of $\psi_r + \Delta\psi$ and correspondingly, the image captured at $\psi - \Delta\psi$ is deconvolved using a PSF recorded at a defocus of $\psi_r - \Delta\psi$, then the two-channel disparity (TCD) between two recovered images is

$$TCD(\psi, \psi_r) = T(\psi + \Delta\psi, \psi_r + \Delta\psi) - T(\psi - \Delta\psi, \psi_r - \Delta\psi) = \frac{2\Delta\psi(\psi - \psi_r)}{3\pi\alpha}, \quad (2.14)$$

which is proportional to $\psi_r - \psi$. Zero disparity happens if, and only if, $\psi_r = \psi$. Consequently, determining the deconvolution kernel which gives zero disparity yields the defocus, or equivalently, the depth of the emitter. Alternatively, if a single PSF (with ψ_r) is used for deconvolution, the TCD is a linear function to the actual defocus of the emitter. Thus given the calibration of the TCD-ψ relation, the defocus of the emitter can be deduced from the TCD. Since this approach was developed from the CKM technique for imaging of extended scenes[81], it is referred to as Airy-CKM in this thesis.

The coefficient of the two-channel disparity,

$$R = \frac{2\Delta\psi}{3\pi\alpha}, \tag{2.15}$$

determines the responsivity and hence sensitivity for determining defocus. The responsivity does not depend on the depth of the emitter (z coordinate), meaning that a relatively uniform localization precision can be obtained throughout the depth range. Moreover, it can be adjusted by changing the defocus difference $\Delta\psi$ or the cubic phase peak modulation α. As discussed, the range for invariance of the PSF can be increased by increasing α but this requires a compensating increase in $\Delta\psi$ to maintain responsivity of the disparity function.

Relation between the amount of defocus and axial displacement

The above discussions in this chapter relate the lateral translation in the AB-PSF and the image disparity in the Airy-CKM technique to the defocus parameter ψ. Although ψ is not a direct measure of the axial position z, it can be related to the z coordinate. An axial displacement Δz results in a defocused wavefront. The relation between z and ψ can be written as

$$e^{ik_z z} = e^{i(\bar{k_x}^2 + \bar{k_y}^2)\psi} = e^{i\frac{k_\rho^2}{(k\sin\theta)^2}\psi}, \tag{2.16}$$

where $\bar{k_x}$ and $\bar{k_y}$ are normalized pupil coordinates, and θ is the angle formed by the marginal ray and the optical axis. Under the paraxial approximation, substituting k_z with equation 1.5 and omitting the constant phase term that contributes to a plane wave, we have

$$\begin{aligned} -\frac{1}{2}\frac{k_\rho^2}{k}z &= \frac{k_\rho^2}{(k\sin\theta)^2}\psi \\ \psi &= -\frac{1}{2}k\sin^2\theta z \\ &= -\frac{\pi n\sin^2\theta}{\lambda}z. \end{aligned} \tag{2.17}$$

It is clear that under the paraxial approximation the amount of defocus in the wavefront is proportional to the axial displacement (i.e. the z coordinate). Thus we conclude that the AB-PSF and its deconvolved image have a depth-dependent lateral translation that is proportional to the square of the z coordinate of the point emitter; whereas the two-channel disparity in the Airy-CKM technique has a linear relation to the z coordinate of the emitter.

Note that the above discussions throughout this chapter are based on the paraxial assumption, and the stationary-phase approximation discussed in section 2.2 is valid

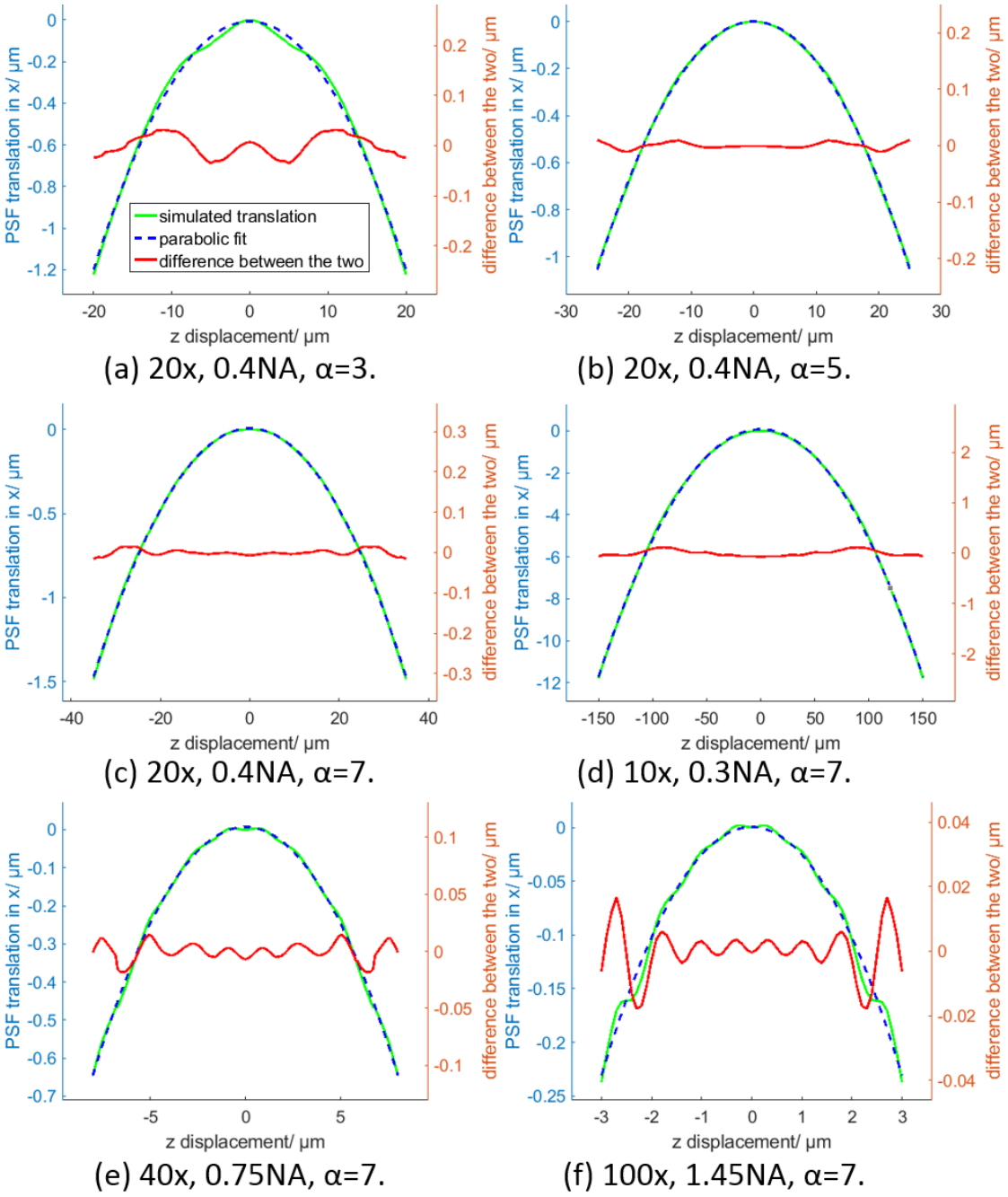

Fig. 2.5 Assessment of the parabolic translation in the AB-PSF in non-paraxial scenarios and with small α. The green curves are the lateral translations along the x direction in the main lobe of the simulated AB-PSF, while the blue dashed curves are the corresponding parabolic fit results. The red curves indicate the difference between the two. The 100×, 1.45NA system considered here employs an oil immersion objective with refractive index of 1.515, and all the other systems are assumed to use air objectives.

only for large α. Nevertheless, simulations show that even for small α and high NA objectives (which are not paraxial), the PSF generated by a cubic phase mask still approximately exhibits the parabolic lateral translation. Fig. 2.5 illustrates some simulated PSF translation curves compared with their corresponding parabolic fits. Firstly, the effect of different peak modulations in the cubic phase mask is investigated with the same imaging system, i.e. a 20×, 0.4NA microscope (Fig. 2.5a, 2.5b and 2.5c). Despite the fact that different α gives different depth ranges, the PSFs generated with an $\alpha = 5\lambda$ and $\alpha = 7\lambda$ masks both closely exhibit parabolic lateral translations. For a peak modulation of three waves, the PSF translation begins to differ from a parabolic curve especially near the focal plane. Nevertheless, one can still conclude that the lateral translation exhibits a quasi-parabolic curve, especially at large defocus. To assess the PSF translation in non-paraxial scenarios, several imaging systems are simulated with different NAs and magnifications. The higher the NA, the larger the angle between the optical axis and the marginal ray collected by the objective. Thus, the paraxial approximation only holds for low NA systems. As shown in Fig. 2.5d and 2.5c, the PSFs exhibit a parabolic lateral translation for low NAs (0.3, 0.4). However, the PSF translation curve begins to differ from a parabola at 0.75 NA (Fig. 2.5e), i.e. a half angle θ of 48.6° which is a non-paraxial scenario (small-angle or paraxial approximation hold when $\theta < 30°$). The difference between the simulated translation and its parabolic fit becomes even more significant for a NA of 1.45 (Fig. 2.5f) where an oil immersion objective is assumed, the resultant PSF translation exhibits an obvious difference from a parabolic curve especially at large defocus. In spite of that, we can conclude that the z-dependant lateral translation of the AB-PSF for large NA differs from but still approximates a parabolic curve. The variation of the PSF translation from a perfect parabolic curve in the scenario of extremely high NA or small α does not preclude the utilization of the AB-PSF for 3D point localization as long as the semi-parabolic translation is well calibrated.

2.4.2 Optical setup

The experimental setup for the Airy-CKM technique was based on a commercial inverted microscope (*Nikon Eclipse* Ti). As discussed in chapter 1, the pupil plane of modern microscopes is conjugate to the back focal plane of the objective which usually lies inside the objective. Thus to modify the pupil function, we need to modify the objective or re-image the pupil plane using a $4f$ relay system. The following results in this chapter were acquired using a modified objective; results obtained using $4f$ relay will be discussed in the following chapters. As shown in Fig. 2.6, a 0.4 NA, 20× Plan Achromat objective was modified to accommodate a two-dimensional cubic phase mask using a 3D-printed holder. The phase mask has a peak modulation of $\alpha = 7\lambda$ and was located as close as practically possible to the pupil plane (in practice, the mask was placed by trial and error at the location where measured experimental PSFs were most similar to simulated PSFs).

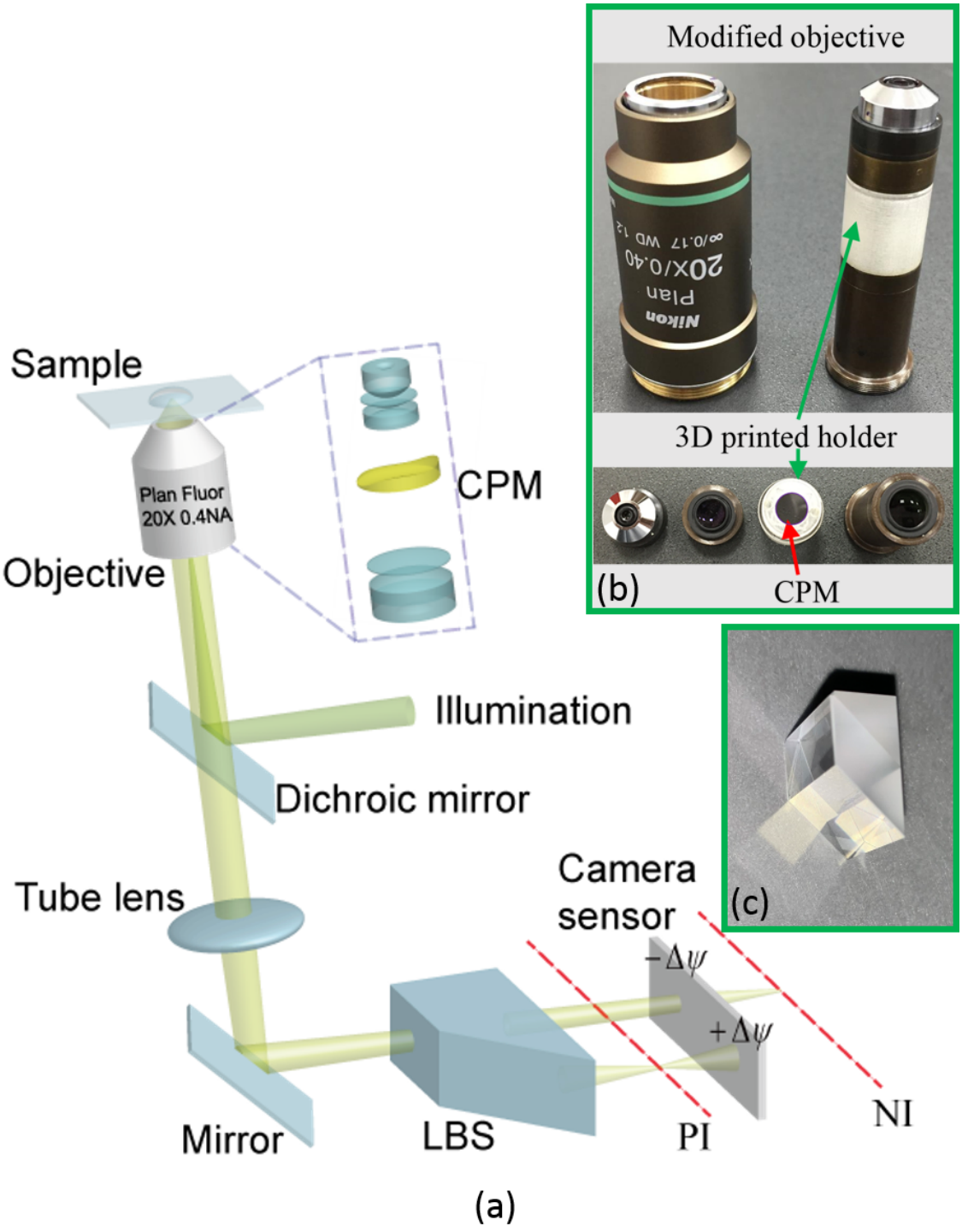

Fig. 2.6 (a) Experimental setup used for 3D particle localization and tracking with Airy-CKM technique. CPM: cubic phase mask; LBS: lateral beam splitter; PI: image plane of the positive imaging channel; NI: image plane of the negative imaging channel. The displacement between PI and NI for this setup was set to be 32 µm on the object side. (b) the 20×, 0.4 NA modified objective. The refractive phase mask was 7 mm×7 mm and mounted on a 3D printed holder with a circular aperture. The 3D holder and the mask was them mounted between the second and last lens groups of the objective. (c) the custom-made LBS. Fig. 2.6b adapted from Zhou et al., 2018[65], materials under Creative Commons licence CC BY.

The excitation illumination was provided by a fiber-coupled laser at 488 nm (Stradus VersaLase). The beam was focused on and diffused with a rotating ground glass and then collimated and focused at the back focal plane of the objective to launch wide-field illumination. A custom-made beam splitter was used to generate two imaging channels with defocus offsets of $+\Delta\psi$ and $-\Delta\psi$ which will be referred to hereon as the positive and the negative imaging channels respectively. The magnitude of $\Delta\psi$ was tunable by inserting glass slabs of certain thickness into one of the optical paths. Two encoded images with dissimilar defocus parameters were thus formed on the 2560×2160 pixel detector (*Andor Neo* 5.5 sCMOS camera with 6.5 µm pixel size), which can be processed using the algorithm described in the following section (2.4.3) to calculate the 3D location of each emitter.

Note that misalignment of the phase mask in the *xy* plane produces aberrations such as asymmetry in the PSF[83] (further discussion on phase mask misalignment, see section 3.5). The 3D-printed holder ensures, to some extent, that the phase mask was well aligned to the optical axis. Additionally, the calibration process can compensate for small misalignment between the phase mask and the actual pupil.

2.4.3 3D point localization algorithm

The discussions in the previous sections show that the TCD is a one-to-one function of the axial position of the emitter. Thus following initial calibration the absolute defocus and z coordinate can be calculated by comparing the *xy* coordinates of the emitters in the two imaging channels.

The algorithm used for the image-analysis pipeline is illustrated in Fig. 2.7. The inputs are the recorded images, I_C^+ and I_C^- from both channels. Firstly, they are deconvolved with their corresponding in-focus PSFs (i.e. PSF_{focus}^+ and PSF_{focus}^-, the PSFs recorded from both channels when the system is focused at the nominal $z=0$ plane) to yield their corresponding recovered images I_R^+ and I_R^-. These images exhibit compact profiles and approximate the in-focus DL-PSF, as has been shown in Fig. 2.1 and 2.4. This enables us to perform a 2D Gaussian fit (section 2.4.3) on I_R^+ and I_R^- to find the emitters' x,y coordinates in both channels. The TCD can be obtained by superimposing I_R^+ and I_R^- with the known mapping of the two imaging channels. The TCD together with calibration data (lookup tables are employed, experimental results will be discussed in section 2.3) enables the z coordinate to be deduced. Once z is determined for a particle, its x and y coordinates are corrected to account for the parabolic image translation of the AB-PSF. The true x and y coordinates are shifted by the amount depending on the z of the particle.

The x and y coordinates can be estimated from either imaging channel ((x^+,y^+) or (x^-,y^-)) since they are related by an affine transform used for the two-channel mapping that will be discussed in the following text.

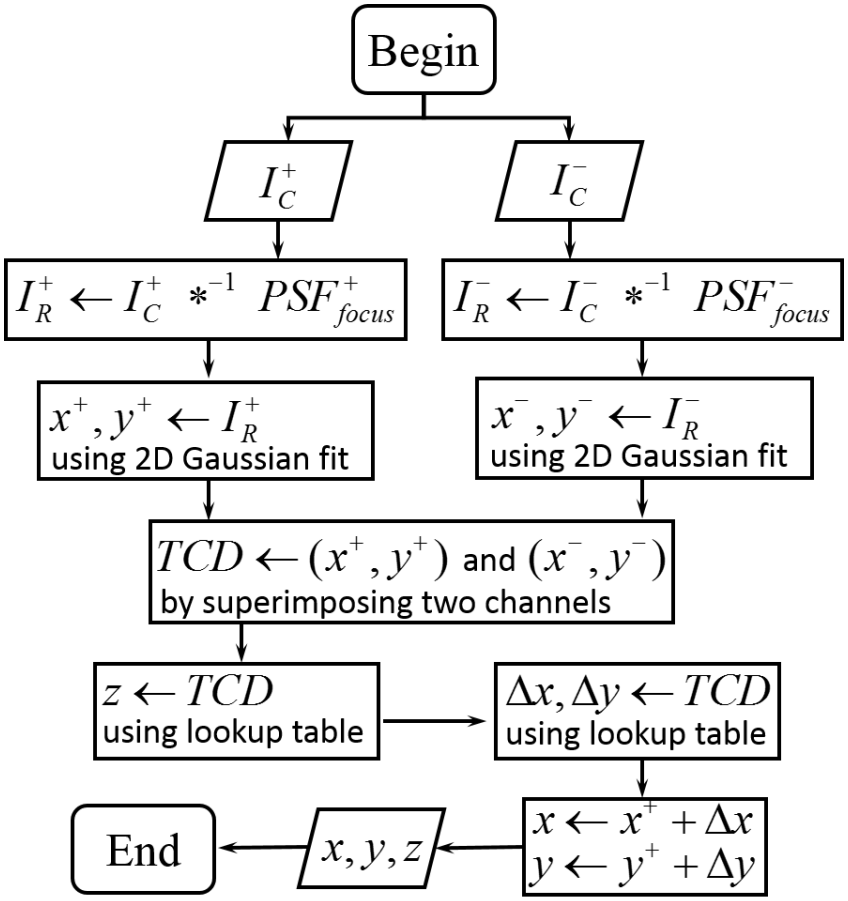

Fig. 2.7 Algorithm used for 3D particle localization using the Airy-CKM method. I_C^+ and I_C^- are the captured images from both channels; $*^{-1}$ refers to the Wiener deconvolution operator; PSF_{focus}^+ and PSF_{focus}^- are PSFs that have been pre-recorded using a sub-resolution emitter locating at the nominal object plane; I_R^+ and I_R^- are recovered images with Wiener deconvolution; Δx and Δy are the shifts in the x and y coordinates due to the PSF translations. Image adapted from Zhou et al., 2018[66], materials under Creative Commons licence CC BY.

Two-channel mapping

The calculation of the above mentioned TCD relies on the correct mapping of two imaging channels. The mapping of the two imaging channels can be performed by either imaging a layer of beads residing on the surface of a coverslip or by scanning a fluorescent bead in the nominal object plane throughout the field of view (FOV). It is more straightforward with the absence of the phase mask, however, since the phase mask may introduce other aberrations, it is preferred to map the two channels with the cubic mask in the optical path.

Fig. 2.8 shows an example of the two-channel mapping process with the presence of the cubic phase mask. The recorded images (Fig. 2.8a) were first deconvolved with PSF_{focus}^+ and PSF_{focus}^- to get the deconvolved images (Fig. 2.8b). After that, 2D Gaussian functions were fitted to the deconvolved images to obtain the 2D coordinates

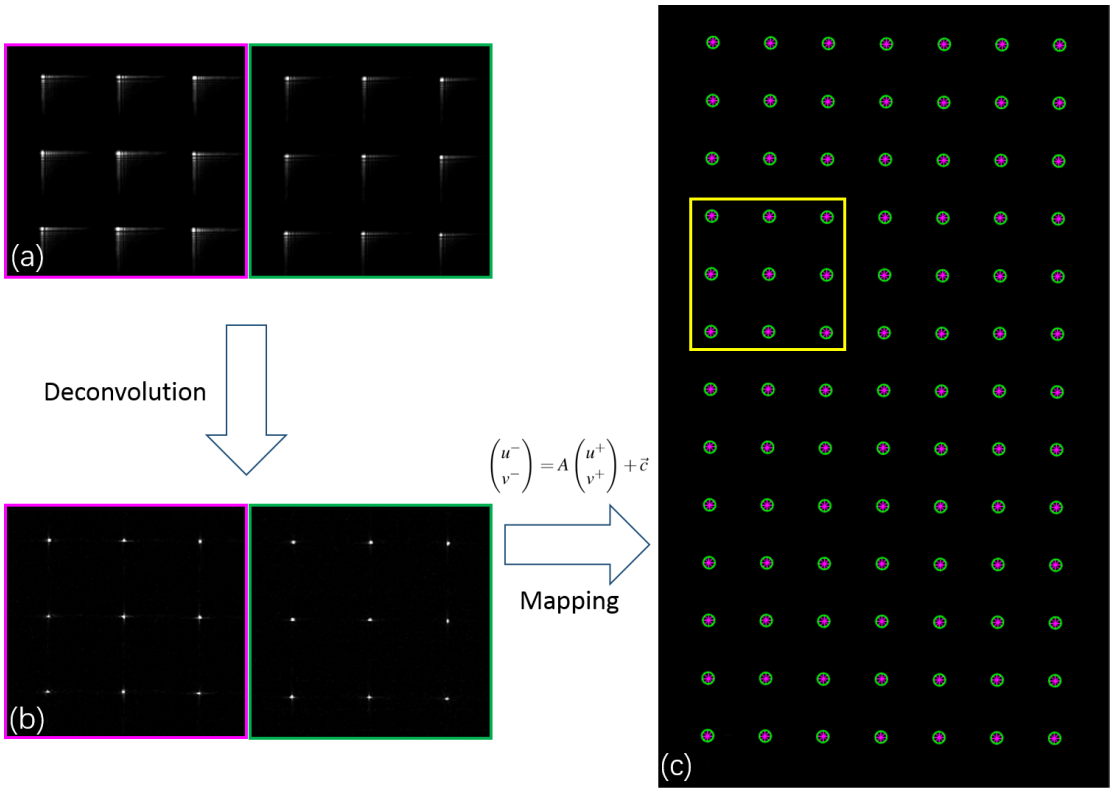

Fig. 2.8 Two-channel mapping process. Magenta indicates the positive channel and green indicates the negative channel. (a) The images recorded from both imaging channels of a single fluorescent bead with a motorized stage scanning in *xy*. (b) deconvolved images from both channels. (c) superimposition of the *xy* coordinates found in both channels using an affine transformation. To make the PSFs more obvious, the images shown in (a) and (b) are zoomed from a fraction of the whole field of view as indicated in the yellow rectangle in (c).

(x^+,y^+) and (x^-,y^-). In addition to the translation offset between the two channels, the slight difference in magnifications also needs to be accounted for. Therefore, an affine transformation was used to relate the two sets of coordinates. This transformation can then be considered as the two-channel mapping:

$$\begin{pmatrix} x^- \\ y^- \end{pmatrix} = A \begin{pmatrix} x^+ \\ y^+ \end{pmatrix} + \vec{c}, \tag{2.18}$$

where x^+ and y^+ refer to coordinates in the positive image (I_R^+) while x^- and y^- refer to the negative image (I_R^-). Point sources at the same depth yield equal image translations; as a result, although the 2D Gaussian fit on the deconvolved images does not give the true xy coordinate, the affine transformation still holds.

Fig. 2.8c shows the superimposition of (x^+,y^+) indicated with magenta asterisk and (x^-,y^-) indicated with green circle, which are obtained using the above mentioned transformation. The fact that they coincide within the whole FOV with an error smaller than 0.2 pixel indicates that an affine function is a sufficient description of the two-channel mapping. For systems that suffer from significant field dependence, a piece-wise affine function can be used as described in ref[81].

2D Gaussian fit

Two-dimensional Gaussian fit was used extensively in the algorithm to find the emitter coordinates in I_R^+ and I_R^-. Given an image of deconvolved AB-PSF, least-square fit was performed using the following 2D Gaussian function:

$$I = I_0 \times \mathrm{e}^{-\left(\frac{(x'-x_0)^2}{2\sigma_x'^2} + \frac{(y'-y_0)^2}{2\sigma_y'^2}\right)}, \tag{2.19}$$

where I_0 is the peak intensity, x' and y' are coordinates rotated by angle γ and x_0' and y_0' are centroids in the rotated coordinates:

$$\begin{aligned} \begin{pmatrix} x' \\ y' \end{pmatrix} &= \begin{pmatrix} \cos\gamma & -\sin\gamma \\ \sin\gamma & \cos\gamma \end{pmatrix} \begin{pmatrix} x \\ y \end{pmatrix} \\ \begin{pmatrix} x_0' \\ y_0' \end{pmatrix} &= \begin{pmatrix} \cos\gamma & -\sin\gamma \\ \sin\gamma & \cos\gamma \end{pmatrix} \begin{pmatrix} x_0 \\ y_0 \end{pmatrix}. \end{aligned} \tag{2.20}$$

I_0, x_0, σ_x', y_0, σ_y' and γ are the six parameters to be estimated. The ellipticity and the rotation are taken into account here because the deconvolved image of the AB-PSF is not circular symmetric, especially when the AB-PSF and its deconvolution kernel have a large mismatch in the amount of defocus.

2.5 Phase mask fabrication

As is shown in the previous section, this experiment employs a refractive phase mask to maximize the optical throughput of the imaging system. It is custom manufactured by Power Photonic Ltd on a UV-fused silica substrate using laser polishing, with anti-reflection coating after fabrication.

To design the cubic phase masks to a specific peak modulation (i.e. α), the pupil size of the imaging system needs to be known. This can estimated by either (1) using the formula $D_{pupil} \approx 2NAf_{obj}$, where f_{obj} is the focal distance of the objective lens; (2) measurement from experiment by imaging an on-axis point emitter and placing the camera at the re-imaged pupil plane; (3) measurement from experiment by imaging an on-axis point emitter and phase retrieval. As will be further discussed in section 3.4, a phase mask that is mismatched to the pupil size can produce a different phase modulation from desired. Matching of pupil size to the phase mask is more critical to some techniques than others. For example, pupil size matching for the cubic phase mask is more flexible because a cubic mask that is designed to be bigger than the actual pupil size is effectively a weaker cubic phase mask; For other masks such as the double-helix mask and the tetrapod mask, however, it is less flexible as they have to be matched to the actual pupil size.

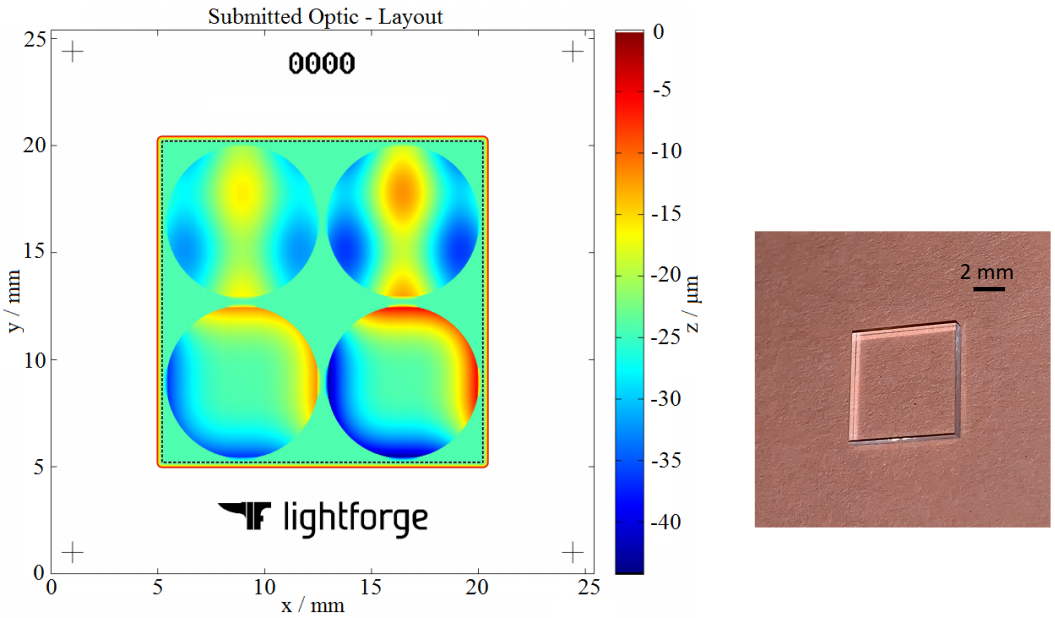

(a) (b)

Fig. 2.9 (a) An example of the phase mask designs. The clear optical aperture size is 15 mm × 15 mm where two cubic phase masks (lower row) and two 'twin-Airy' phase masks (upper row) with different strength are displayed. (b) A ready-diced and anti-reflection-coated phase mask that was manufactured by Power Photonic.

The sampling rate required for fabrication is 10 µm, thus the designed phase mask is sampled to a 10 µm × 10 µm grid. Each pixel can then be laser polished to the thickness

that introduces the desired wavefront modulation. Fig. 2.9a shows an example of the phase mask designs. The typical pupil diameters for the microscope objectives used in this work are below 6 mm while the dimension limit for the fabrication process is 15 mm $\times$ 15 mm. To make full use of the silica substrate, we place four mask designs on one substrate and then dice them after fabrication and anti-reflection coating. In this example, there are two cubic phase masks and two 'twin-Airy' phase masks (this will be introduced in chapter 3). Fig. 2.9b shows a phase mask after dicing. The substrate has a thickness of 1 mm, thus the dimension of the diced phase mask is around 7 mm $\times$7 mm$\times$1 mm.

2.6 Proof-of-concept experiment and discussions

Before applying the proposed technique to biomedical applications, some proof-of-concept experiments were performed as a validation. This section assesses the extended depth range and the depth-dependant translation associated with the AB-PSF and the deconvolved AB-PSF. Measurement of fluid flow that is seeded of fluorescent beads within capillaries made of fluorinated ethylene propylene (FEP) will also be shown as a proof-of-concept of the Airy-CKM technique.

2.6.1 Assessment of PSF translation and extended depth range

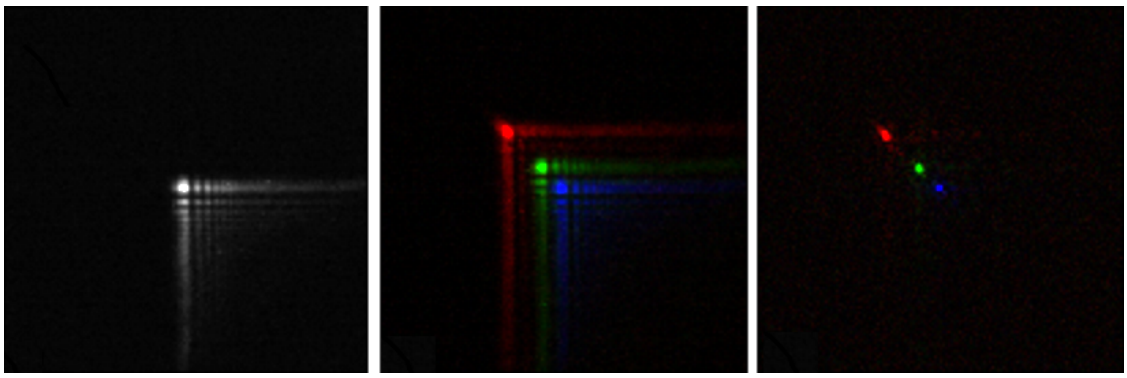

(a) (b) (c)

Fig. 2.10 (a) Image of a single in-focus bead (i.e. the PSF). (b) Superimposed images of the same bead with z displacements Δz=0 (blue), 30 µm (green) and 60 µm (red) respectively. (c) Deconvolved images of the same bead at the mentioned depths with an in-focus PSF as the deconvolution kernel. Image adapted from Zhou et al., 2018[65], materials under Creative Commons licence CC BY.

It has been shown that the AB-PSF yields depth-dependant lateral translation both theoretically and by numerical simulation. In this section, the focus is on experimental assessment of this PSF translation.

An experimental AB-PSF, acquired with the 20×, 0.4NA system using a single in-focus fluorescent bead (Bangs Laboratories, Inc. FS03F 10999, emitting peak at 520 nm), is shown in Fig. 2.10a. The *xy* axes of the cubic phase mask were aligned with the rows and columns of the detector array so that the two arms of the 'L'-shaped PSF are parallel to the image edges. As the defocus increases, this PSF translates along the image diagonal, which is illustrated in Fig. 2.10b. The z displacements of the bead with respect to the in-focus plane were 0 (blue), 30 µm (green), 60 µm (red) respectively. Fig. 2.10c shows the images of the bead recovered from the recorded images in Fig. 2.10b using a Wiener deconvolution with the PSF in Fig. 2.10a being the deconvolution kernel. As predicted in equation 2.13, the in-focus image (blue) yields no lateral translation in the recovered image as it was deconvolved with the in-focus AB-PSF. However, the defocused images were deconvolved with a PSF for different defocus (also the in-focus PSF) thus exhibiting the expected translations (green and red).

The PSF translations from both imaging channels are measured against depth (Fig. 2.11) by scanning a fluorescent bead along the optical axis using a translation stage. The vertex of the parabola corresponds to the actual in-focus plane of corresponding imaging channel, where the lateral translation rate is zero. The nominal $z = 0$ plane was set near the middle of two focal planes, which are about 32 µm away from each other in the object space as can be seen from Fig. 2.11a and 2.11b. The PSF translations in x and y are independent and the amount of translations in the two directions are theoretically the same. However, they have slight differences in practice because unavoidable minor angular nonalignment in the orientation of the principle axes of the cubic phase mask (and hence the PSF) with the detector array of the camera. There are other aberrations in the imaging system. For example, an additional astigmatism will separate the parabola vertices in the x and y directions. Nevertheless, calibration can compensate for these slight aberrations.

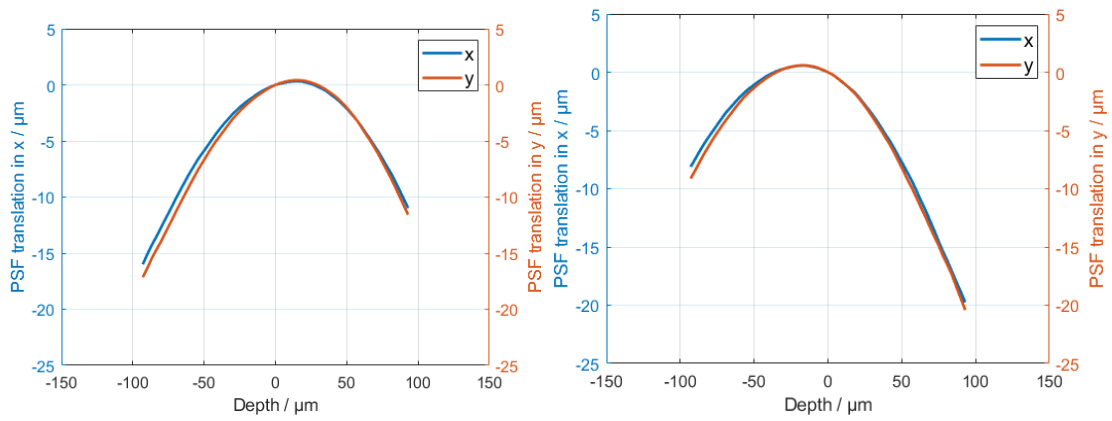

(a) positive imaging channel (b) negative imaging channel

Fig. 2.11 The lateral translation curves from both the imaging channels, which can be used as lookup tables for the 3D localization algorithm (section 2.4.3). Blue and orange curves correspond to the x and y translations respectively.

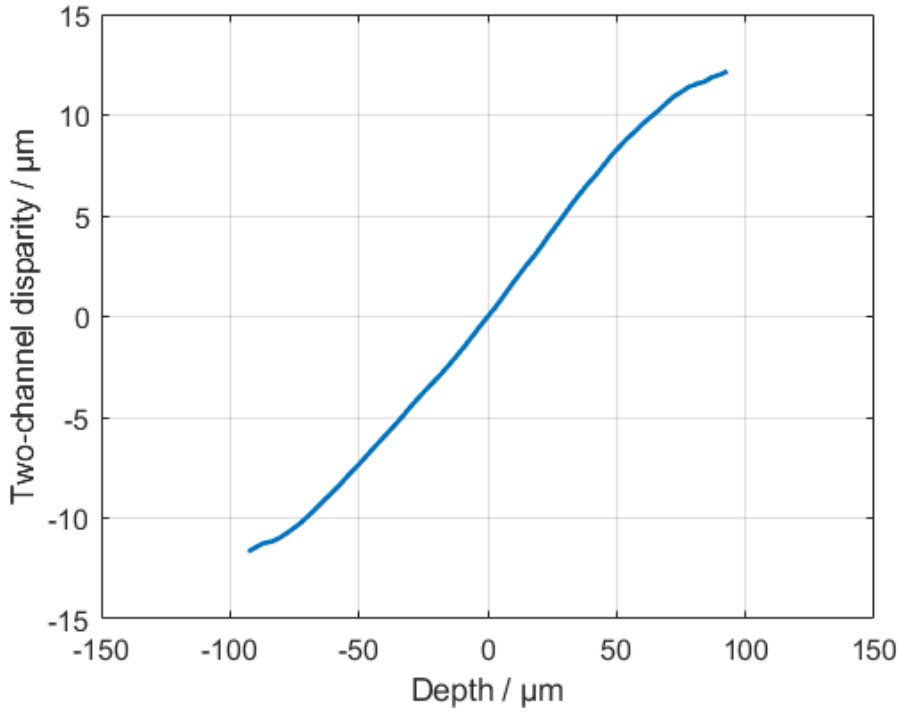

Fig. 2.12 Relation between the two-channel disparity and depth. This is the calibration look-up table for determination of the z coordinates.

Given the lateral translation from both imaging channels, the TCD can be deduced with the known mapping between the two imaging channels. Fig. 2.12 shows the calculated TCD. As can be observed, the curve is a monotonic function over the extended depth range of about 200 µm meaning any particle within this range can be localized with the algorithm described in section 2.4.3 without ambiguity. The quasi-linearity of the curve gives a uniform z-responsivity over the whole depth range. This proves the validity of the analysis in the previous sections. As described in the 3D localization algorithm, this curve is used as a lookup table for determining the z coordinate from the TCD. Note that the xy coordinates obtained from the deconvolved images I_R^+ and I_R^- do not reflect the actual xy position of the emitter in the object space, because the xy coordinates are associated with the z-dependent lateral translation. Thus, once the z coordinate is known, the shifts in the x and y need to be determined from the xy translation curves (Fig. 2.11a and 2.11b) to make corrections on the centroid xy coordinates accordingly.

To assess the extended depth range provided by the AB-PSF and the deconvolved AB-PSF we compare with the DL-PSF and the astigmatic PSF. Fig. 2.13a shows an experimental comparison of these PSFs over a depth range of 150 µm (the deconvolved PSFs are the corresponding AB-PSF deconvolved with the in-focus AB-PSF). As expected, the conventional DL-PSF forms a high-peak-intensity Airy disk at its focal plane. However, it expands rapidly in size and decreases in intensity with the increasing defocus; this results in a very limited depth range (the displayed intensity is re-scaled non-linearly to make the out-of-focus DL-PSFs visible). The astigmatic PSF generated with a cylindrical lens

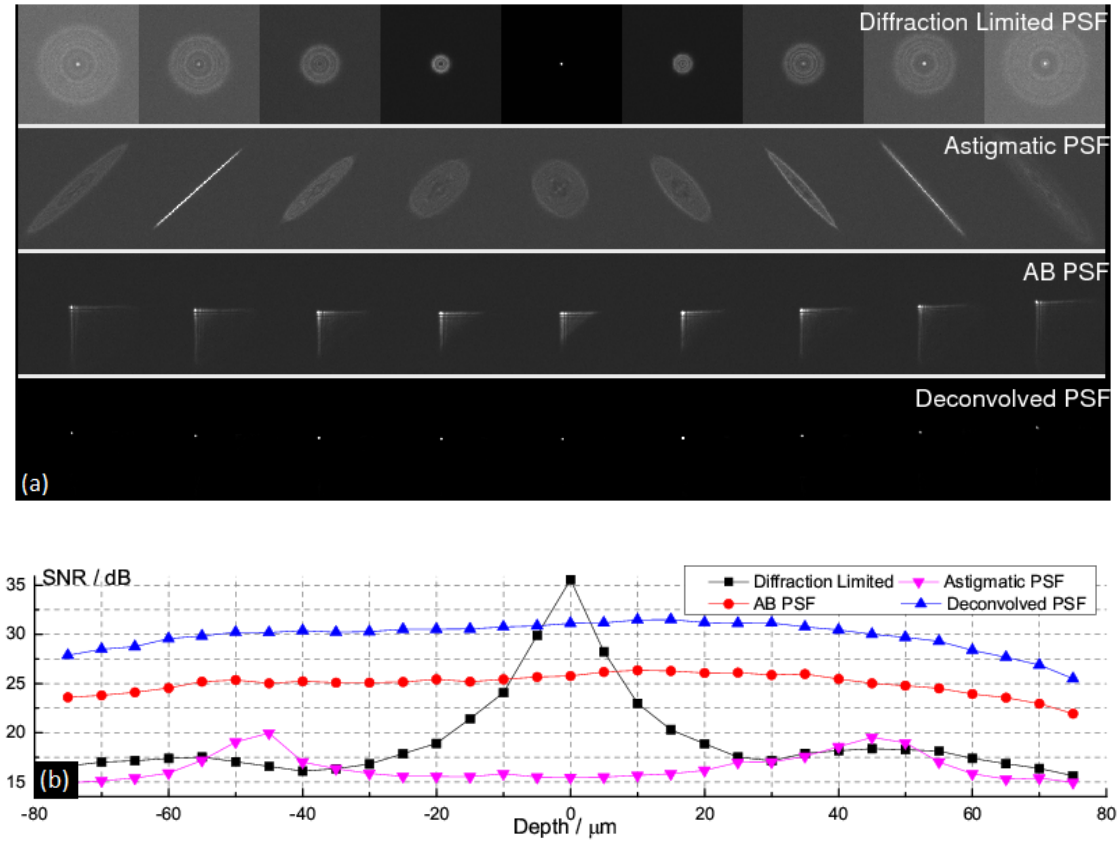

Fig. 2.13 (a) Comparison of the diffraction-limited PSFs, the astigmatic PSFs, the Airy-beam PSFs (AB-PSF) and the deconvolved AB-PSFs over a depth range of 150 µm, the depth of each PSF can be read from the x axis in (b). The intensity of the diffraction-limited PSFs has been rescaled non-linearly to make the patterns visible. The cylindrical lens for generating the astigmatic PSF has a focal length of 1000 mm. (b) SNR comparison of the different PSFs in dB. Images adapted from Zhou et al., 2018[65], materials under Creative Commons licence CC BY.

exhibits two focal planes. The PSF profile yields a continuous variation (i.e. in ellipticity and orientation) with the changing defocus. Similar to the DL-PSF, the astigmatic PSF expands severely with defocus making it unsuitable for imaging of thick samples. In contrast, the AB-PSF changed little (not only in its form but also in its intensity) over the whole depth range except for the expected translation. Consequently, following image deconvolution, a compact PSF can be recovered for an extended depth range as shown in Fig. 2.13a.

Fig. 2.13b shows the variations in the SNR of the above experimental PSFs as a function of depth. The definition $SNR = 20\log_{10}(I_m/\sigma_b)$ is employed in the calculations, where I_m is the maximum recorded intensity, and σ_b is the standard deviation of the background noise[84, 85]. The DL-PSF exhibits the highest SNR close to the focal plane but the SNR reduced rapidly with depth due to the rapid increase in size. Compared to the DL-PSF, the astigmatic PSF displays higher SNR at its two focal planes which are determined by the sagittal and tangential focal lengths of the imaging system. Its SNR is comparable to that of the DL-PSF when both are defocused. Conversely, the SNR of the AB-PSF is approximately constant and significantly higher than that of the above-mentioned techniques over the entire depth range with the exception of a 16 µm region around the focal point where the DL-PSF has a higher SNR. Furthermore, following deconvolution, the SNR is increased further and the region where the DL-PSF has a better SNR is reduced to only 7 µm. This clearly demonstrates that the AB-PSF and the deconvolved AB-PSF provide the highest SNR and hence most precise particle localization for operation over an extended depth range.

2.6.2 3D particle-tracking velocimetry in laminar flow

We discuss now the application of the Airy-CKM technique to the measurement of a microfluidic flow in an FEP capillary. FEP is popular as a sample holder material in microscopy applications as its refractive index is close to that of water at visible wavelengths (FEP: 1.344, water: 1.335), minimizing the refractive aberrations in imaging. 0.96 µm fluorescent beads (Bangs Laboratories, Inc. FS03F 10999) were suspended in water and a syringe pump was used to generate a steady laminar flow within the FEP capillary. Part of the FEP capillary was laid flat on the microscope cover slip and was immersed in saline (Fig. 2.14a). The concentration of the saline was adjusted so that the FEP capillary was almost invisible to match its refractive index, effectively eradicating refraction and Fresnel reflections. Fig. 2.14b shows a snapshot image of the fluid flow seeded with fluorescent beads. The FEP capillary was aligned roughly to one edge of the camera sensor so that the flow field was along y direction. It had an inner diameter of 150 µm and about 700 µm of its length was within the FOV of the microscope. I_C^+ and I_C^- are the PSF-encoded images from both imaging channels. Each AB-PSF indicates a

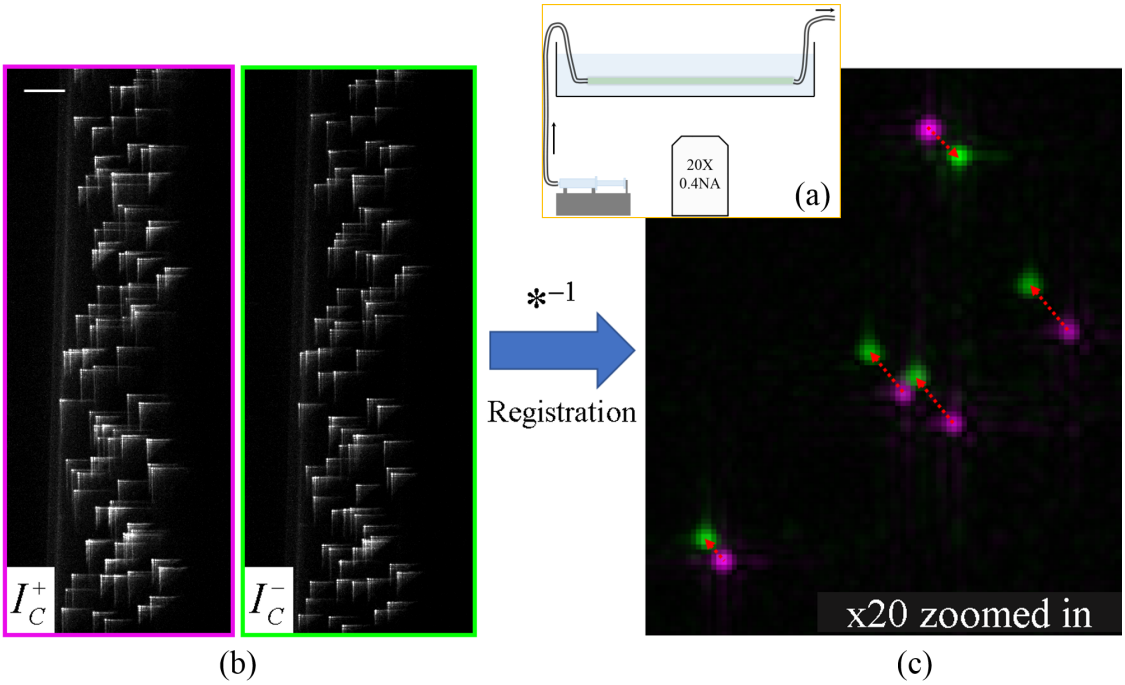

Fig. 2.14 (a) Schematic of the laminar flow imaging configuration. (b) A snapshot of a steady laminar flow seeded with 0.96 µm fluorescent beads in an FEP capillary with a nominal inner diameter of 150 µm. The image is encoded with the AB-PSF and the scale bar is 50 µm. (c) Corresponding deconvolved images I_R^+ and I_R^- superimposed after two-channel mapping with magenta spots denoting the images recovered from positive imaging channel and green spots from the negative, 20 times zoomed in. The red arrows are the calculated image disparities. Image adapted from Zhou et al., 2018[65], materials under Creative Commons licence CC BY.

tracer bead flowing in the fluid flow. Following image deconvolution with the in-focus PSF and image registration with the known two-channel mapping (section 2.4.3), we can superimpose the two deconvolved images, I_R^+ and I_R^-, to find the TCD for each tracer bead as shown in Fig. 2.14c. The green and magenta dots correspond to recovered images from the positive and negative channels respectively and the red arrows indicate the calculated TCD. As can be observed, the disparities between the recovered bead images from the two channels have a range of magnitudes and directions indicating that the beads vary in axial displacements. The recorded and deconvolved PSFs can be seen to have forms that are independent of range as expected. Given the calibration curves in Fig. 2.11 and 2.12, the *xyz* coordinates of each tracer bead can then be deduced from its TCD.

The deconvolved image of a bead exhibits a compact profile that approximates the in-focus DL-PSF, as can be appreciated from Fig. 2.14c; thus, a higher seeding concentration can be obtained compared to techniques employing a spatially expanding PSF such as astigmatism (for a similar depth range). Even though the recorded PSF-encoded images overlap severely as in Fig. 2.14b, the recovered bead images are well isolated as in Fig. 2.14c. In this experiment, the orientation of image disparities is along the unity-slope line, which can be used as a criterion to unequivocally pair positive and negative images

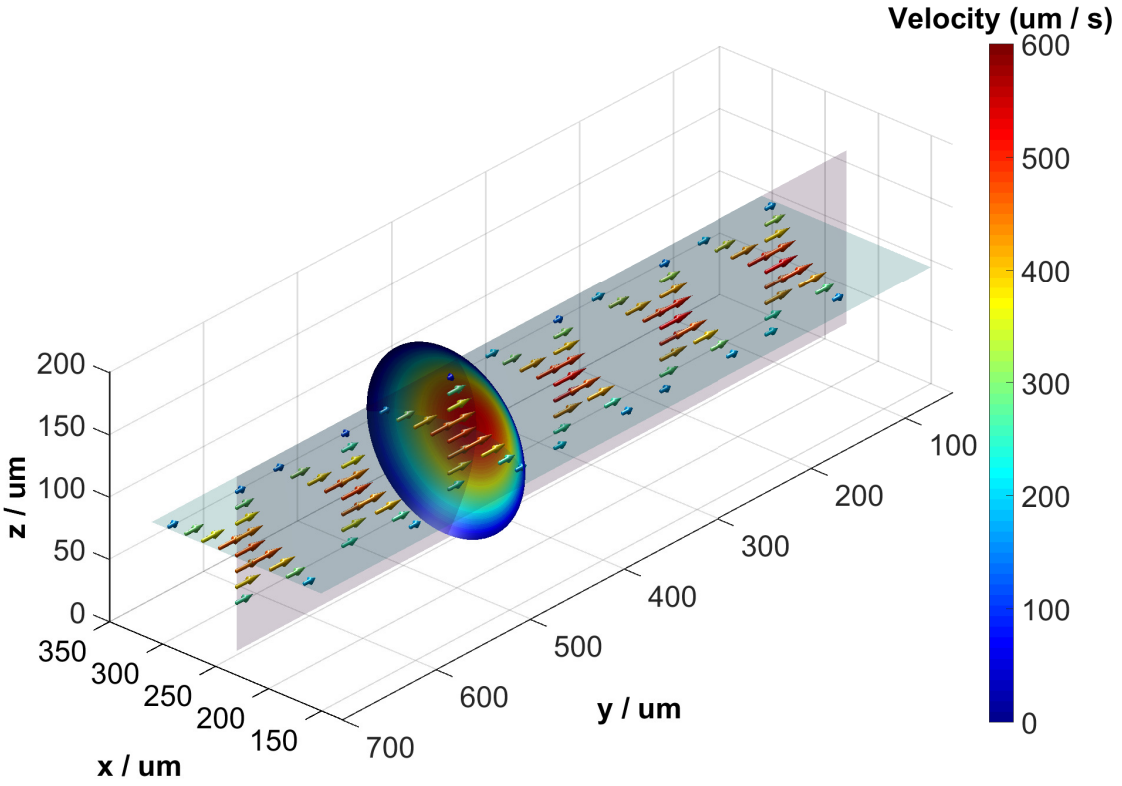

(a)

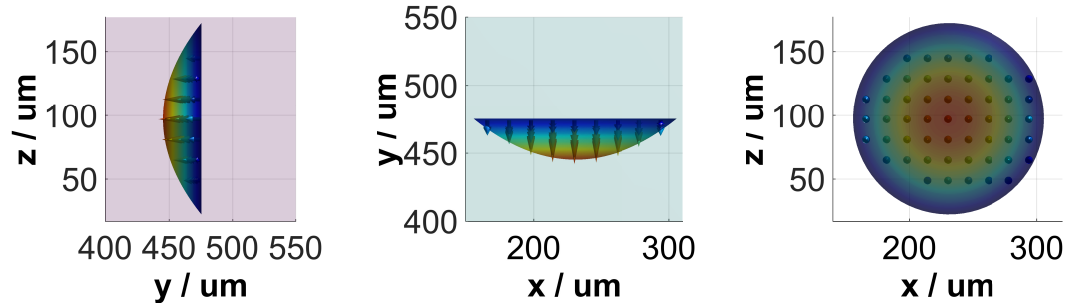

(b)

Fig. 2.15 (a) 3D velocity field of a steady laminar flow generated in an FEP capillary with a nominal inner diameter of 150 µm, obtained by averaging 4000 frames. Vectors on two perpendicular slices are shown, and the color map indicates velocities from 0 to 600 µm/s. The parabolic curve is a least-squares fit to the velocity vectors at that cross-section with (b) its three projections shown below. Adapted from Zhou et al., 2018[65]. Materials under Creative Commons licence CC BY.

of a single particle: for example the bead images clustered in the center of Fig. 2.14c can be paired on this basis as indicated.

With the tracer beads in each frame localized in 3D space, the 3D velocity field can be deduced from tracer displacements if the tracer trajectories can be determined through several successive frames. Many algorithms have been proposed for frame-to-frame particle tracking, in this work the technique developed by Crocker and Grier[86] was used, which is robust when the maximum displacement of particles between frames is less than the mean spacing between the particles. As a demonstration of the application and validity of this technique, the 3D velocity field of the above mentioned laminar flow has been calculated, confirming measurements in line with predictions.

The whole detection volume is divided into small voxels, each tracer bead passing a specific voxel contributes to the average velocity vector of that voxel. Fig. 2.15 shows the measured 3D velocity field for the fluid flow generated in the 150 µm FEP capillary as described above. As required, the measured locations of all beads were within the capillary inner volume as determined from bright-field images. Since the beads were relatively small and light, they did not disturb the laminar flow significantly. Consequently, the velocity profile is expected to be parabolic and is given by[87]:

$$v(r) = v_m \left(1 - r^2/R^2\right), \tag{2.21}$$

where v_m is the maximum velocity, r is the radial coordinate and R is the radius of the capillary. Least-squares fit of $v(r)$ yielded the profile shown in Fig. 2.15 together with its three orthogonal projections, which are in agreement with the expected parabolic form. The inner radius $R = 74.07\,\mu\text{m}$, obtained from curve fitting, matches the nominal inner radius of the capillary of 75 µm with an error of 1.2 %. Furthermore, we calculated $v_m = 553\,\mu\text{ms}^{-1}$ which gives a volume flow rate that is within 5 % of the value programmed into the syringe pump.

2.6.3 Flow tracking in twisted capillary

In addition to the PTV measurement of a laminar flow, where the motions of particles were along a constant direction, we also tracked tracer beads in a 3D bidirectional flow as a further demonstration. This was generated in two FEP capillaries that were mutually twisted to form a double helix. The flow field inside such a structure therefore yields both xy and z components. The same optical setup was used to image the bidirectional flow and half a period of the double helix structure was within the 400 µm × 700 µm × 150 µm detecting volume as shown in Fig. 2.16a. Similarly, the capillary was stabilized on a coverslip and immersed in saline to match the refractive index of the FEP capillary

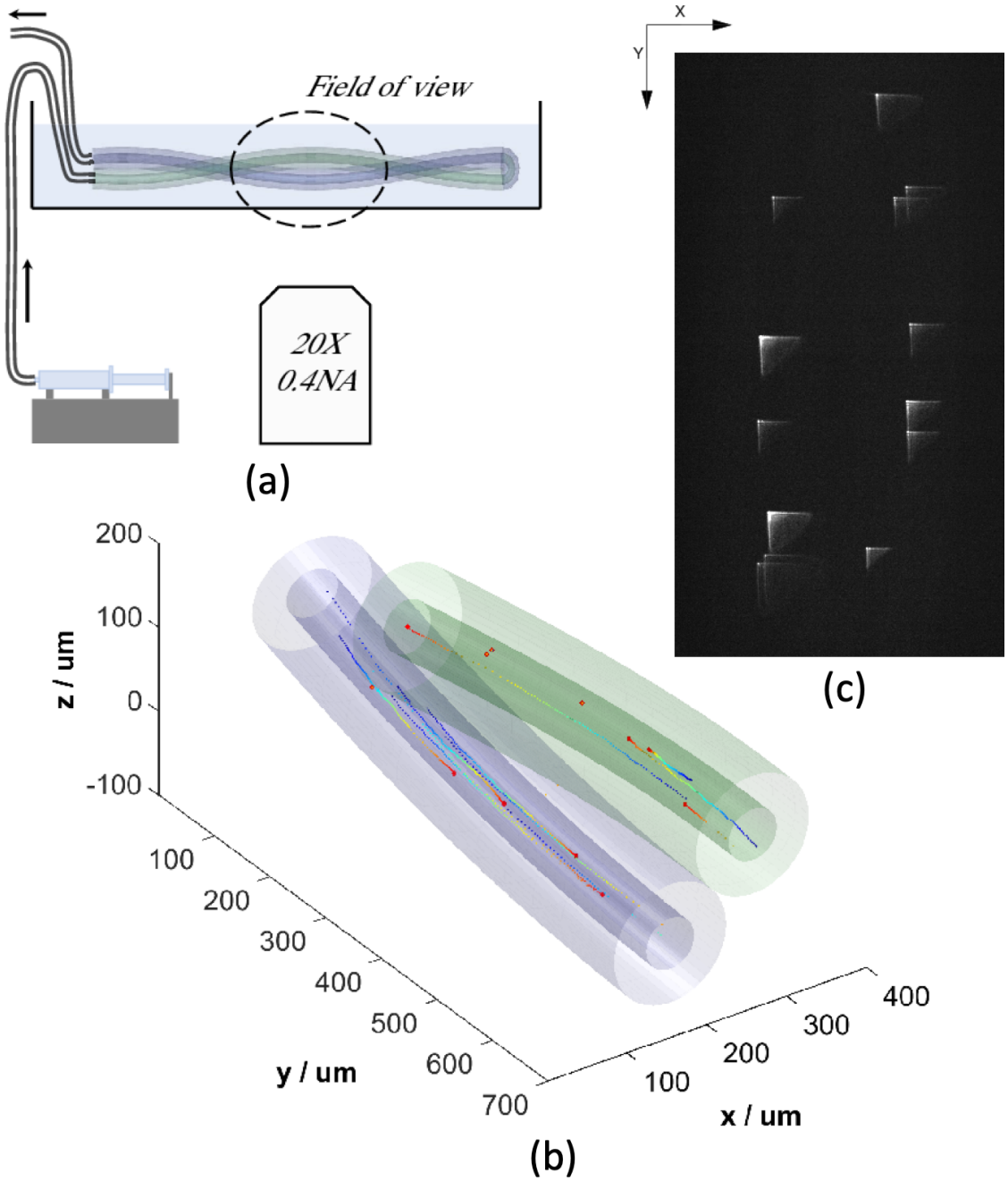

Fig. 2.16 Flow tracking in a twisted FEP capillary. (a) Twisted capillary configuration. The capillary had an inner diameter of about 50 µm and an outer diameter of about 140 µm. The capillary was immersed in salt water to match its refractive index. The optical setup was the same as described in Fig. 2.6. (b) Fluorescent bead trajectories in twisted capillary within 100 successive frames. Different color denotes the time with dark blue being the first frame and dark red being the last frame. (c) Image of the last frame captured by the positive imaging channel. Adapted from Zhou et al., 2018[65]. Materials under Creative Commons licence CC BY.

and minimize refractive aberrations. Fig. 2.16b shows the flow tracking of ten trajectories calculated from 100 successive frames. The hues of the trails, varying from dark blue to dark red, indicate the time evolution of their paths which clearly show the *xyz* components within the helical capillaries. A relatively large red spot indicated at the end of each trajectory was from the last frame as shown in Fig. 2.16c. The 3D locations were extracted from the 2D image sequences; thus, every bead in Fig. 2.16b has a corresponding PSF-encoded image in Fig. 2.16c. A video of this experiment is published online with ref[65].

2.6.4 Tracking of magnetic beads

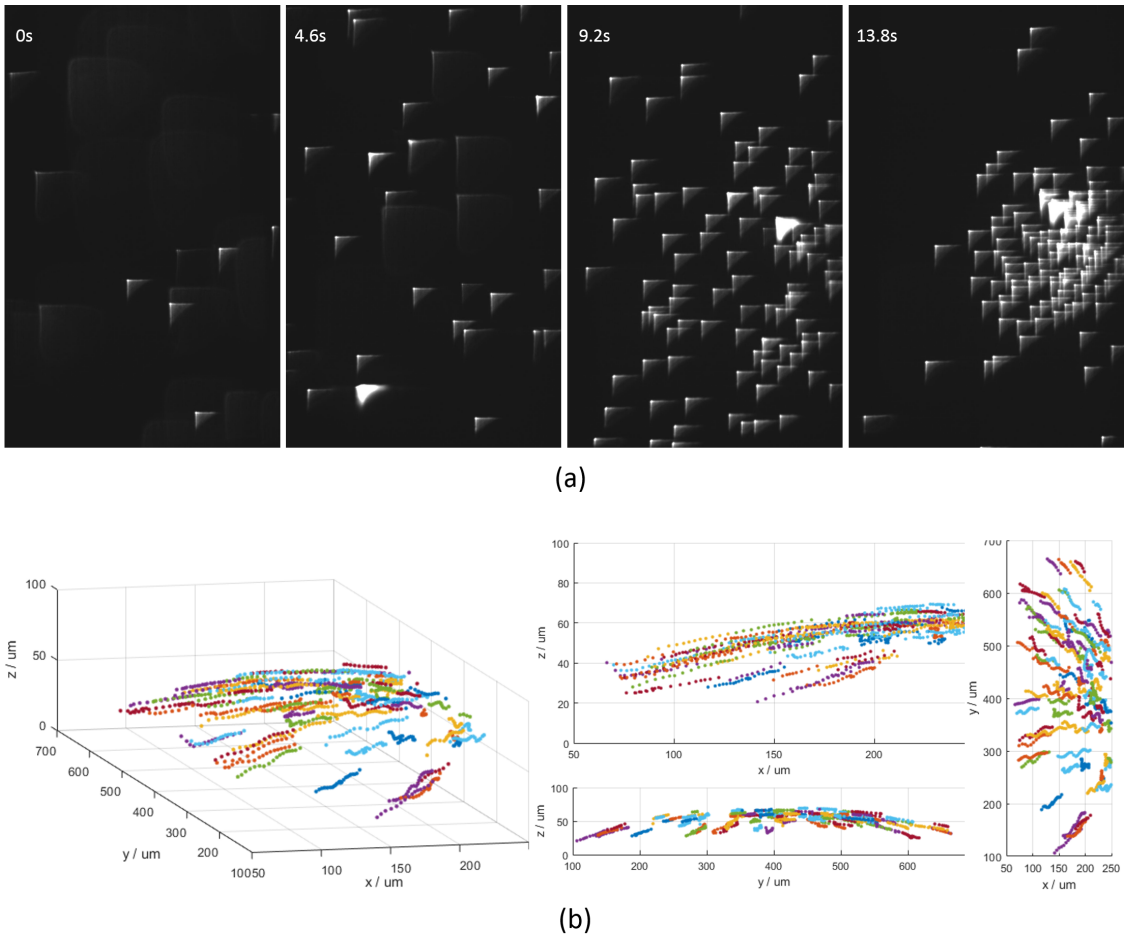

Fig. 2.17 Results of the magnetic bead experiment. (a) Raw images from the positive imaging channel at various time points. Some beads form clusters and appear as saturated pixels, which are rejected in the post processing. (b) Multi-views of the bead trajectories obtained from the video, each color indicate the trajectory of a single bead.

Another illustrative experiment was performed using 2.85 µm magnetic beads (Bangs Laboratories, Inc. UMC3F) dissolved in a drop of phosphate-buffered saline (PBS) solution on a coverglass. At the beginning of the experiment, the magnetic beads were allowed to settle down to reside on the surface of the coverglass. Then a neodymium

magnet was used to attract the beads, so that they can yield movement in the z direction. The magnet was also shaken in the y direction on purpose. The whole process was imaged at 10 fps, and the images were then processed to reconstruct the trajectories of the beads.

Fig. 2.17a shows raw images of the magnetic bead from the positive imaging channel at four time points. The microscope was focused deep into the liquid drop to image its top surface (recall that an inverted microscope was used here), thus at the beginning most of the beads appeared to be faint (0s and 4.8s) as they were on the surface of the coverslip and out of the detection range. In response to the magnetic field, the beads rose in z gradually into the detection range and gathered towards the right of the FOV where the magnet was placed. The corresponding bead trajectories are shown in Fig. 2.17b in multiple views where we can clearly see a change in their z coordinates as they were attracted by the magnet and rose to the surface of the liquid drop. The oscillation in y due to the movement of the magnet was also expected. Additionally, longer exposure to the magnetic field will result in magnetization among beads, causing them to react to each other such as attraction, repulsion, line-up and change of orientation.

2.7 Localization precision analysis

A figure of merit in point localization microscopy is the repeatability, or in other word the localization precision, defined as the standard deviation of a number of repeated measurements. Many factors affect the achievable precision including the SNR. To assess the precision of this experimental implementation, we measured the 3D-localization precision as a function of SNR and depth. The standard deviations dropped with increasing SNR as illustrated in Fig. 2.18a. For an SNR of 43.6 dB, the x, y and z precisions reached 5.1 nm$\times$4.9nm$\times$48.8 nm and for an SNR of 46.5 dB, an axial precision of better than 30 nm was recorded. The three histograms in Figs. 2.18c-2.18e show the distributions of the estimated x, y and z locations for 100 measurements of a single bead ($\Delta z = 0$, SNR=43.6 dB) together with the Gaussian fits to the distributions. Similar to most reported experiments, the z precision is worse than the x and y precision, since the changing rate of disparity with axial position is relatively small (about 0.15, as can be seen from Fig. 2.12). As discussed in section 2.3, this responsivity is tunable by changing the ratio of the focal difference $\Delta\psi$ to the cubic parameter α.

The variation of precision with z is shown in Fig. 2.18b. The rapid degradation for $|z| >$60 µm is associated with the limits of the axial range for invariance of the Airy-beam PSF and modulation-transfer function[88]. Due to the depth-insensitivity of the Airy-beam PSF, an approximately constant precision of better than 50 nm over an extended range of 120 µm can be achieved in z with an in-focus SNR of 46.5 dB, and a sub-100 nm precision can be expected over a range of 140 µm. This is more than 20-fold larger than the nominal DOF (about 5.8 µm) of the objective.

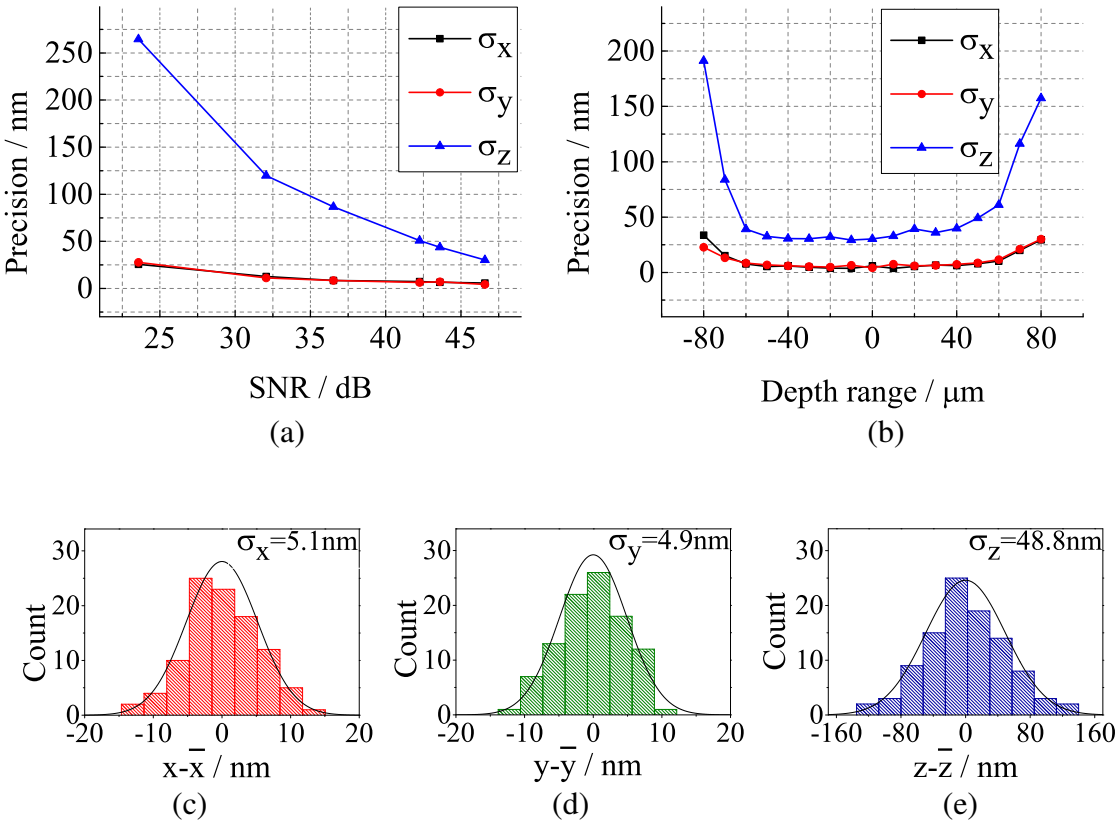

Fig. 2.18 Repeatability analysis from 100 measurements for each z position and each SNR. (a) Standard deviations of the x, y and z localizations of the same bead at the focal plane as a function of SNR. (b) x, y and z standard deviations of the same bead throughout a depth range of 160μm with an in-focus SNR of 46.5dB. (c) (d) (e) Histograms of the x, y and z coordinates of the same bead at focal plane with SNR=43.6dB. Images adapted from Zhou et al., 2018[65], materials under Creative Commons licence CC BY.

Note that the SNR is emitter dependent: parameters like the emitter size and quantum yield affect the SNR and thus the localization precision. For emitters significantly bigger than the optical resolution of the system, the recovered image will become extended, reducing precision for equal number of detected photons; but the higher photon flux expected for larger emitters will tend to introduce a compensating increase in SNR and precision. The NA of the system determines the optical resolution and is a salient parameter for both the depth range and the localization precision: a lower NA gives an increased depth range, but fewer signal photons are collected resulting in a lower SNR and thus a worse precision. For applications in which single molecules are used as emitters, the number of photons collected are usually limited thus high NA, high magnification and more sensitive sensor such as EMCCD are typically used.

2.8 Sampling of the PSF and choice of emitter size

The PSF has a spatially continuous profile, however, it can be sampled only as a discrete matrix due to the pixelation of the camera detector. It is thus important to make sure the PSF sampling preserves the fine structures in its profile, especially for image deconvolution purposes.

According to Abbe's law, the numerical aperture NA and the emitting wavelength from the sample determine the resolution and the PSF size of the imaging system: $\lambda/2NA$. The Nyquist sampling theorem requires the pixel on the detector in the image space to be smaller than half of this resolution limit; or equivalently, the sampling frequency needs to be twice the cutoff frequency of the imaging system to achieve its full resolving power. Given a fixed pixel pitch, the magnification can be adjusted to achieved Nyquist sampling rate. Therefore, the NA and the magnification of the microscope objectives are usually weakly coupled to meet this requirement: Higher numerical aperture objectives usually has a higher magnification. Modern scientific cameras and microscopes are designed to achieve Nyquist sampling. However, when pixel binning is used to increase peak signal level or image acquisition speed, it is worth checking if high spatial frequency is lost, i.e. aliasing is occurring.

In addition to the Nyquist sampling considerations, the size of the emitter used for measuring the PSF also needs to be chosen according to the resolving power of the imaging system. The image of an emitter that is smaller than the resolution (or the diffraction limit) can be considered as the PSF of the imaging system; the image of an emitter bigger than the diffraction limit is a convolution of the shape of the bead with the PSF. Therefore, sub-diffraction emitters need to be used to record the actual PSF of the imaging system.

The deconvolution kernel in the image recovery is ideally the actual PSF of the imaging system. For particle localization purposes, however, the image of an emitter that is similar to or bigger than the diffraction limit may also be utilized as the PSF because only the centroid of the emitter's image is of concern. Assume an emitter is bigger than the diffraction limit, the deconvolution of its image with itself yields a delta function, resulting in the same centroid as its image deconvolved with the actual PSF of the imaging system.

2.9 3D point localization using a single AB-PSF

In the previous sections of this chapter, we employed a bi-plane arrangement (the Airy-CKM technique) to deduce the lateral translations of the AB-PSF, thus to calculate the *xyz* coordinates of the emitter. It is worth noting here that it is also possible to localize point

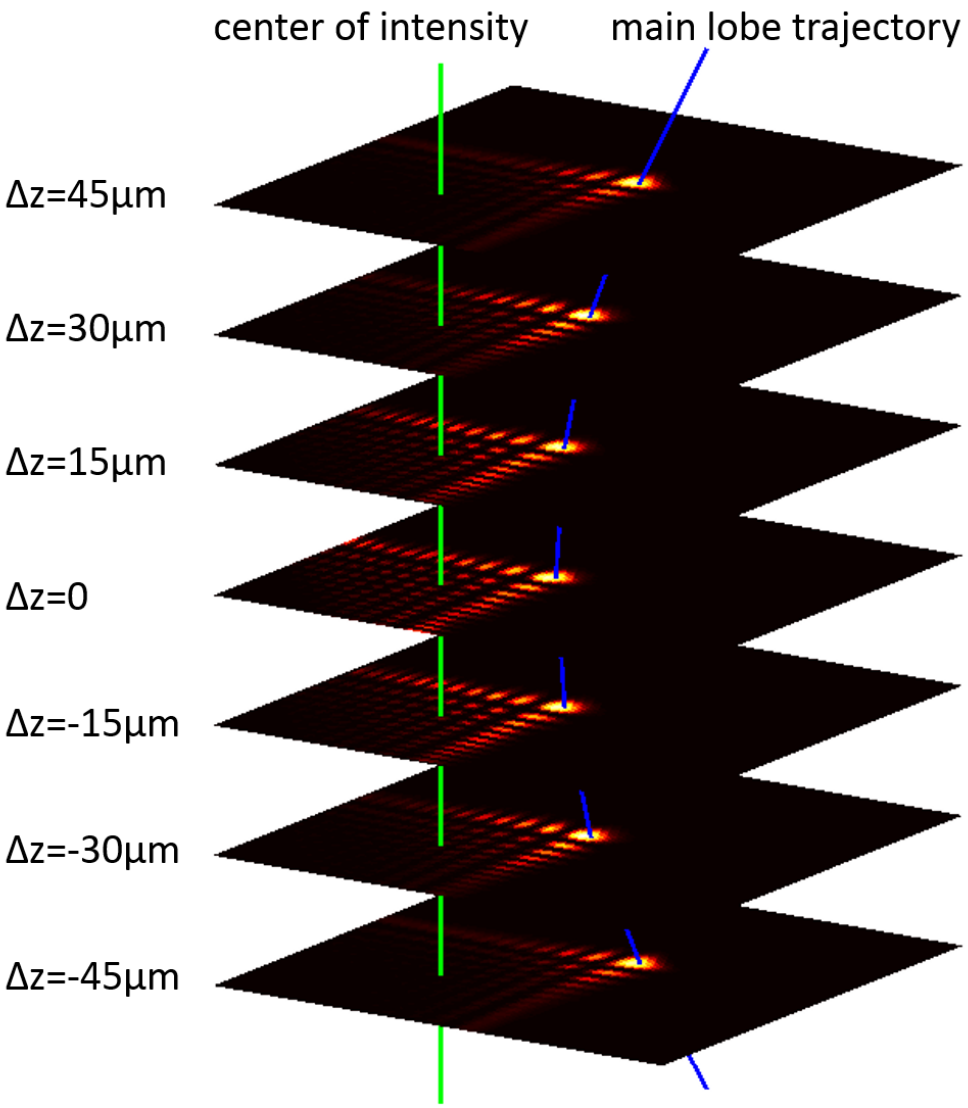

Fig. 2.19 Trajectory of the 'center of intensity' (green) of the AB-PSF compared to the trajectory of its main lobe (blue) over a depth range of 90 μm. The PSFs are generated with a $\alpha = 5\lambda$ cubic phase mask on a 20×, 0.4NA system.

emitters in 3D space with only one AB-PSF, without any additional imaging path or any modification of the AB-PSF. This is based on the fact that a single AB-PSF itself carries information in z, and this will be further discussed in section 3.6.2 where its CRLBs are calculated. In the following text, a method to extract this z information solely from a single intact AB-PSF will be proposed.

It is known that self-acceleration of the Airy beam does not violate the Ehrenfest's theorem as the 'center of gravity' of these beams moves at a constant velocity as a function of propagation distance[89]. Therefore, we expect the 'center of intensity' of the AB-PSF to be invariant even though the profile of the AB-PSF appears to be translating laterally. Consequently if we measure the disparity between the main lobe of the AB-PSF and its center of intensity, it should be a quadratic function to the emitter's z coordinate.

Fig. 2.19 shows a stack of simulated AB-PSFs with the main lobe indicated by the blue curve and the center of intensity indicated by the green. The center of intensity is simply calculated by $\sum x_k I_k / \sum I_k$. As can be observed, the center of intensity does not translate laterally which confirms that the average Poynting vector is parallel to the optical axis. In contrast, the main lobes translate along a parabolic trajectory as the z coordinates changes, which has been discussed in the previous chapters. Therefore, one can localize point emitters in 3D space using a single AB-PSF by measuring the disparity between the main lobe and its center of intensity.

Such an approach is much simpler compared to the Airy-CKM, however, it only works for very high SNR scenarios because the Poisson noise and background noise will alter the center of intensity of the AB-PSF, resulting in a degraded localization accuracy and precision. In addition, this approach has two more drawbacks: (1) the z-sensitivity of the AB-PSF is a linear function of z, it provides no z information near the focal plane. (2) the AB-PSF is symmetrical on two sides of the focal plane, which causes ambiguity and effectively loses half the depth range.

2.10 Conclusion

In this chapter, the lateral translation properties of the AB-PSF have been investigated and utilized to propose a new approach, the Airy-CKM technique, for 3D particle-localization microscopy. A bi-plane configuration is used to extract the absolute image translation and thus the xyz coordinates of the point sources.

Thanks to the diffraction-free propagation of the AB-PSF, this method provides significantly extended depth range compared to conventional methods. Moreover, the bi-plane configuration eliminates the sign ambiguity and reduced z sensitivity associated with the AB-PSF and the SB-PSF; thus, providing effectively double the depth range. Since the image deconvolution produces a compact PSF, a high seeding concentration is

more easily demonstrated than for the PSFs with spatially extended intensity profiles. A particular advantage is the simplicity of this configuration which not only enables it to be adapted to most microscopy systems but also provides a high-optical throughput which shows potential for low-photon-count experiments (further discussion in section 3.6.2).

A disadvantage, however, is that the two-channel configuration introduces difficulty in image registration and reduces robustness in practice. The use of a lateral beam splitter also halves the FOV achievable on a detector. An improved PSF and phase mask design that overcomes these disadvantages will be introduced in the following chapter.

Chapter 3

Twin-Airy PSF

The Airy-CKM technique discussed in the previous chapter provides greatly extended axial range compared to conventional imaging methods such as the astigmatism. However, it requires replication of the imaging path in order to determine the 3D position from the depth-dependent translation of the AB-PSF. This increases the complexity of both the optical setup and of the calibration procedure. Although a single AB-PSF can also be used to localize emitters in 3D space, it yields zero z sensitivity near the focal plane and is associated with a sign ambiguity. Therefore, a single channel approach which provides the benefits of the Airy-CKM technique is desirable. With such motivation, we seek a PSF design that contains two Airy-beam-like lobes, which will conserve the diffraction-free range and encode the depth information in a single PSF with constant z sensitivity and no ambiguity.

This chapter describes the design and validation of a 'twin-Airy' phase mask, which generates a PSF composed of two adjacent Airy-beam-like lobes (section 3.1). Following image deconvolution, such a PSF displays a double image of each point emitter with a mutual separation that varies with depth, enabling recovery of axial position over the extended depth range of Airy beams. This simplifies the optical configuration to a single imaging channel compared to the Airy-CKM technique. This twin-Airy PSF (TA-PSF) is also implemented using a refractive mask, which provides effectively 100% broadband optical throughput, is polarization insensitive, and provides very simple calibration and logistics. Moreover, the TA-PSF exhibits a quasi-uniform sensitivity to defocus over an extended range: it does not exhibit the reduced sensitivity of the Airy-beam PSF near the focus, nor the sign ambiguity highlighted by Jia et al.[17], and so provides more than double the effective range. The TA-PSF is characterized on a 60x, 1.4NA system by imaging quantum dots in order to assess the suitability of this PSF for single-molecule tracking and localization-based super-resolution applications. This result demonstrates a precision better than 30 nm over a 7 μm depth range.

3.1 Twin-Airy PSF and phase mask

To combine two Airy-beam-like lobes in one PSF, one possible solution is to concatenate two cubic phase directly at the pupil plane. However, the following two criteria should be considered when designing such a PSF: (1) discontinuity in the pupil phase profile is not preferred as it will introduce scattering, reducing the contrast and optical throughput. In addition, a discontinuous phase profile can not be displayed on deformable mirrors and increases the manufacturing difficulty of a phase mask. (2) As the light from an emitter is spatially coherent, the two Airy-beam-like lobes should be directed away from each other to avoid interference between them, which will alter the PSF profiles and consequently eliminate the inherent advantages of the Airy beams.

There are 16 possible ways of concatenations considering each Airy-beam-like lobe has four different orientations. Below shows four examples of direct concatenations of two cubic phase masks and the corresponding pupil functions. Here the pupil is divided into the upper and lower halves, x and y are pupil coordinates normalized to the pupil radius. The two cubic phase profiles on the two pupil halves are centered at $O_1\,(0,\,1/2)$ and $O_2\,(0,\,-1/2)$ respectively.

$$\begin{cases} -x^3+(y+1/2)^3 & y\le 0 \\ -x^3+(y-1/2)^3 & y>0 \end{cases}$$

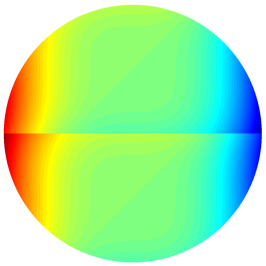

$$\begin{cases} x^3+(y+1/2)^3 & y\le 0 \\ -x^3+(y-1/2)^3 & y>0 \end{cases}$$

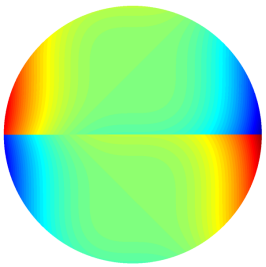

$$\begin{cases} x^3-(y+1/2)^3 & y\le 0 \\ x^3+(y-1/2)^3 & y>0 \end{cases}$$

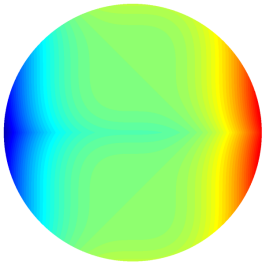

$$\begin{cases} -x^3+(y+1/2)^3 & y\le 0 \\ -x^3-(y-1/2)^3 & y>0 \end{cases}$$

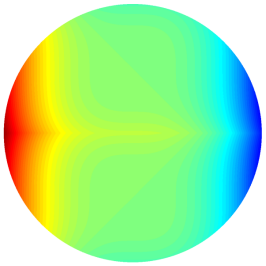

The first two designs are ruled out by criterion (1), because they both display discontinuity in the phase profile. The third one and the fourth one, which are cubic phases concatenated with their mirror images, are continuous functions across the pupil although they are not differentiable along $y=0$. However, such designs do not meet criterion (2) since the two halves of the pupil still direct light to the same region on the image plane (the center of the FOV if the emitter is on-axis), which will produce interference in the PSF. As can be observed in Fig. 3.1, the PSF generated by the fourth phase dose not contain two Airy-beam-like lobes as designed for. Instead, it yields depth-dependent interference patterns. Such a PSF with interference pattern can still be utilized for 3D localization using the phase-retrieval-based maximum-likelihood estimation (PR-MLE) proposed in ref[69], however, it does not preserve the extended axial range offered by the AB-PSF, nor the depth-invariant profile. Therefore, deconvolution can not be performed on such PSF images with a single pre-recorded deconvolution kernel.

Based on the above discussions, it can be concluded that the desired phase mask should also contain an opposite linear-phase term on each pupil half to direct the two resultant lobes away from each other, avoiding the interference between the two lobes. Therefore, the pupil function should have both cubic terms to generate the Airy-beam-like lobes and linear terms to avoid self-interference, and preferably displays a continuous profile. With this inspiration, the pupil function is designed as shown in Fig. 3.2a, with the following analytic expression:

$$\psi = \alpha(\cos(\frac{\pi\cdot y}{R_{pup}})+\frac{1}{2}\sin(\frac{\pi\cdot x}{R_{pup}})), \tag{3.1}$$

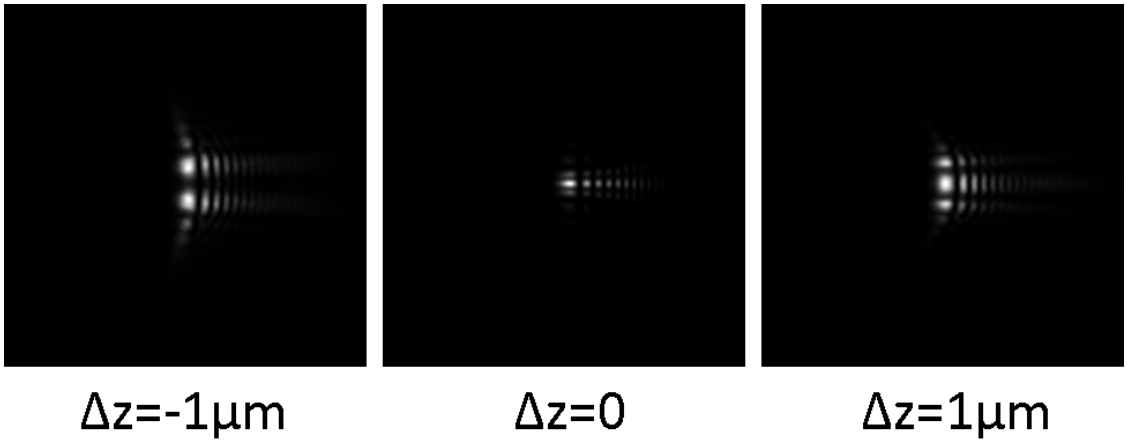

Fig. 3.1 Simulation of the interference in the PSF generated with the directly concatenated cubic phase masks (the last of the above mentioned examples) with peak modulation $\alpha = 3\lambda$.

where R_{pup} is the pupil radius and α is a parameter similar to that in the cubic phase and is related to the peak modulation. The factor of $\frac{1}{2}$ yields Airy-beam-like lobes with approximately equal dimensions in the x and y directions.

Such a phase design exhibits two quasi-cubic profiles centered at pupil locations O_1 and O_2. The Taylor expansion of ψ about O_1 and O_2 with the terms higher than cubic omitted can be written as:

$$\begin{aligned}\psi_{O_1} &\approx \alpha\left\{-\pi(\bar{y}-\frac{1}{2})+\frac{\pi^3}{6}(\bar{y}-\frac{1}{2})^3+\frac{1}{2}(\pi\bar{x}-\frac{\pi^3}{6}\bar{x}^3)\right\}\\ \psi_{O_2} &\approx \alpha\left\{\pi(\bar{y}+\frac{1}{2})-\frac{\pi^3}{6}(\bar{y}+\frac{1}{2})^3+\frac{1}{2}(\pi\bar{x}-\frac{\pi^3}{6}\bar{x}^3)\right\},\end{aligned} \tag{3.2}$$

where $\bar{x}$ and $\bar{y}$ are coordinates normalized to the pupil radius R_{pup}.

The cubic terms in the expressions for ψ_{O_1} and ψ_{O_2} contribute to the two Airy-beam-like lobes, which are mirror images of each other. The linear terms result in a constant offset in spatial separation between the two lobes. Each Airy-beam-like lobe exhibits a depth-dependent image translation, and so the disparity between the two main lobes is a function of the axial position as shown in Fig. 3.2b. The two lobes converge on one side of the focal plane but diverge on the other side. This eliminates the sign ambiguity associated with use of a single AB-PSF or the SB-PSF technique[17] and thus doubles the axial range. Compared to the use of diffractive phase functions, as are often used to implement other engineered phase functions, the use of a sinusoidal phase function can be readily implemented as a purely refractive mask offering the advantages of simple manufacture, low light scatter and broad spectral range.

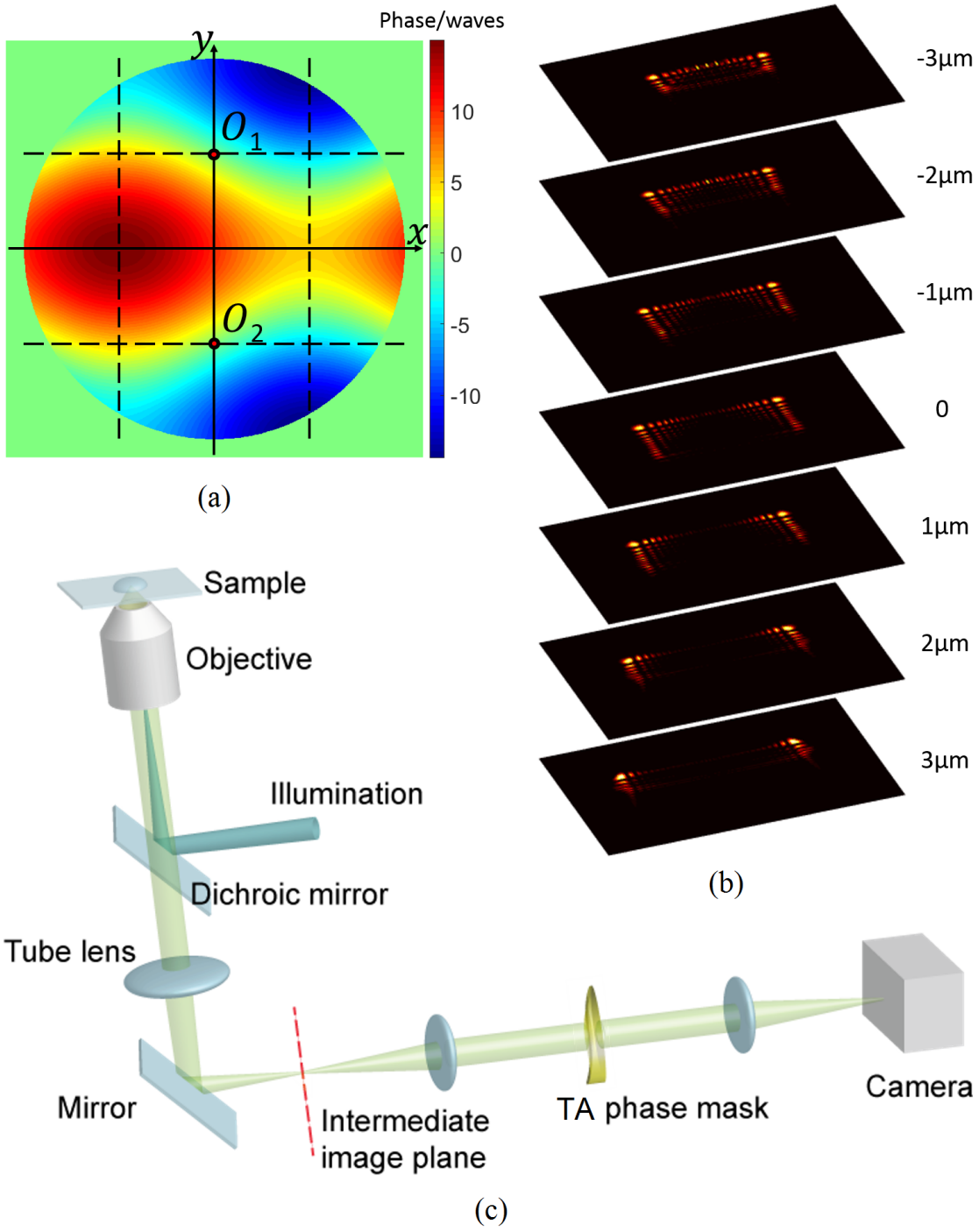

Fig. 3.2 (a)Pupil function of the TA-PSF. (b)Simulated variation in TA-PSFs with defocus with an $\alpha = 10\lambda$ phase mask on a 60x, 1.4NA system. (c)Schematic of the experimental setup, based on a Nikon Eclipse Ti microscope. The TA refractive mask is located at the re-image the pupil plane of a $4f$ relay system with 100 mm focal lengths.

3.2 Localization algorithms

This section focuses on the methods to deduce the emitter's *xyz* coordinates from the TA-PSF image. Two algorithms will be discussed including the PR-MLE and a novel deconvolution-based approach. It will also be shown that the deconvolution-based algorithm enables imaging of higher tracer density with overlapping PSFs.

3.2.1 Phase-retrieval-based maximum-likelihood estimation

An algorithm that can be used for estimation of the *xyz* coordinates in localization microscopy is the PR-MLE, which was proposed by Quirin et el. and used for both the DH-PSF and the tetrapod PSF[69, 73]. Given a calibration z-stack (i.e. a stack of images of a sub-resolution point source with preferably equal spacing: $I(z_i)$, $i = 1 : N_z$), the PR-MLE algorithm can also be utilized for the TA-PSFs. The steps of the algorithm are described below:

- Find an initial guess of the pupil function $P_0(k_x, k_y)$. A good initial guess is important for the rapid converging, however, it does not significantly alter the final result.
- Given the current pupil function $P(k_x, k_y)$, generate a stack of simulated amplitude PSFs, i.e. $APSF(x, y, z_i)$ the complex field in the image space, using the simulation model described in section 1.4. Ideally, the amount of defocus for each computer generated amplitude PSF should have the same absolute value as its corresponding experimentally measured PSF. However, this can be compensated in the retrieved pupil function as a global defocus phase, which makes it less critical. In contrast, the z spacing in the simulated amplitude PSF stack should be exactly the same as that in the measured PSFs.
- Replace the amplitude of each computer-generated amplitude PSF with the square root of its corresponding measured calibration PSF:

  $APSF(x, y, z_i) = \sqrt{I(z_i)}\mathrm{e}^{\mathrm{i}Arg(APSF(x,y,z_i))}$.
- Inverse Fourier transform to get the current pupil function for each amplitude PSF in the z stack by dividing the corresponding defocus phase term.

  $P_i(k_x, k_y) = \mathscr{F}\{APSF(x, y, z_i)\}/\mathrm{e}^{\mathrm{i}k_z z_i}$.
- Average the pupil functions to get the current pupil function $P(k_x, k_y) = \sum P_i/N_z$. It's worth noting that the current pupil function can be constrained to phase only as the phase mask used here provides almost 100% transmission and only modulates the phase of the light.

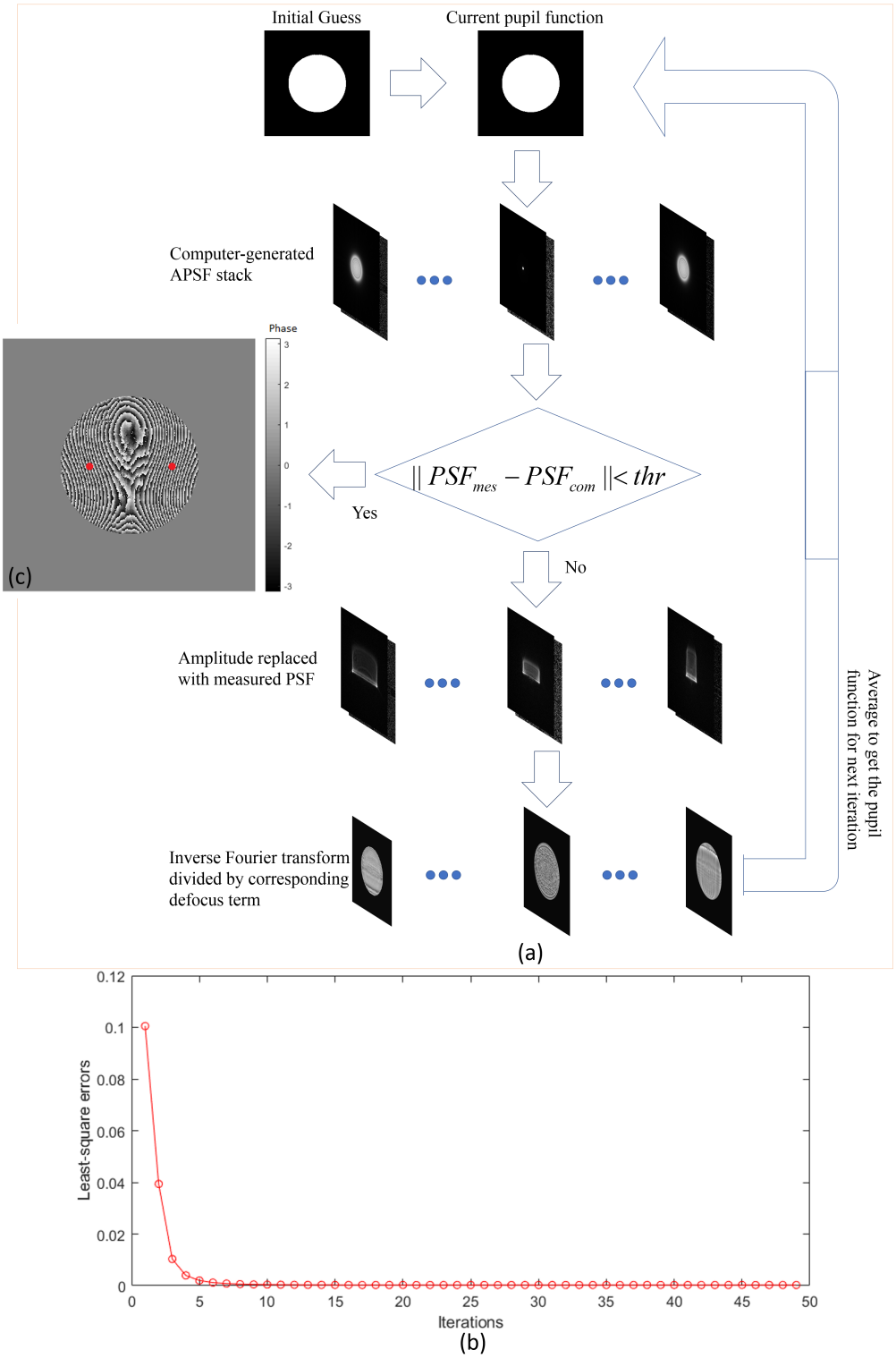

Fig. 3.3 (a) Phase retrieval procedures. (b) Decreasing least-square error between the computer-generated PSF and the experimentally measured PSF as iteration runs. (c) A retrieved twin-Airy phase profile (wrapped) after 500 iterations.

- Repeat the iteration until the error between the computer-generated PSF and the experimentally measured PSF is below a threshold.

An intuitive flow chart of the above discussed phase retrieval algorithm is illustrated in Fig. 3.3a. Note that the above phase retrieval algorithm is sensitive to shot noise in the measured calibration stack. Ideally long exposure time should be used or a number of repeated images should be acquired at the same z and average to minimize the shot noise. Fig. 3.3b shows an example of this phase retrieval process with the initial guess of the pupil function being a clear aperture. As the number of iteration increases, the residuals between the computer-generated PSF and the experimentally measured PSF decrease. The resultant phase mask is shown in Fig. 3.3c. Although the retrieved phase here is wrapped phase, it can be observed that it exhibits a twin-Airy phase profile and two origins of the quasi-cubic phases as indicated with red dots.

With the retrieved pupil function, the image of an point emitter at arbitrary xyz can be generated by computer, that is equivalently a continuous image formation model. This allows the use of the maximum-likelihood estimation to deduce the 3D coordinates. Under the Poisson noise model where only the shot noise in the image is considered, the set of parameters to be estimated in a measured PSF is (x,y,z,N_{ph},N_b) with xyz being the spatial coordinates and N_{ph} being the total number of photons in a single PSF and N_b being the number of background photons per pixel. These parameters can be determined by maximizing the likelihood function, or in practice minimizing the negative log-likelihood function[90, 73]:

$$LL = \sum_k \mu(k) - s(k) ln[\mu(k)] + C, \tag{3.3}$$

where $s(k)$ is the detected number of photons on the k-th pixel, $\mu(k)$ is the expected number of photons calculated with the set of parameters (x,y,z,N_{ph},N_b).

Note that the minimization process of the likelihood function is computationally intense, especially if the PSF shape is self-similar and induces many local minima in the optimization process. In addition, the likelihood function will inevitably be altered in the case of overlapping PSFs, which degrades the localization precision.

3.2.2 Deconvolution-based algorithm

Similar to the single AB-PSF, image deconvolution can be efficiently applied to the TA-PSF, meaning a fast deconvolution-based algorithm can be used to perform the 3D localization as summarized in Fig. 3.4. First, the recorded image is deconvolved with the in-focus TA-PSF. The deconvolved PSF consists of two compact lobes as shown in Fig. 3.7b, approximating the in-focus diffraction-limited PSF (DL-PSF). Then the separation of the two deconvolved lobes in y (i.e. the two-lobe disparity TLD) is deduced after two

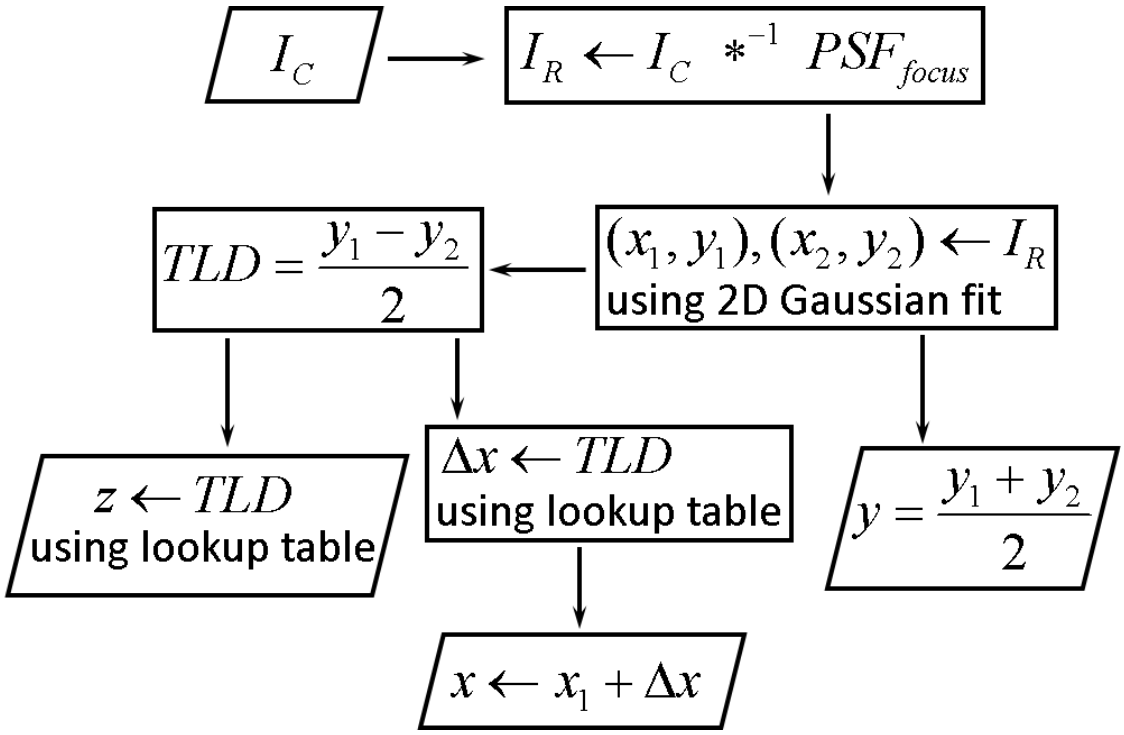

Fig. 3.4 Deconvolution-based 3D localization algorithm for the TA-PSF. $*^{-1}$ refers to deconvolution of the TA-PSF, which is detailed in Fig. 3.5. I_C is the captured image of an emitter to be localized, TLD refers to the two-lobe disparity, i.e. the disparity between the two recovered lobes of the TA-PSF.

deconvolved lobes are fit to Gaussian profiles. The TLD increases with defocus (Fig. 3.7c) while the mean positions of the two deconvolved lobes translate in x parabolically (Fig. 3.7d), which follows exactly the same lateral translation of the two main lobes of the TA-PSF. With TLD and the x-directional lateral translation calibrated, one can localize an emitter directly from the TLD.

The deconvolution here is different from the deconvolution of an AB-PSF as the TA-PSF contains two Airy-beam-like lobes. A detailed image deconvolution procedure for the TA-PSF is highlighted in Fig. 3.5. The two halves of the in-focus PSF, $PSF(z_0)$, are used as the deconvolution kernels. Given an input image I_C, it is firstly deconvolved using both deconvolution kernels. The result using the upper kernel yields a compact high-intensity upper lobe while the result using the lower kernel yields a compact high-intensity lower lobe. A threshold is set to filter out the high-intensity lobes from the low-intensity lobes that are deconvolved from a non-matched kernel. The filtered results are then used to form a final recovered image with two compact bright lobes. The compactness of the deconvolved PSF is a desirable property over other spatially expanding PSFs as it allows high emitter density with overlapping PSFs to be imaged.

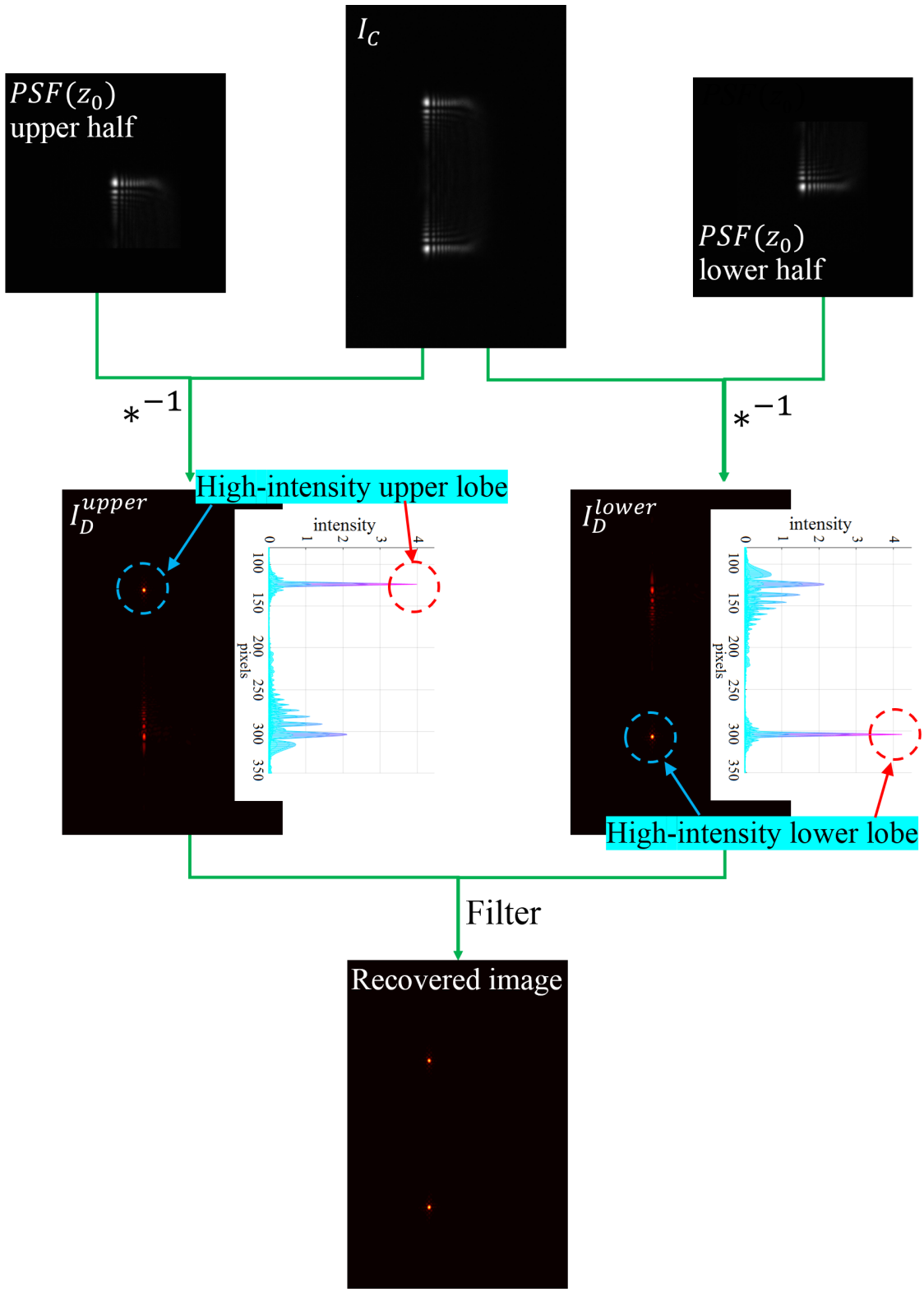

Fig. 3.5 Deconvolution procedures for the TA-PSF. $*^{-1}$ refers to Wiener deconvolution. $PSF(z_0)$ is the in-focus PSF from the pre-recorded calibration PSF stack. I_C refers to an input captured image. I_D^{upper} and I_D^{lower} are the intermediate deconvolved images.

3.2.3 Overlapping PSFs

For high-tracer-density scenario with overlapping PSFs, additional processing is needed to correctly pair the recovered upper lobe and the lower lobe of each TA-PSF. This is achieved based on the following four criteria:

1. The intensity of the deconvolved upper lobe is similar to that of the deconvolved lower lobe. This assumes the twin-Airy phase mask is well aligned with respect to the optical axis, a misalignment may break the symmetry in the two lobes, which will be discussed in section 3.5.
2. As discussed in section 2.3, the deconvolved PSF displays an elliptical profile when the defocus of the deconvolution kernel is mismatched to the defocus of the acquired PSF. When this occurs, the ellipticity of the deconvolved upper lobe is similar to that of the lower lobe.
3. The two deconvolved lobes are well aligned in a specific direction (in this case, they are aligned in the y direction.
4. The separation of the two deconvolved lobes, i.e. the TLD, is within the calibrated range.

Fig. 3.6 shows an example of deconvolution and two-lobe pairing for several overlapping TA-PSFs. The sample was a drop of water solution containing fluorescent beads between two cover slips. As can be observed, image deconvolution produces very compact lobes (Fig. 3.6b), avoiding the overlap of PSFs that occurs in the raw image (Fig. 3.6a). The upper and the lower lobes of each particle can be paired using the above mentioned criteria. In this case, all the overlapping PSFs in the FOV can be uniquely identified with the upper and lower lobes paired correctly; thus, the xyz coordinates can be deduced from the two-lobe disparities. The locations of point pairs P7, P8 and P1,P2 in Fig. 3.6c are examples of potentially challenging identifications. P7 and P8 are two beads located very close to each other, such that their PSFs overlap severely in Fig. 3.6a while P1 and P2 have similar, but not identical, x coordinates. In both cases, the two lobes can be correctly paired based solely on criterion (3). P10 and P11 were at different focal planes compared to the others, so they yield different two-lobe disparities in Fig. 3.6c and appear defocused in Fig. 3.6d because the imaging system was focused at the upper side of the lower coverslip where P1-P9 resided on. A comparison of the localization result in xy (red dots) with the ground truth is illustrated in Fig. 3.6d, which proves that the above mentioned criteria can pair the two PSF halves effectively even though the PSFs are overlapping.

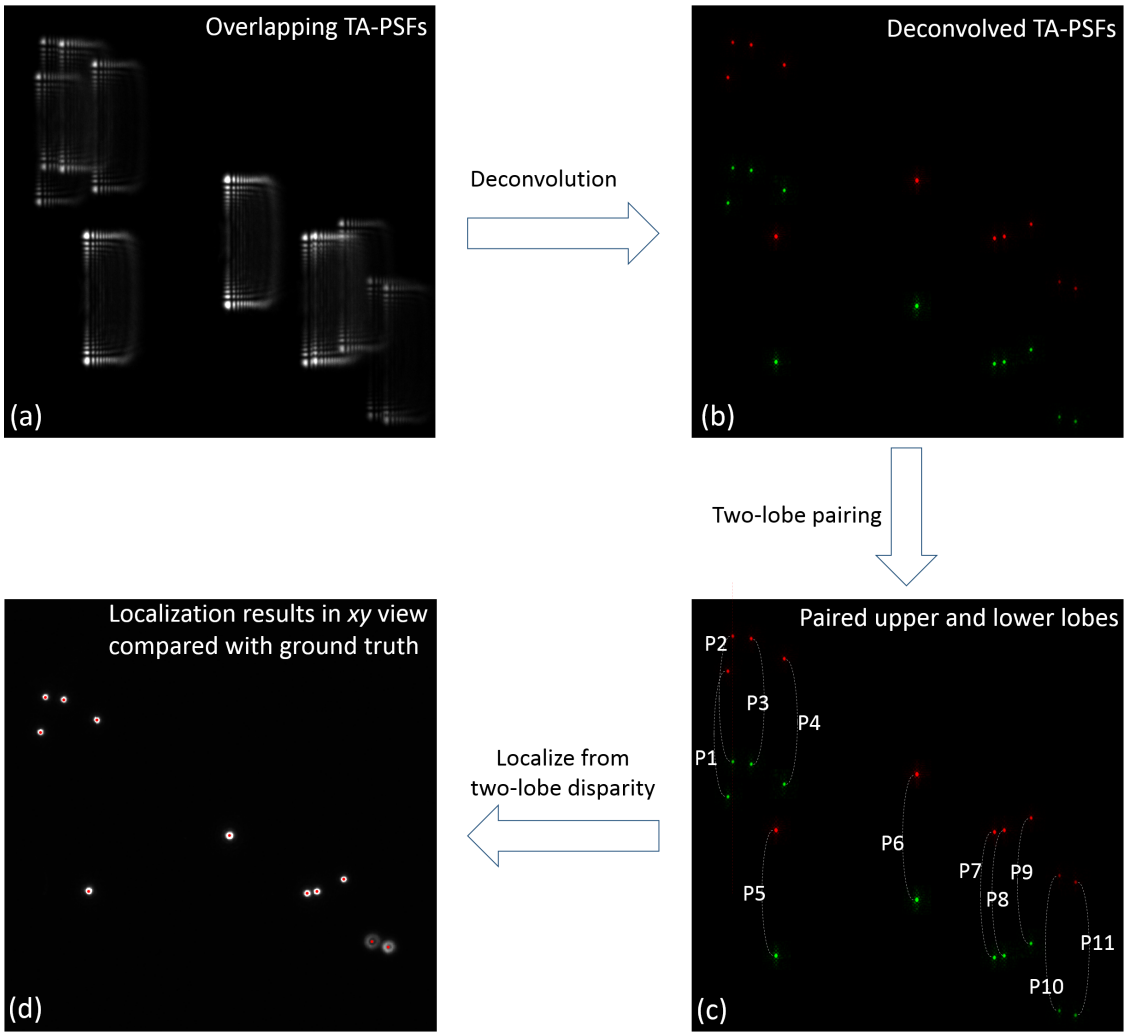

Fig. 3.6 (a) Example of overlapping TA-PSFs. (b) Deconvolved PSFs with red indicating the upper lobes and green indicating the lower lobes. (c) Two-lobe pairing result. P1: particle 1 (or two-lobe pair 1). (d) Localization results (red dots) in *xy* view compared with the ground truth. The images were recorded with fluorescent bead solution between two cover slips, and the ground truth was acquired with the phase mask removed.

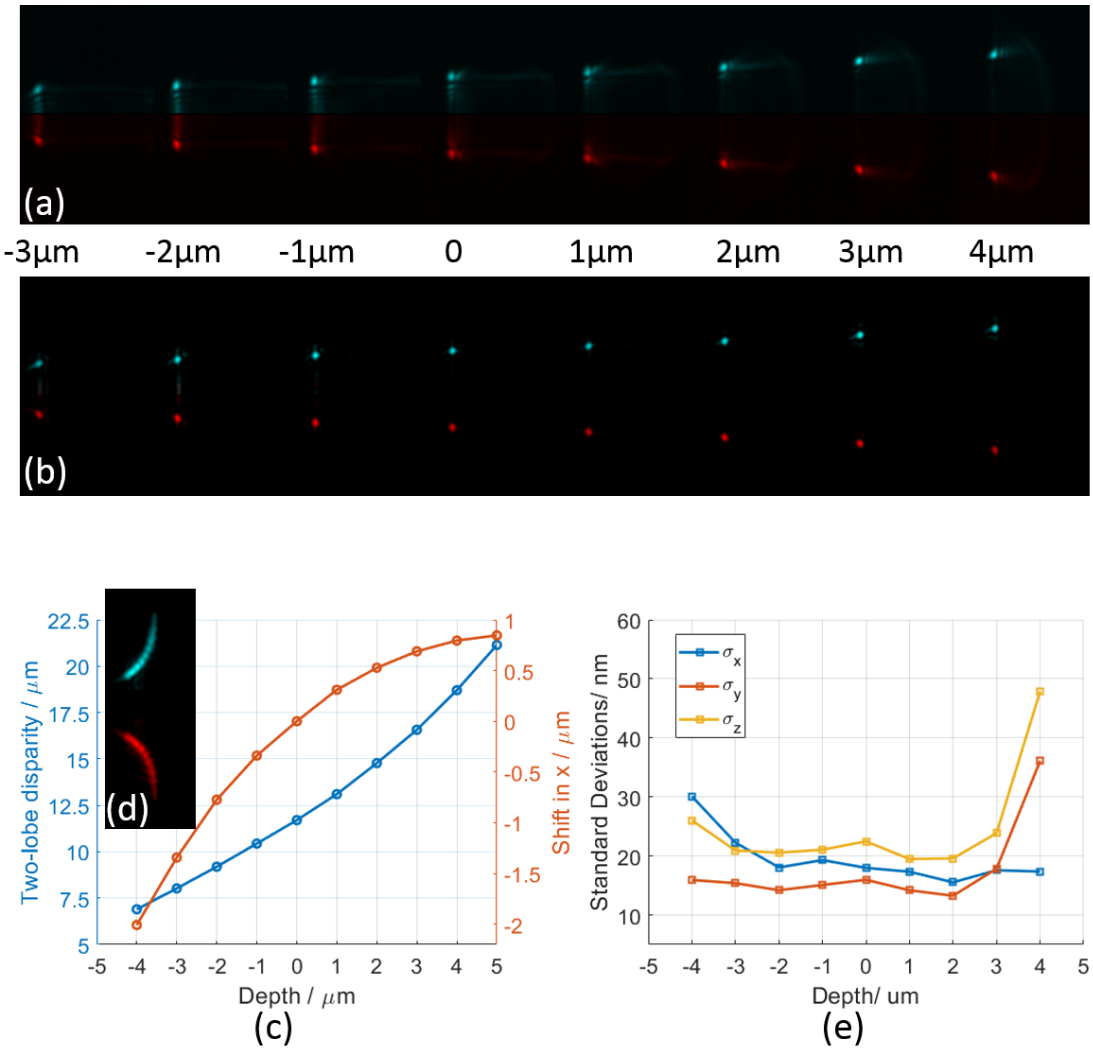

Fig. 3.7 (a)Point-spread functions over a depth range of 10 µm, acquired with 60x, 1.4NA , averaged over 1000 frames. (b)Corresponding recovered PSFs, with recovery kernel being the in-focus PSF. (c) Calibration curves: blue curve maps depth to disparity between the two recovered lobes and orange curve maps depth to lateral shift. (d) Superimposition of the recovered PSFs in (b). (e) Experimental measurements of statistical localization precision. The standard deviations σ_x, σ_y and σ_z for each z position are calculated with 1000 camera frames of the same quantum dot.

3.3 Demonstration for single-molecule experiments

In this section, the TA-PSF is demonstrated for 3D single-molecule localization microscopy with a 60x, 1.4NA oil-immersion microscope using subwavelength-sized quantum dots (Trilite Fluorescent Nanocrystals emitting at 665 nm). The localization precision of the TA-PSF is also assessed in the low-photon-level scenario.

The optical configuration is shown in Fig. 3.2c, where a $4f$ relay system was used to access the pupil plane of the imaging system. The twin-Airy phase mask was custom fabricated to produce a peak phase modulation of $\alpha = 10\lambda$ for an aperture diameter of 6 mm. To approximate single molecules, the exposure time was set to limit the detected photon flux level and about 6800 photons were detected per localization with a background of about 9 photons per pixel. The images were captured using an EMCCD sensor (Andor iXon 888) with 13 µm pixel size. The recorded TA-PSF is shown in Fig. 3.7a with the upper half and the lower half indicated in cyan and red respectively. As can be observed, it maintains approximately its twin-Airy intensity profile over 7 µm range while the two halves of the complete PSF increase in separation. Fig. 3.7b shows the corresponding deconvolved TA-PSFs with the compact two-lobe profiles. A superimposition of all the deconvolved PSFs recorded within this depth range is displayed in Fig. 3.7d where the parabolic translation of each lobe can clearly be observed. Both the two-lobe disparity and the x-directional lateral translation are quadratic functions of the axial position of the emitter (Fig. 3.7c) which can be used as lookup tables for the localization algorithm discussed in section 3.2.2.

Fig. 3.7e shows the localization precision in x, y and z over an axial range of 10 µm. As can be observed, a precision better than 30 nm (as given by the standard deviation of 1000 measurements) in all spatial dimensions was achieved over a depth range in excess of 7 µm, which is comparable to the dimension of many cells. This also indicates that this technique has potential for single-molecule tracking and localization-based super resolution over an extended depth range.

3.4 Pupil-size mismatching

Pupil size varies with the NA; thus if a different objective with a different NA is used, the pupil size often changes as a result. This may lead to mismatching between the actual pupil size of the imaging system and the size of the designed phase mask, especially when laser-fabricated phase masks are used. Therefore, it is worth investigating the influence of pupil-size mismatching on the resultant PSFs. For the cubic phase mask, when its size is mismatched to the actual pupil size, it is still effectively a cubic phase, but with a

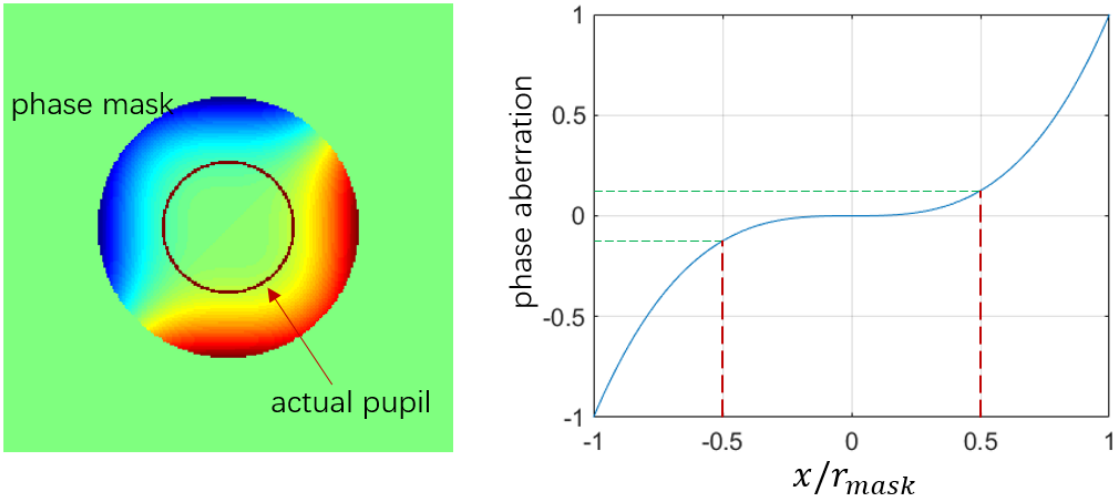

Fig. 3.8 A mismatched pupil phase is still a cubic phase, but with a different strength. Dark red indicates the actual pupil size.

stronger or weaker modulation. The effective peak modulation can be estimated using the following equation,

$$\psi_a = \frac{r_a^3}{r_d^3}\psi_d, \tag{3.4}$$

where the r_a and ψ_a are the actual pupil size and the actual wavefront modulation at the pupil edge while r_d and ψ_d are the designed size of the phase mask and designed wavefront modulation.

An intuitive illustration of such effects can be observed in Fig. 3.8, a pupil size that is half of the designed cubic phase mask gives a $1/8$ weaker modulation. In the case that the pupil size is bigger than the designed phase mask, the pupil will be cropped by the phase mask, which will effectively lower the NA and optical throughput for the imaging system. This reduced NA yields a larger depth range however, at the cost of additional photon loss. Therefore pupil cropping are non-preferred for low-photon-count scenario such as single-molecule experiments.

However, in the case of a twin-Airy phase mask, a mismatched pupil size will not generate the exact 'TA-PSF'. This is because the coordinate origins of the two cubic phases (O_1 and O_2) are off-axis, a cropped phase profile can no longer be described by the equation 3.1. Therefore, it is important to match the size of the phase mask to the actual pupil size of the microscope when using the twin-Airy phase mask. The same is true for most previously discussed phase masks such as the double-helix phase mask and the tetrapod phase mask.

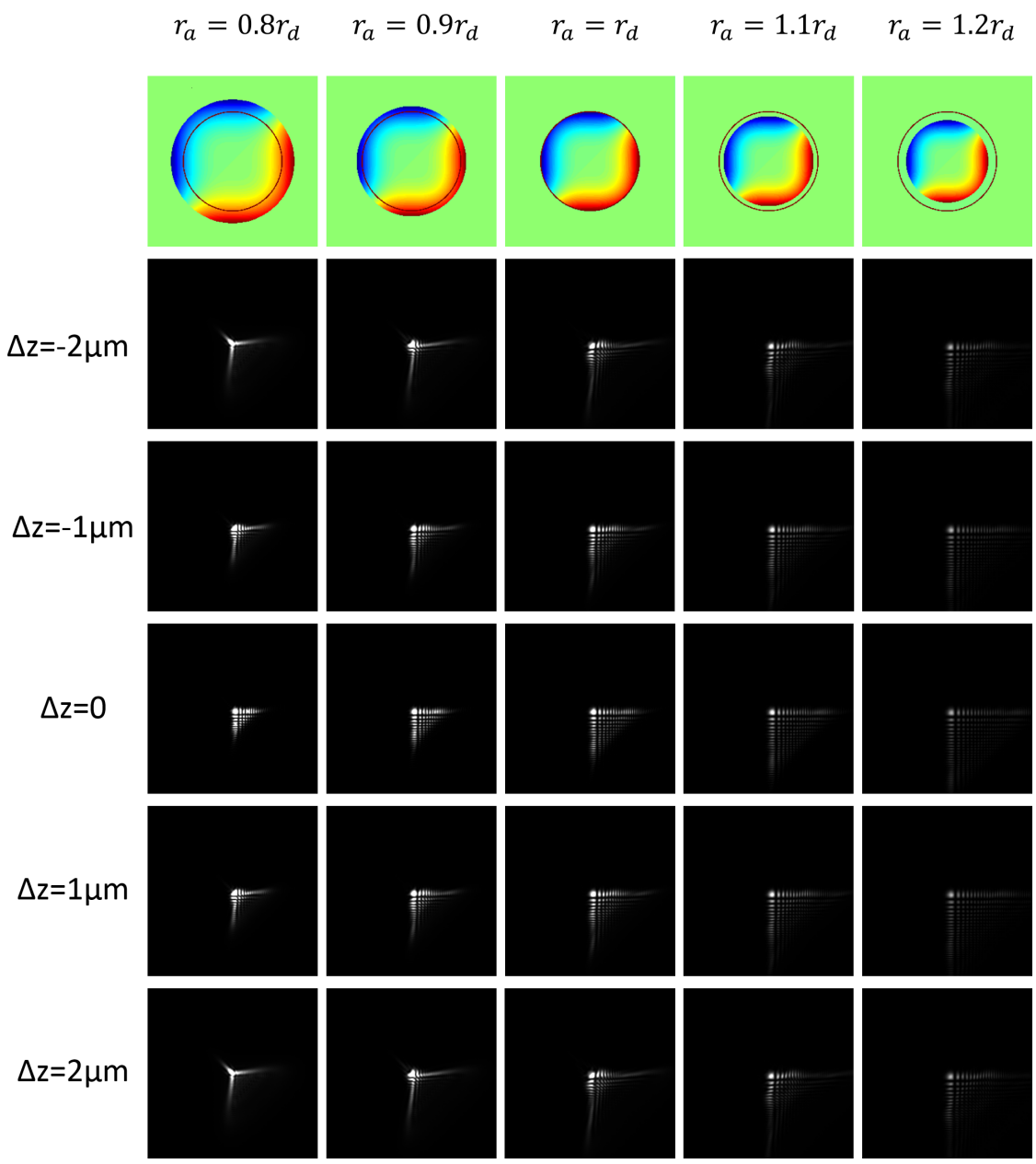

Fig. 3.9 Influence of pupil-mismatching on the AB-PSF profile. The circle in dark red shows the actual pupil size. Simulation based on a 1.45NA, 100× system with an $\alpha = 5\lambda$ cubic phase mask. r_d: designed radius of the phase mask. r_a: actual pupil size of the microscope.

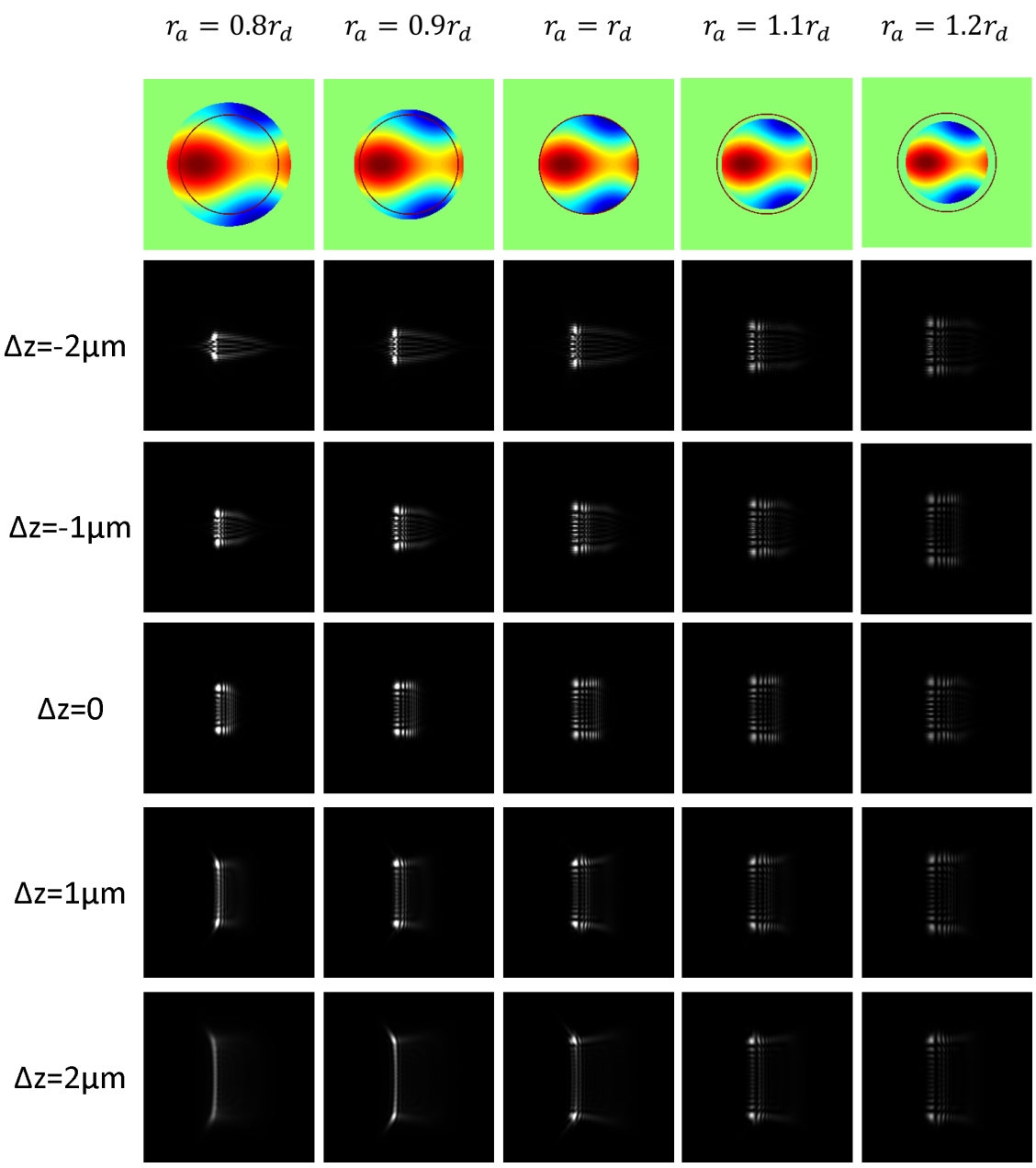

Fig. 3.10 Influence of pupil-size mismatching on the TA-PSF profile. The circle in dark red shows the actual pupil size. Simulation based on a 1.45NA, 100× system with an $\alpha = 2.5\lambda$ twin-Airy phase mask. r_d: designed radius of the phase mask. r_a: actual pupil size of the microscope.

Experimentally, the pupil size of the microscope can be adjusted by changing the focal length of the relay system. A relay lens with a focal length larger than the tube lens magnifies the pupil while a relay with shorter focal length demagnifies the pupil. However, the commercially available focal lengths for optical lenses limit the ability of continuous adjustment and thus the perfect matching of the pupil size. Therefore, it is important to explore the influence of pupil mismatching on the PSF profile.

To this end, an imaging system with mismatched pupil sizes is simulated. A 1.45NA, 100× system is assumed, with the designed sizes of the phase mask ranging from 0.8 to 1.2 times the actual pupil size. The pupil-cropping effect is also considered here where the physical size of the phase mask is smaller than the actual pupil size. PSFs at various focal planes are generated, from which we can observe the influence of pupil mismatching. The results for the cubic phase masks with various sizes and their corresponding AB-PSFs are illustrated in Fig. 3.9. As expected, a cubic phase mask bigger than the actual pupil size produces a smaller AB-PSF due to the weaker modulation, this also means a higher signal level and a smaller depth range. On the contrary, a cubic phase mask that is smaller than the actual pupil size gives a bigger AB-PSF profile with a larger depth range due to the effectively lower NA. However, the SNR is lower because of both the bigger intensity profile and photon rejection from the cropped pupil.

For the twin-Airy phase mask that is designed to be bigger than the actual pupil size, the effective phase profile does not generate the exact 'TA-PSF'. Nevertheless, when the amount of mismatch is small, the PSFs still exhibit a TA-PSF profile approximately with a smaller depth range as shown in Fig. 3.10, similar to that generated by a weaker twin-Airy phase mask. However, simulations show that a twin-Airy mask that is significantly bigger than the actual pupil size can not generate the twin-Airy PSF profile as the side lobes tend to 'bend' towards the middle of PSF (as can be observed from the first column of Fig. 3.10 when $r_a = 0.8r_d$). On the other hand, a twin-Airy phase mask that is designed to be smaller than the actual pupil size still generates the exact TA-PSF with a effectively lower NA due to the pupil cropping. As can be seen from the fourth and fifth columns of Fig. 3.10, the depth range becomes lager but the signal level is much lower. This is again due to the effectively lower NA and additional photon rejection from the cropped pupil.

3.5 Phase mask misalignment

In addition to the matching of the pupil size, the alignment of the phase mask is also crucial to generate the desired PSF. Misalignment in all directions results in variations in the PSF profile and thus may influence the designed performance. This is true for all types of phase masks that have been considered in this thesis.

The influence of misalignment for the cubic phase mask has been investigated previously in literature[83]. A misalignment of the phase mask in the z direction does not alter the profile of the AB-PSF significantly, meaning that the AB-PSF profile is not sensitive to z displacement of the phase mask. This is due to the slow varying beam diameter near the pupil plane. Nevertheless, a z displacement of the phase mask will inevitably introduce a field dependence in the PSF, exhibiting asymmetry when the point emitter is off-axis. Fig. 3.11 shows the AB-PSFs generated with the phase mask decentered in xy directions. Compared to the well centered results in the first column, decentering of the cubic phase mask in x and y breaks the symmetry in the PSF. When the system has a positive (negative) defocus, the AB-PSF yields one 'leg' longer (shorter) than the other. An opposite decentering of the cubic phase mask together with an opposite defocus results in effectively the same AB-PSF profile.

The influence of the twin-Airy phase mask misalignment on the TA-PSF profile is also investigated. As shown in Fig. 3.12, the first column shows the well-aligned twin-Airy phase mask and the corresponding PSFs; the following four columns are the results for the misaligned phase masks in x and y directions, where a displacement of 20% of the pupil radius is considered. A displacement in the y direction breaks the symmetry in the PSF, causing the upper half to be weaker or stronger than the lower half. And the weaker half no longer preserves the Airy-beam profile at large defocus. The reason for this phenomenon is the y directional displacement makes the semi-cubic phase profile centered at O_1 or O_2 in Fig. 3.2a incomplete. A further displacement will completely remove one half of the TA-PSF, resulting in a single AB-PSF. Since the data processing requires the two lobes to be symmetrical (section 3.2.3), in this work the twin-Airy mask is always pre-aligned before taking calibration and data. A displacement of the twin-Airy phase mask in the x direction, however, does not significantly change the profile of the TA-PSF near the focal plane. The obtained PSF has some noticeable variations at large defocus, resulting in a increased useful depth range on one side of the nominal focal plane and a reduced useful range on the other side. The most significant influence of phase mask misalignment, however, lies in the reduced photon efficiency due to additional photon loss at the edges of the pupil. If the phase mask is not larger than the actual pupil size, a misalignment directly reduces the SNR and should be avoided in experiments.

The above discussion reveals the influence of the phase mask misalignment on both the AB-PSF and the TA-PSF, and can be used as guidelines for optical alignments in practice. In this work, the fabricated phase masks are fitted in 3D printed holders first and then implemented into the optical system. For the modified objective as discussed in chapter 2, the holder tightly aligns the phase mask with other objective elements allowing no freedom of movement. The recorded image in Fig. 2.10 proves that the phase mask was well aligned with the optical axis. However, there is no flexibility in this case if the phase mask is not aligned. In the case of $4f$ relay implementation as used in this chapter and the following chapter, the 3D phase mask holder is firstly mounted on a rotation

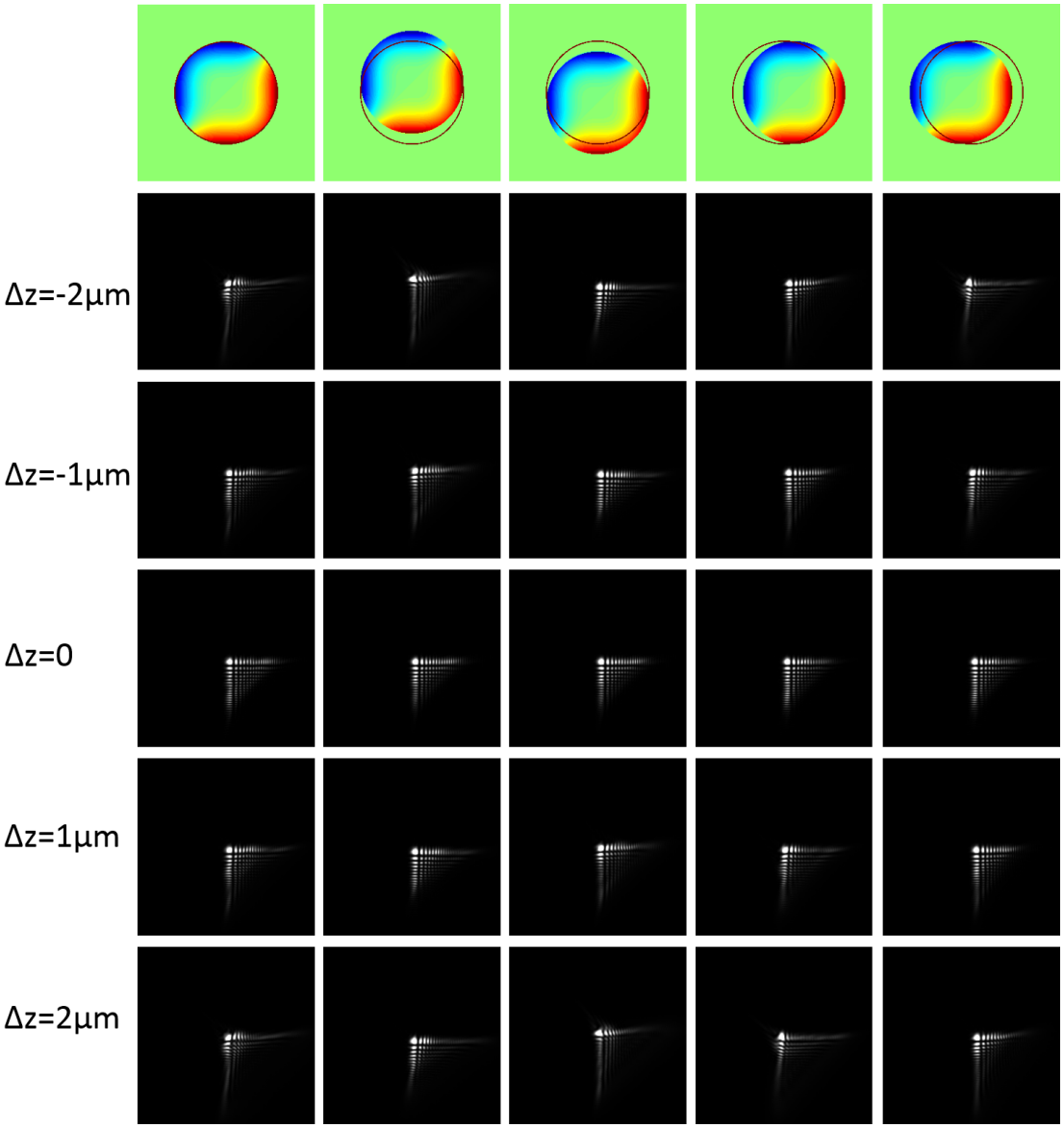

Fig. 3.11 Influence of phase mask decentering on the AB-PSF profile. The circle in dark red shows the actual pupil. Simulation based on a 1.45NA, 100× system with an $\alpha = 5\lambda$ cubic phase mask. r_d: designed radius of the phase mask. r_a: actual pupil size of the microscope.

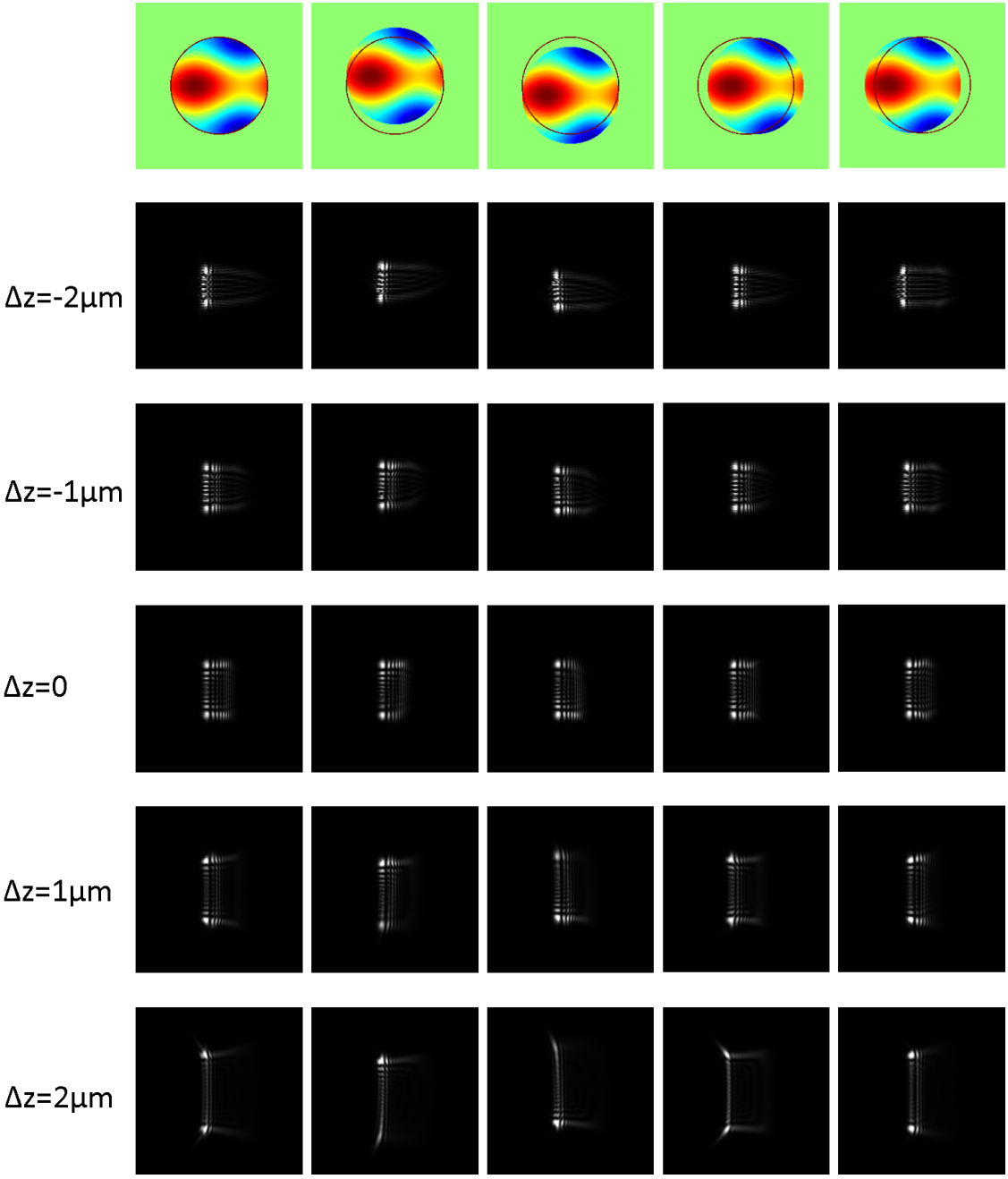

Fig. 3.12 Influence of phase mask decentering on the TA-PSF profile. The circle in dark red shows the actual pupil. Simulation based on a 1.45NA, 100× system with an $\alpha = 2.5\lambda$ twin-Airy phase mask. r_d: designed radius of the phase mask. r_a: actual pupil size of the microscope.

mount (Thorlabs Threaded Rotation Mount, LRM1) and then mounted on a *xy* translator (Thorlabs 30 mm Cage XY Translator, CXY1) which can slide in the direction of the optical axis. In this way, the phase mask can be translated in all three dimensions and rotated about the optical axis at the same time. The reimaged pupil can be visualized by imaging of diffusing objects (e.g. a white tape attached to the surface of a coverglass) in bright field, the high-contrast bright spot at the middle of the $4f$ relay is an approximation of the location and size of the pupil given paraxial scenario. Therefore, the *xyz* position of the phase mask should be adjusted with respect to the high-contrast bright spot while the rotation of the phase mask can be adjusted with the detected PSF on the camera. Note that the tilt of the axis of the phase mask with respect to the optical axis of the imaging system is negligible with the 3D printed holder tightened in the rotation mount.

3.6 Cramer-Rao lower bound analysis

In this chapter and the previous chapter, the twin-Airy and the Airy-CKM techniques have been reported respectively for 3D particle-localization microscopy. In this section, the performance of both techniques will be assessed in terms of localization precision and axial range, and comparisons will be made to several existing techniques mentioned in the literature review.

A significant part of point-localization microscopy lies in its data processing, i.e. to estimate the 3D coordinates of the point emitters from the recorded 2D image. Various localization approaches (estimators) have been used in this field including the mostly used the least-square fitting and maximum-likelihood estimation, thus the following challenges arise when different techniques are compared: (1) different techniques usually employ different estimators. For example in the astigmatism technique, ellipticity is calculated to estimate the 3D location; in rotation-based and translation-based techniques, least-square Gaussian fit can be applied to the PSF lobes to calculate rotation angles and disparities enabling the 3D localization; while some techniques can only use MLE to estimate the 3D locations. (2) For the same technique, different estimators always give different localization precision. For example, MLE is proved to have better precision than least square fitting under low background levels[90]. Therefore, to assess and compare the techniques in particle-localization microscopy, a metric that is independent of the specific localization estimators is desirable.

3.6.1 Basics of CRLB in microscopy

Ober et al. treated estimating emitters' 3D locations as a parameter estimation problem and developed a framework based on the information theory to calculate the Cramer-Rao

lower bound (CRLB) for a specific PSF[70]. The Cramer-Rao inequality gives a lower bound on the variance of any unbiased estimators of a deterministic parameter, which is the inverse of the Fisher information. Thus, if the spatial coordinates x, y, z are parameters to be estimated, the square root of this lower bound yields the best achievable standard deviation (i.e. the localization precision) regardless of any unbiased estimator used. In this way, different techniques can be compared directly. The PSF that gives more localization precision carries more information of those parameters.

For a N-pixel image, the Fisher information can be written as the sum of the Fisher information matrices corresponding to the data in the N pixels[70]:

$$I(\boldsymbol{\theta}) = \sum_{k=1}^{N} E\left[\left(\frac{\partial \ln f_{\boldsymbol{\theta},k}(c)}{\partial \boldsymbol{\theta}}\right)^{T}\left(\frac{\partial \ln f_{\boldsymbol{\theta},k}(c)}{\partial \boldsymbol{\theta}}\right)\right], \tag{3.5}$$

where E is the expectation, $\boldsymbol{\theta} = [x, y, z]$ denotes the spatial coordinates and $f_{\boldsymbol{\theta},k}(c)$ is the probability distribution for the k-th pixel with c being the photon count. The probability distribution depends on the data model for the PSF and the specific PSF intensity distribution. Various data models can be used to characterize imaging systems mathematically, what is employed here is the so called 'Poisson model' where the pixelation of the finite detector, the shot noise from the object of interest and the shot noise from the background fluorescence are taken into account[70]. This data model assumes that the detector does not introduce any noise during the read-out process, however, it is considered as a reasonable data model and widely used in CRLB simulations since the read-out noise is typically small compared to the number of photons detected on each pixel. Under this data model, the probability mass function associated with the k-th pixel can be written as:

$$f_{\boldsymbol{\theta},k}(c) = \frac{v_{\boldsymbol{\theta},k}^{c} \mathrm{e}^{-v_{\boldsymbol{\theta},k}}}{c!}, \tag{3.6}$$

where $v_{\boldsymbol{\theta},k} = \mu_{\boldsymbol{\theta},k} + \beta_{\boldsymbol{\theta},k}$ is the expected photon count of the k-th pixel. $\mu_{\boldsymbol{\theta},k}$ is the expected count of the signal photons and $\mu_{\boldsymbol{\theta},k}$ is the expected count of background photons.

Substituting probability mass function to equation 3.5 and evaluating the expectation terms give the following Fisher information matrix:

$$I(\boldsymbol{\theta}) = \sum_{k=1}^{N} \frac{1}{\mu_{\boldsymbol{\theta},k} + \beta_{\boldsymbol{\theta},k}}\left(\frac{\partial \ln \mu_{\boldsymbol{\theta},k}}{\partial \boldsymbol{\theta}}\right)^{T}\left(\frac{\partial \ln \mu_{\boldsymbol{\theta},k}}{\partial \boldsymbol{\theta}}\right). \tag{3.7}$$

The expected signal photons can be derived from a specific PSF model. Therefore, the Fisher information matrix can be calculated using equation 3.7. The Cramer-Rao inequality gives $Var(\boldsymbol{\theta}_i) \geqslant I_{ii}^{-1}(\boldsymbol{\theta}_i)$, meaning the best achievable precision is bounded by the square root of the inverse of the diagonal element:

$$CRLB_{\boldsymbol{\theta}_i} = \sqrt{I_{ii}^{-1}(\boldsymbol{\theta}_i)}. \tag{3.8}$$

As discussed in chapter 2, the amplitude PSF for an optical imaging system is given by the Fourier transform of the pupil function. For an in-focus system, the pupil function can be seen as a clear aperture; for a defocused system, however, additional phase needs to be accounted for. In the following simulations, the high-NA model discussed in Hanser et al. was used[76]:

$$APSF(x,y,z) = \mathscr{F}\{P(k_x,k_y) \times \mathrm{e}^{\mathrm{i}k_z(k_x,k_y)z}\}. \tag{3.9}$$

$\mathrm{e}^{\mathrm{i}k_z(k_x,k_y)z}$ is the defocus term where $k_z(k_x,k_y) = \sqrt{(2\pi n/\lambda)^2 - (k_x^2+k_y^2)}$, with n being the refractive index between the point source and the objective and λ being the wavelength. $P(k_x,k_y)$ is the in-focus pupil function, in other words, a sub-resolution point source's in-focus wavefront at the back focal plane of the objective. For pupil engineered techniques, a corresponding phase or amplitude is combined with $P(k_x,k_y)$ to generate the specific PSF.

3.6.2 Simulation and comparison

With the above discussions, one can calculate the CRLBs for a specific PSF provided that the number of photons and other parameters for the imaging system are known. Here a 100x, 1.45NA oil immersion objective is assumed with the refractive index of the immersion oil being $n = 1.515$. The sampling of the image plane is based on a 512×512 detector with pixel size of 16 µm. These parameters are selected on purpose to approximate the state-of-the-art experiment equipment available in practice for low-photon-count single-molecule experiments. In addition, the emission wavelength was assumed to be 650 nm (to approximate the *Alexa Fluor 647* dye) and the mean number of photons collected per localization was set to 4000 with a background level of 10 photons per pixel. The CRLBs in xyz over a depth range of 8 µm are calculated.

Fig. 3.13a shows the CRLBs for conventional microscope, i.e. a diffraction-limited system with a clear circular aperture. Obviously, it gives the best CRLBs in x and y at the focal plane because of the 'highly-concentrated' PSF profile. However, the CRLBs in x

and y degrade rapidly with the increasing defocus. This is due to the rapid expansion in the PSF size and thus the dramatically decreasing SNR. In the z direction, the DL-PSF changes slowly near the focal plane as the defocus changes. This means that it carries little information for z, which gives a high CRLB. Additionally, the PSF is symmetrical above and below the focal plane, making it difficult to assign a unique z coordinate to the emitter. All these aspects clearly demonstrates that conventional DL-PSF is ideal for imaging of 2D in-focus samples and not suitable for 3D applications.

Astigmatism can be used to improve the z sensitivity near the focal plane and to break the sign ambiguity associated with the DL-PSF. In this simulation, quadratic phases with opposite signs in the x and y direction were added to the pupil function as shown in Fig. 3.13b, with a resultant 1 μm deference in the tangential and sagittal focal planes. This breaks the symmetry in the x and y CRLBs. The best CRLB occurs at the focal plane of the corresponding direction. However, the z CRLB still becomes worse at the two focal planes due to the lack of depth sensitivity. Nevertheless, it eliminates the zero z-sensitivity and thus the infinite CRLB in z at the focal plane. The astigmatic PSF yields CRLBs better than 10 nm in xyz over a depth range of about 1.2 μm which doubles that of the DL-PSF on one side of the focal plane.

Bi-plane imaging is another solution to overcome the shortcomings of the conventional system. For the bi-plane technique, the collected photons are divided equally into each channel and images from both channels contribute to the localization precision. Thus the total number of photons is divided into two halves and assigned to two conventional PSFs with a 0.5 μm difference in the defocus. Then the CRLBs are calculated by concatenating the two images or from the sum of their corresponding Fisher information matrices with the assumption that the total information is the sum of that from both channels. From Fig. 3.13c, one can observe that the bi-plane technique exhibits better CRLBs than the DL-PSF. It is also better than the astigmatism in the sense that the CRLBs in x and y do not exhibit the misplacement as in Fig. 3.13b, and they both plateau near the nominal focal plane. The z CRLB, however, behaves similarly to the astigmatism as it gets worse near the two focal planes. The bi-plane technique gives a precision better than 10 nm in xyz over a depth range of about 1.7 μm which is more than double the useful range of a conventional single-focal-plane system.

The *parallax* technique is based on the conventional imaging system but splits the pupil into two halves, effectively creates two 'side views'. To simulate this, PSFs are generated for the two 'side views' individually by placing an amplitude mask that is 'half one, half zero' as shown in Fig. 3.13d. Same as the bi-plane treatment, half the photons are used for each channel and the images are then concatenated to calculate the CRLBs. The *parallax* technique also provides a better performance than the conventional and astigmatic systems. It has good z sensitivity near the focal plane and dose not exhibit the 'M-shaped' z precision as in astigmatism and bi-plane methods. Interestingly, the y CRLB

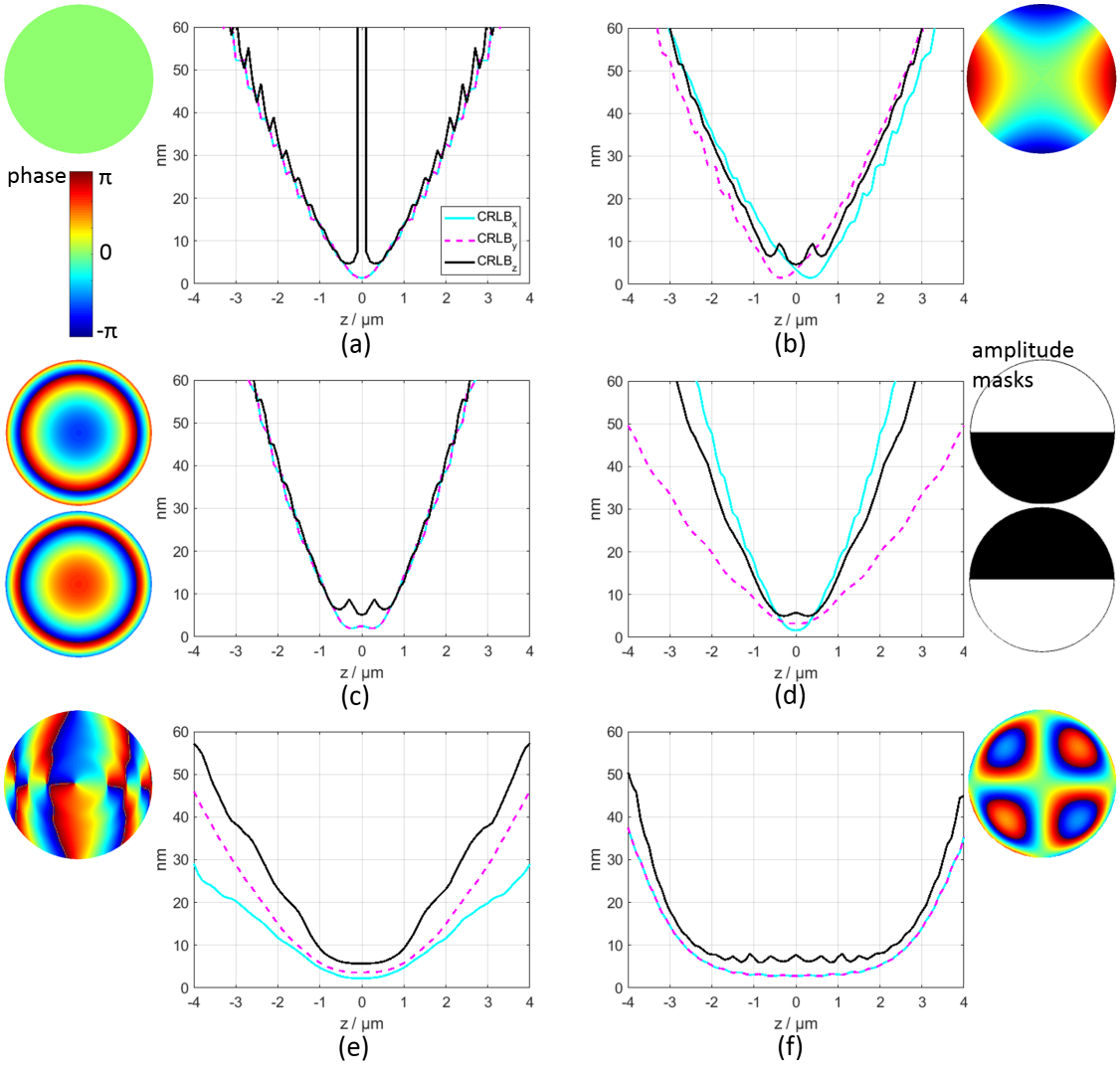

Fig. 3.13 Cramer-Rao lower bounds and corresponding pupil functions for (a) conventional DL-PSF, (b) astigmatic-PSF, (c) bi-plane technique, (d) *parallax* technique, (e) DH-PSF and (f) tetrapod PSF, assuming 4000 detected photons per localization, and an average of background of 10 photons per pixel.

is better than that in the x direction as it increases slower with the increasing defocus. This is because the effective NA is lower in the y direction as the pupil is cropped to create the two channels, resulting in a larger depth range. The *parallax* technique yields CRLBs better than 10 nm in xyz over a depth range of about 1.3 µm.

To calculate the CRLBs for the DH-PSF, an iterative simulation is performed to obtain the double-helix phase mask as described by Pavani and Piestun[16]. The phase mask and the corresponding CRLBs are shown in Fig. 3.13e. The fact that most photons are concentrated in the two rotating lobes gives rise to the SNR and thus the localization precision. The DH-PSF provides better performance in terms of both the depth range and the precision, compared to above discussed techniques. Due to its continuous rotation, the DH-PSF has a constant z sensitivity over an axial range of about 2 µm. However, the operable range of the DH-PSF is limited by both the achievable precision and the 180° rotation. In this case, about 2.6 µm can be utilized without ambiguity.

For similar purpose, the optimization process reported by Shechtman et al. was also performed to obtain a tetrapod phase mask for this CRLB analysis[73, 72]. Fig. 3.13f shows a tetrapod phase mask optimized for 4 µm together with its corresponding CRLBs. Because the mean CRLB in xyz over the depth range is optimized in the tetrapod PSF design, it displays the best CRLBs which exceeds all of the above discussed techniques, making the tetrapod PSF a preferred tool for imaging over an extended depth range and through thick samples. As can be observed, the tetrapod mask yields a continuous profile that resembles the secondary astigmatism with two peaks and two valleys. The CRLBs are flat between -2 and 2 µm, and are better than 10 nm in all dimensions over a depth range of about 4.8 µm. However, the tetrapod PSF also has some drawbacks that can not be avoided: Firstly, the z information is 'hidden' in its intensity profile especially at small defocus. This requires the PR-MLE to decode the emitter's axial position, which is computationally expensive and thus time consuming, particularly when global minimization is used to avoid the local minima in the likelihood function. Secondly, the likelihood function can be altered in the case of overlapping PSFs; thus the localization precision will be degraded[72]. These facts may lead to a worse achievable precision when using the tetrapod PSF in practice.

Then we consider the Airy-beam-based PSFs. As has been discussed in section 2.9, a single intact AB-PSF carries the emitter's depth information and thus can be utilized for 3D localization purpose. Therefore, it is worth calculating the CRLBs for single AB-PSF. A cubic phase with peak modulation $\alpha = 2\lambda$ is added to the pupil function, which yields the resultant CRLBs as shown in Fig. 3.14a. The diffraction-free propagation gives rise to the SNR at large defocus, as can be seen from the x and y CRLBs which keep below 10 nm for around 4 µm depth range on each side of the focal plane. The parabolic z-dependant lateral translation helps to maintain good depth sensitivity at large defocus. However, the disadvantages are also obvious: (1) the CRLB in z shows zero sensitivity near the focal

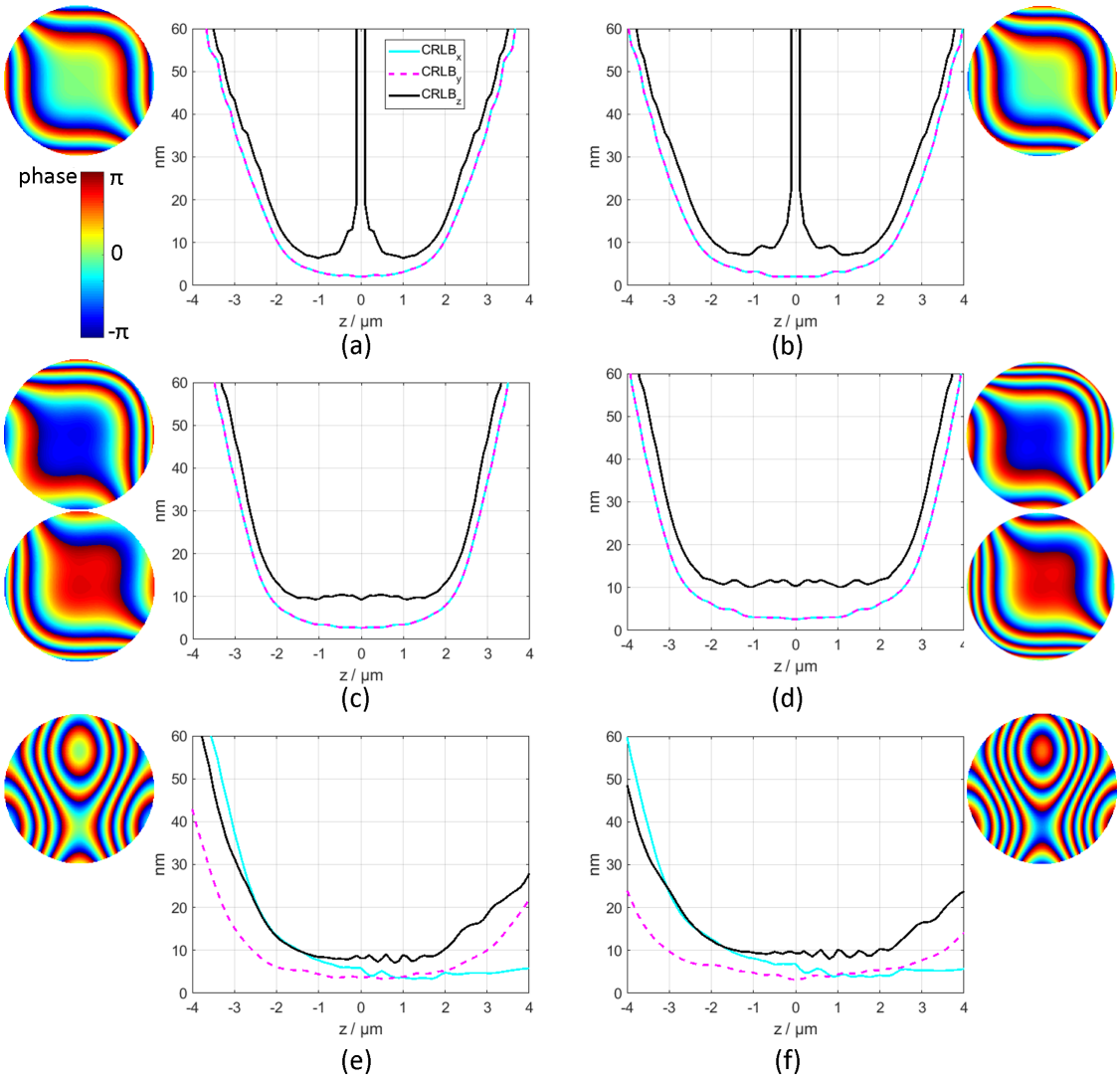

Fig. 3.14 Cramer-Rao lower bounds for AB-PSF with (a) $\alpha = 2\lambda$ and (b) $\alpha = 2.5\lambda$; Airy-CKM technique (c) $\alpha = 2\lambda$ and (d) $\alpha = 2.5\lambda$; TA-PSF with (e) $\alpha = 2\lambda$, (f) $\alpha = 2.5\lambda$. The detected number of photons is assumed to be 4000 photons per localization with an average of background of 10 photons per pixel.

plane similar to the DL-PSF. (2) the sign ambiguity in z exists as the AB-PSF translates the same way above and below the focal plane. Nevertheless, the AB-PSF still gives about 2.5 µm depth range on one side of the focal over which the CRLBs are better than 3 µm in all dimensions. Larger peak modulation in the cubic phase gives a larger depth range but a worse achievable precision, the CRLBs for an $\alpha = 2.5\lambda$ AB-PSF is also calculated as shown in Fig. 3.14b.

The combination of AB-PSF and bi-plane technique helps eliminate the zero z insensitivity near the focus, which is the Airy-CKM method highlighted in chapter 2. The same treatment is used to equally divide the total number of photons and concatenate the PSF images from both imaging channels for the calculation of the final CRLBs. With a 1.6 µm separation in the two focal planes, the Airy-CKM yields the CRLBs as shown in Fig. 3.14c ($\alpha = 2\lambda$) and 3.14d ($\alpha = 2.5\lambda$). Clearly, the z CRLB is relatively uniform. It is lower than 12 nm over a depth range of about 4 µm for $\alpha = 2\lambda$. A larger peak modulation generally gives a wider range but a higher CRLB. Besides, the CRLBs in x and y are also improved compared to that of a single AB-PSF. Compared to the bi-plane technique using DL-PSF (Fig. 3.13c), the AB-PSF significantly extends the depth range with a small compromise in the precision near the focal plane. This trade-off is necessary as the total information carried by the collected photons is limited.

Finally, we discuss the CRLBs for the TA-PSF. The results are plotted in Fig. 3.14e and 3.14f with the peak modulation being $\alpha = 2\lambda$ and $\alpha = 2.5\lambda$ respectively. As expected, the TA-PSF also maintains high localization precision in three dimensions over an extended axial range. Interestingly, the CRLBs for the x and y directions are not the same. This is due to the asymmetry in the TA-PSF profile and can be confirmed with the experimental results in section 3.3. Unlike most reported PSFs, the CRLBs are not symmetric above and below the focal plane, especially the CRLB in the x direction. Similar to the AB-PSF, the operable depth range is also tunable by adjusting the peak modulation of the phase mask: a smaller α gives less depth range but better precision in all space dimensions. For $\alpha = 2\lambda$, the TA-PSF is capable of exhibiting CRLBs better than 10 nm over 3.2 µm axial range for the specified signal-to-noise conditions; for $\alpha = 2.5\lambda$ nearly 4 µm can be achieved, which is slightly worse but comparable to the tetrapod PSF.

In conclusion, the Airy-beam-based PSFs and the tetrapod PSF yield significantly larger depth range than other existing approaches including DL-PSF, astigmatic PSF, bi-plane with DL-PSF, *parallax* and DH-PSF. The tetrapod PSF provides the larges depth range but it suffers from degraded precision in the scenario of PSF overlapping and is more computationally expensive. The Airy-CKM and the twin-Airy techniques provide slightly worse depth range to precision ratio but yield the advantages of high tracer density and fast data processing. Also, the cubic and twin-Airy phase masks are analytic, which provides flexibility for adjusting modulation strength and for its fabrication.

Techniques	Implementation	Continuous mask or not	Analytic mask or not	Commercial Availability	Comments
DL-PSF	conventional microscope	–	–	–	–
Astigmatism[39]	cylindrical lens	yes	yes	yes	–
Multi-plane[35]	multiple cameras	–	–	–	reduced SNR for each additional camera
Parallax[62]	split pupil by mirror	–	–	–	–
Wedge prism[63]	split pupil by wedge prism	–	–	–	
DH-PSF[16, 56]	$4f$ with DH mask	no	no	no	180° rotation limit
DH-PSF (analytic mask)[60]	$4f$ with analytic DH mask	no	yes	yes	180° rotation limit
Corkscrew PSF[59]	$4f$ with corkscrew mask	no	no	yes	sequential images needed for deducing z
SB-PSF[17]	$4f$ with truncated cubic mask	no	yes	no	additional photon loss from trucated pupil
Tetrapod PSF[73, 72]	$4f$ with tetrapod mask	yes	no	yes	degrade precision at low SNR and with overlapping PSFs
Airy-CKM[65, 66]	$4f$ with cubic mask	yes	yes	no	lower peak signal
TA-PSF	$4f$ with cubic mask	yes	yes	no	lower peak signal

Table 3.1 Comparison of currently available techniques for 3D localization microscopy.

3.6.3 Comparison of other aspects

There are additional considerations when choosing between these particle localization techniques, such as the complexity of implementation, the photon-efficiency of the phase mask, the commercial availability of components and systems, and the cost. Some of these aspects are listed in TABLE 3.1, where whether a phase mask can be described by an analytic function on the pupil is also considered. This is important in the sense that it influences both the flexibility for adjusting modulation strength and the phase mask fabrication. For example, efforts have been made to achieve an analytic pupil function for the DH-PSF that can be adapted to specific imaging and sensing tasks[60]. Similarly, whether a mask exhibits a continuous surface is also important for its fabrication, as phase profiles with 2π jumps that cannot be unwrapped are not ideal for manufacturing and can also cause some additional photon loss due to scattering. A smooth phase profile is also required for implementation of a phase mask using a deformable mirror (which is preferred over SLMs due to their higher photon efficiency).

3.7 Conclusion

In this chapter, the twin-Airy method has been proposed for 3D point-localization microscopy, which displays two Airy-beam-like lobes in one PSF. The two lobes diverge on one side of the nominal focal plane but converge on the other, enabling the emitters' 3D coordinates to be encoded in a single image. The TA-PSF preserves the extended depth range provided by the single Airy beam but eliminates the complexity in multi-channel configurations as in the Airy-CKM approach. Such a PSF can be generated with a carefully designed twin-Airy phase mask which contains two quasi-cubic profiles in the pupil plane. The phase profile is continuous; thus, it can be easily manufactured as a refractive mask using currently available processes or produced on a deformable mirror, which is significantly more photon-efficient than a liquid crystal spatial light modulator.

The TA-PSF also allows image deconvolution with a single pre-recorded PSF. This chapter describes a deconvolution-based algorithm to localize point emitters with the TA-PSF, which does not degrade the precision for overlapping PSFs and shows promise for imaging high emitter densities than MLE-based techniques. A localization precision of better than 30nm in *xyz* over an axial range of 7 µm has been demonstrated on a 60x, 1.4NA system from 6800 photons per localization. This implies that the TA-PSF is potentially useful for applications like single-molecule tracking with thick samples comparable to the size of a cell. On a larger length scale, it will be shown in the next chapter the applicability of the TA-PSF to blood-flow measurement in a live zebrafish. Its potential for broader applications, such as real-time 3D TFM will be discussed in the last chapter.

In addition, it has also been shown that pupil-size mismatching and phase mask misalignment result in various alterations in the AB-PSF and TA-PSF profiles, which can be utilized as guidelines for optical alignments in practice. As an assessment of performance, CRLBs have been calculated for the proposed techniques, which compare favorably to the existing approaches in terms of achievable depth ranges.

Chapter 4

In vivo blood-flow characterization

In this chapter, the previously reported techniques are applied to measurement of blood flow in living zebrafish, a modal biological system that have drawn much attention in the *in vivo* study of hemodynamics due to their advantages such as fast growth and good transparency. Understanding the spatio-temporal properties of blood flow in the cardiovascular system is crucial for cardiac morphogenesis, angiogenesis and vasculogenesis[91–96], yet high-speed quantitative methods able to provide blood flow parameters in large 3D volume with high precision are still highly desirable. It will be shown that the Airy-beam-based techniques combined with microinjection are promising tools for *in vivo* characterization of blood flow with high temporal and spatial resolution, and with the capability to image within large volumes. Images of the blood vessels reconstructed from light-sheet microscopy will also be presented as a validation of the particle localization approaches.

4.1 Background material

Recent studies have revealed that blood flow is a key factor controlling aging processes in the skeletal system[94], and plays an important role in brain functioning[97–99] and in the continued growth of some organs such as the liver[95]. Additionally, flow-induced forces, such as the wall shear stress and transmural pressure, are believed to have an important influence on heart development and valve formation [91, 92].

Conventionally, blood-flow dynamics are measured with techniques such as fluorescence correlation spectroscopy on a confocal laser-scanning platform[100–102]. The velocities are deduced from the temporal intensity fluctuations of fluorescence and the scanning direction of the laser focus. This can quantify blood velocity at relatively high spatial resolution, but is usually limited to small observation volumes[103] and low concentrations, and the point-scanning nature of confocal microscopes makes it unsuitable

for time-resolved imaging. The same is true for optical vector field tomography which combines optical projection tomography with high-speed multi-view acquisition and particle-image velocimetry (PIV)[103]. It can produce a 3D velocity map of the blood flow at the whole organism level. However, because the sample must be rotated in order to obtain 3D information, this approach is not suitable for resolving the time-varying details of pulsatile flow in the cardiovascular system. The recent work by Zickus and Taylor uses high-speed multi-depth acquisition combined with digital synchronization with the beating heart to enable 3D measurement of the flow in zebrafish[26]. However, the multi-depth acquisition limits the axial component of the flow to be deduced. In addition, using endogenous tracers, e.g. the erythrocytes, results in a limited spatial resolution (several microns) which is typically low for accurate measurement of hemodynamic parameters such as wall shear stress[104].

To provide three-dimensional real-time operation, Lu et al. introduced defocusing digital particle-image velocimetry combined with microinjection of tracer particles for the *in vivo* measurement of blood-flow dynamics[105]. As has been discussed in section 1.2.2, this technique employs a three-pinhole mask at the pupil plane, enabling coding and decoding 3D locations of tracer particles[106]. Such a three-pinhole mask, however, severely limits the optical throughput of the imaging system, resulting in a reduced SNR and thus a limited localization precision. Moreover, the PSF expands rapidly with defocus resulting in a low seeding concentration and small axial range (about 40 µm as reported).

Pupil-engineered point-spread functions provide precise localization (tens of nanometers) of point emitters, and have been widely used in the filed of super-resolution imaging, single-particle tracking in cells or microfluidic experiments. Particularly, the AB-PSF and TA-PSF reported in this work provide extended detection volume, which is suitable for imaging of complicated and spatially extended vasculature. To the best of the author's knowledge, such techniques have not been applied to the field of *in vivo* blood-flow mapping.

In the following sections, the Airy-beam-based techniques combined with microinjection of high contrast tracer beads are utilized for the *in vivo* measurement of blood flow in 3 dpf zebrafish. It will be shown that sub-40 nm precision and sub-1 ms temporal resolution can be achieved over more than 100 µm axial range on a 20×, 0.5NA system. Tracer trajectories are recorded and reconstructed in 3D space within both cardinal and intersegmental vessels, and these are validated with the help of an image of the blood vessels reconstructed from image stacks acquired using a modified OpenSPIM system[107].

4.2 Zebrafish as a model system

The zebrafish has been widely used as a model biological system to study developmental biology[108, 109], cancer, toxicology, drug discovery, and molecular genetics[110–112]. The zebrafish embryo develops in a sequence of well-defined stages, from freshly fertilized egg through larva to adult fish as shown in Fig. 4.1 and it has several unique advantages over other model animals which are important to some researchers.

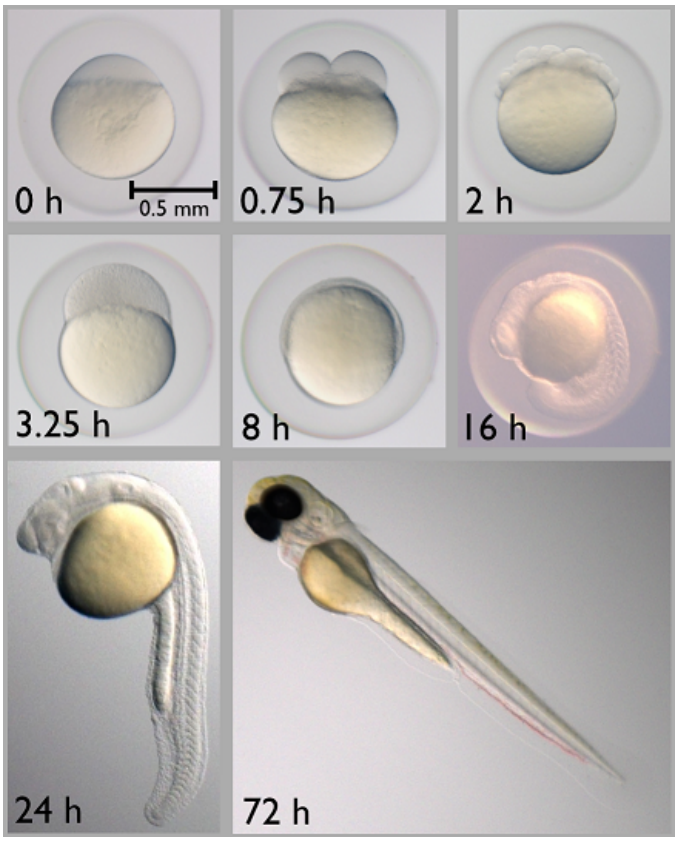

Fig. 4.1 Development stages of the zebrafish. Zebrafish develop rapidly, hatching at 2 days as a free-swimming larva. 3 dpf zebrafish are most interesting in this experiment for easy injection purpose. Image reprinted from Hendel[113]. Material under CC BY-SA 4.0 licence.

The zebrafish are small and robust and are cheaper to maintain than mice. Zebrafish have a similar genetic structure to humans and their genome has been fully sequenced. They share 70% of genes with us and 84% of genes known to be associated with human disease have a zebrafish counterpart[114, 115]. They are easy to breed and grow at an extremely fast rate. As zebrafish eggs are fertilized and develop outside the mother's body it is an ideal model organism for studying early development. It has well-understood, easily observable and testable developmental behaviors. Furthermore, well-characterized mutant strains are readily available. Zebrafish have the unique ability to repair heart muscle. As a vertebrate, the zebrafish has the same major organs and tissues as humans. Their muscle, blood, kidney and eyes share many features with human systems.

Optically, zebrafish are generally transparent from egg to the stage of larva and has low refractive index, enabling the imaging with optical microscopes. With the help of chemical treatment, even the pigmentation can be removed[116], making them completely transparent. Also, there are numerous genetically modified zebrafish lines available that have various fluorescence in various tissues or organs, allowing imaging of specific targets and phenomenon in multi-imaging channels.

Due to the above-mentioned benefits, zebrafish have been used in this work for the measurement of blood-flow dynamics with Airy-beam-based point-localization techniques.

4.3 Microinjection and sample preparation

High-contrast tracers are crucial to achieve precise measurement of the blood flow[104]. Compared to endogenous tracers such as the blood cells, fluorescent beads are bright and uniform in size and shape, making the particle tracking more robust. In this work, microinjection of fluorescent beads was performed to zebrafish embryos for the measurement of the blood flow.

The beads used were 1 µm-diameter fluorescent polymer (Bangslabs, FSEG004 envy green with excitation peak at 525 nm and emission peak at 565 nm), which were chosen as their fluorescence emission spectrum is separated from the green fluorescent protein (GFP) emission of the transgenic zebrafish (*flk1:GFP*) blood vessels (emission peak at 509 nm). The beads were suspended in purified water and washed three times by centrifuging at 9800 relative centrifugal force for 4 minutes to remove additives. Washed beads were resuspended in $1\times$ PBS solution, at the ratio of 1 part bead solution to 20 parts PBS and sonicated in a water bath sonicator for 10 minutes to preclude bead aggregation before injection.

The prepared solution was then transferred in a glass needle (several microns thick as shown in Fig. 4.2a) which was attached to a micro injector (Eppendorf Transjector 5246) with manipulator (Eppendorf Micromanipulator 5171). Three dpf zebrafish embryos were anesthetized using $200\,\mathrm{mg\,l^{-1}}$ tricaine mesylate solution for 10 minutes before injection (the fish remained at this concentration of tricaine throughout the experiment). For a 3 dpf zebrafish, the common cardinal veins (CCV) tend to be flat and thick, and lie at the anterior trunk and are close to the skin of the embryo, which was chosen as the injection spot (Fig. 4.2b). A petri-dish was filled with agarose with tiny holes dug to mount the zebrafish head up and tail down the as shown in Fig. 4.2c. The injection was performed with the help of a stereo microscope (Zeiss SteREO Discovery. V8).

Following injection, the fish were transferred in 1.5% melt agarose (with a temperature of around 30 °C) and then sucked into a hollow square glass capillary with inner

dimensions of 1 mm × 1 mm and 0.2 mm wall thickness (VitroCom Inc., 8100-050) for imaging. The square capillary was then mounted on a piezo stage (PInano Z Microscope Scanner, P-736.ZR2S) with a 3D printed holder (Fig. 4.7a). To achieve the best imaging performance, the walls of the square capillary were mounted perpendicular to both the optical axes of the illumination and the detection optics. Preferably, the left-right axis of the fish was aligned with the optical axis of the detection optics while the dorsoventral axis of the fish was aligned with the optical axis of the illumination optics. The sample was maintained in a temperature of 28.5 °C (which is optimal for zebrafish embryo development) throughout the imaging using an incubator mounted on the microscope.

Note that the injected beads gradually adhere to the blood vessel walls[104], and the time window for observation is limited to about 20 minutes. Smaller bead can increase the observation time window, however, it will yield lower SNR as short exposure time is necessary for high-speed imaging of blood-flow dynamics.

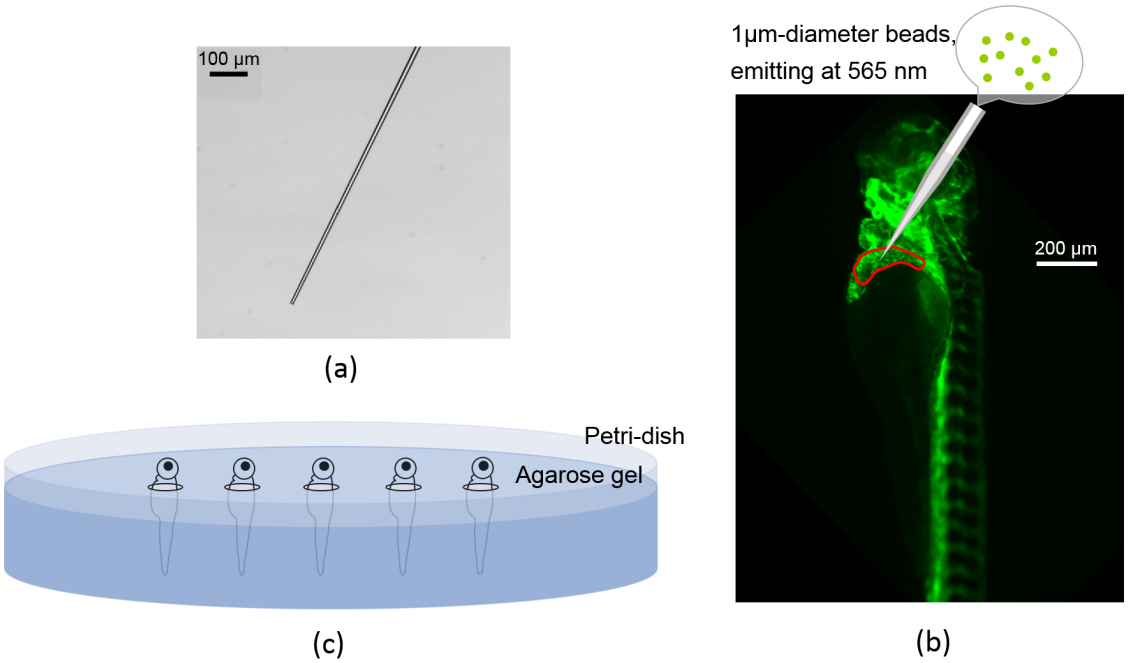

Fig. 4.2 (a) An image of the glass needle used for microinjection. (b) The injection spot indicated in red, i.e. the common cardinal vein which has a relatively wide morphology at 2-3 days post fertilization, transforming into a much narrower vessel from end of day 3. This is the preferred location for injections at this age. (c) Zebrafish mounted in agarose gel for the microinjection, a schematic.

4.4 *In vivo* blood-flow mapping with the Airy-CKM technique

4.4.1 Experimental setup

The experimental setup was based on a Nikon Eclipse Ti microscope and consisted of three additional paths: one for imaging and two for illumination, as indicated in dashed boxes in Fig. 4.3. The excitation for tracking the fluorescent beads was a 532 nm diode-pumped solid state laser (Thorlabs DJ532-40), the beam was diffused with a rotating ground glass and then focused at the back focal plane of the 20×, 0.5NA objective to launch wide-field epi-illumination (green box). The fluorescence was collected by the same objective and formed an intermediate image after the tube lens which was then re-imaged by the Airy-CKM particle tracking arm.

The Airy-CKM particle tracking arm was implemented using a $4f$ relay as indicated in the orange dashed box in Fig. 4.3. The focal length of the relay lenses was 200 mm. A refractive cubic phase mask (laser-fabricated with a peak modulation of $\alpha = 7\lambda$) was placed at the re-imaged pupil plane between two relay lenses to generate the AB-PSF. A lateral beam splitter was used to form two images with opposite defocus offsets $\psi + \Delta\psi$ and $\psi - \Delta\psi$ respectively; thus, it yields spatial disparities in the deconvolved images that is proportional to the absolute defocus of each point source ψ (section 2.4).

As has been discussed in chapter 2, the detectable volume of the Airy-CKM technique is tunable by changing the peak modulation in the cubic phase mask. Larger α yields a larger diffraction-free range in the AB-PSF, providing a larger operable axial range. For microscope with a 20×, 0.5NA objective lens, the detectable range can be extended to more than 600 µm using a cubic phase no weaker than $\alpha = 12\lambda$. However, larger α results in a broader PSF profile and a lower peak SNR, and this is accompanied by a reduced image translation and responsivity to depth. Despite that, this reduction in image translation can be compensated by increasing the defocus offset $\Delta\psi$, so that the responsivity to depth can be retained [65]. Overall, the best localization precision is achieved using the smallest α that ensures a diffraction-free AB-PSF for the required axial range of localization. Here the combination of a 20x, 0.5NA objective and a $\alpha = 7\lambda$ cubic phase mask provides a depth range of nearly 200 µm; this is sufficient to cover the thickness of the region of interest (ROI) in this experiment.

The particle tracking arm was calibrated before the *in vivo* imaging. As shown in Fig. 4.4a (left), a stack of PSFs are acquired near the nominal focal plane with defocus ranging from -100 µm to $+100$ µm. The green curve indicates the lateral translation in the PSF which encodes the depths of the point emitters as described in the Airy-CKM technique. Such a PSF exhibits little variation in its intensity profile thus allowing Wiener deconvolution to be performed with a single pre-recorded PSF yielding the compact

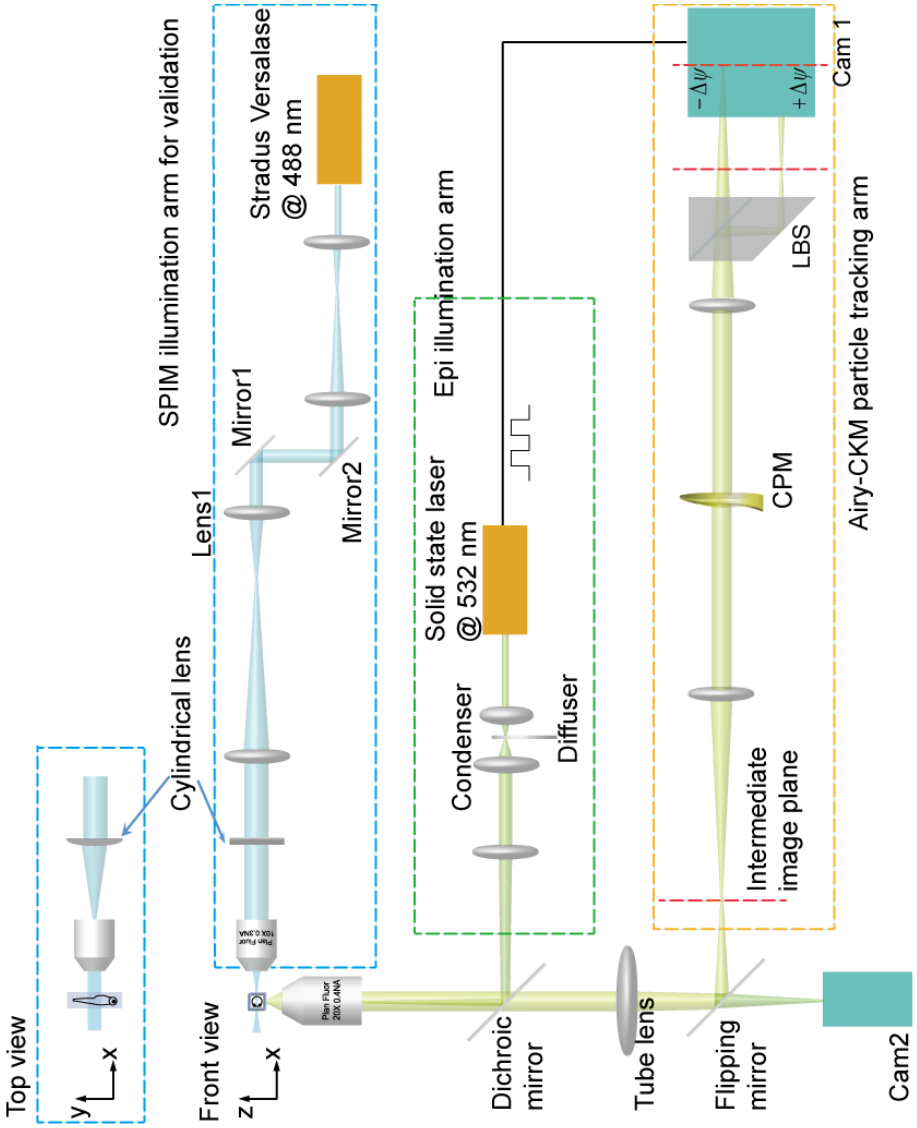

Fig. 4.3 Schematic of the experimental setup. The orange box indicates the particle tracking arm: A 0.5 NA, 20× CFI Plan Fluor objective was used to image the tracer particles. A cubic phase mask was placed at the re-imaged pupil plane of a $4f$ relay system. The lateral beam splitter generated two images of the same scene but with opposite defocus offsets on the same sensor of camera 1. Wide-field epi-illumination was used for the 3D particle tracking with a 532 nm solid state laser as light source. The blue box shows the SPIM illumination arm, the light sheet was launched using a 10×, 0.3 NA CFI Plan Fluor objective and a cylindrical lens with 75 mm focal length. The SPIM images were acquired with Camera 2. The sample was mounted in a square glass capillary on a piezo z stage. CPM: cubic phase mask; LBS: lateral beam splitter. (Adapted from Zhou et al., 2018[66])

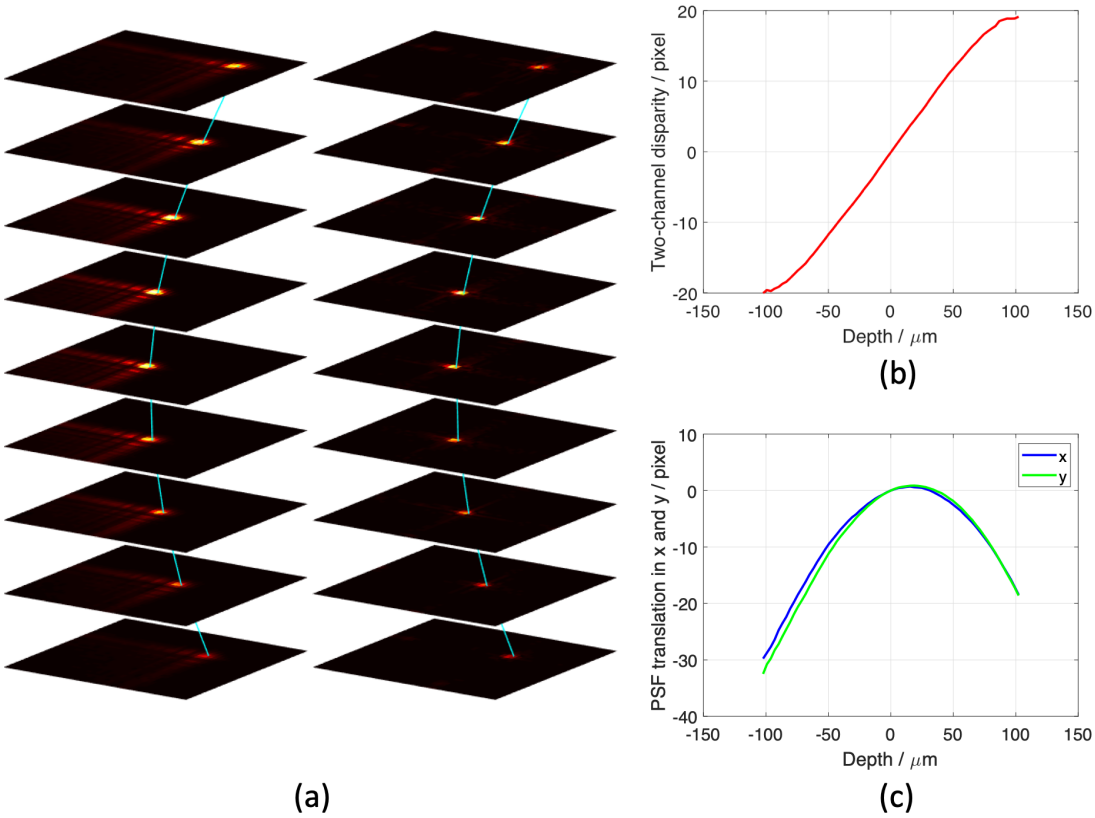

Fig. 4.4 (a) AB-PSFs and corresponding deconvolved PSFs. Calibration curves of the 20×, 0.5NA system with an $\alpha = 7\lambda$ phase mask: (b) Lookup table relating the two-channel disparity to the z coordinate of the particle. (c) Image translations in x and y as a function of z, which are used to correct the image shifts once z is deduced. Images adapted from Zhou et al.[66], materials under Creative Commons licence CC BY.

profile as shown in Fig. 4.4a (right). The deconvolved PSF exhibits the same lateral translation but a higher peak signal level and a more compact intensity profile. As discussed in chapter 2, the depth-dependent image translation is measured by duplicating the image with dissimilar defocus on the same camera sensor using a lateral beam splitter. Thus, the particle coordinates can then be deduced from the image disparity in two imaging channels. Recall that the imaging system needs to be calibrated for this purpose. Fig. 4.4b and 4.4c show the calibration results of the Airy-CKM particle-tracking arm which can be used as lookup tables for the 3D localization algorithm as described in section 2.4.3.

4.4.2 Correction for systematic drift

During long-term imaging, it is in most cases inevitable to observe drift. This can be from sample movement (e.g. the drift of the fish inside the agarose before its solidification) or the drift from instruments caused by temperature fluctuation or mechanical relaxation effects. This includes the z-directional drifting of the objective due to gravity, the xy

drifting of the motorized stage. Such drift can easily be in the range of several hundred nanometers or even several microns during the time of a few minutes.

Although, this is problematic for some scanning-based techniques, it is less of a problem for the 'single-shot' techniques including the Airy-beam-based methods where the whole volume is imaged in a single snapshot. This means that the drift is systematic at each time point, and thus can be corrected by subtracting the global movement of all detected tracers. A straightforward way to measure this global movement is to seed the agarose gel with fluorescent fiducial markers, the displacements of these markers over time will therefore reflect the systematic drift. Note that the zebrafish may have sudden movement when exposed to laser light, such frames are not used in the data processing.

4.4.3 Results

The injected fluorescent beads flowed with the blood and circulated within the cardiovascular system as high contrast tracers, they were imaged with the Airy-CKM particle tracking arm once the sample was mounted. As an extensively studied model animal, zebrafish have a relatively simple and well understood cardiovascular system. Fig. 4.5a shows the heart and blood vessels of a 3 dpf zebrafish recorded with a stereo microscope in green fluorescence where one can observe the quasi-periodic structure of the intersegmental vessels. The chosen ROI is near the cloaca indicated by the red rectangle covering several intersegmental vessels, the cardinal artery and the cardinal vein where some predictable 3D structure can be observed.

Video sequences of the blood flow were recorded. Fig. 4.5b shows a single image from a 2000-frame video. Each AB-PSF is the image of a bead in the blood. The 3D tracer locations in each frame can be extracted from the AB-PSFs with the algorithm discussed in section 2.4.3. Due to the extended depth range of the AB-PSF, blood flow throughout the whole thickness of the fish (less than 200 μm in this case) can be recorded in a single snapshot without optical sectioning. This allows a high volume-imaging rate (up to hundreds of snapshot volumes per second depending on the ROI and limited only by the camera performance). The trajectory of each bead was tracked through successive frames within the image sequence using an algorithm developed by Crocker and Grier[117]. The displacements between two successive frames can be used to approximate the instantaneous velocity. Fig. 4.5c shows the reconstructed 3D trajectories of the tracers that were tracked within the ROI, where the coloring indicates trajectories of individual beads. As shown, most tracers flow through the cardinal artery and cardinal vein, with a few of them entering the intersegmental vessels supplying the surrounding muscle tissue. The spatially expanded 3D structures of the intersegmental vessels and capillaries can be observed as the injected tracers flow through them.

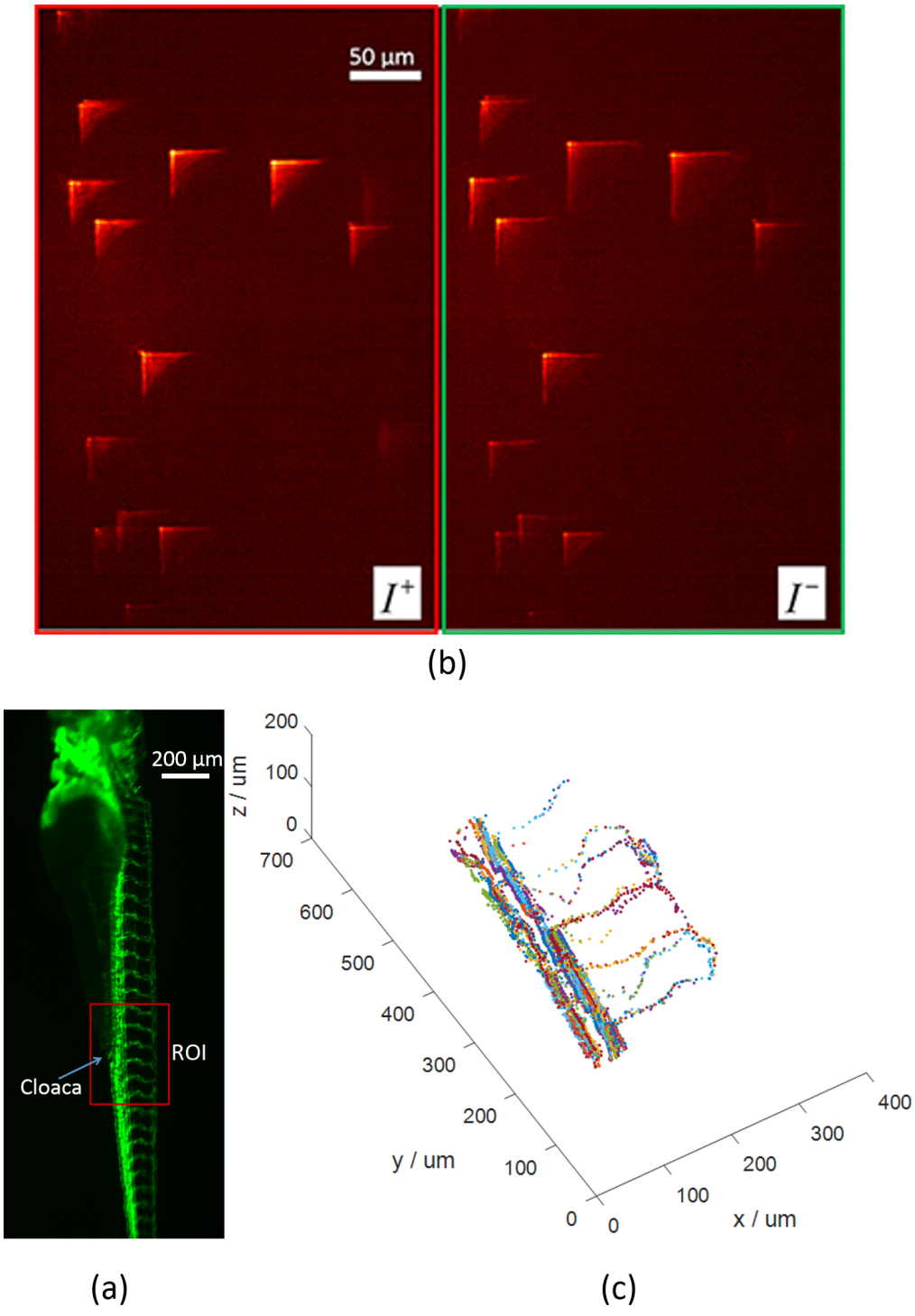

Fig. 4.5 (a) The region of interest (ROI) of this experiment. (b)PSF-encoded images from both imaging channels of the 1 µm fluorescent tracer beads flowing within the ROI. (c) 3D trajectories of tracers within cardinal and intersegmental vessels of zebrafish, reconstructed from 2000 frames. Different color refers to the trajectory of different tracers. A video showing the tracers flowing with the real-time blood flow and the 3D reconstruction of tracer trajectories is published with ref[66]. Images adapted from Zhou et al. [66], materials under Creative Commons licence CC BY.

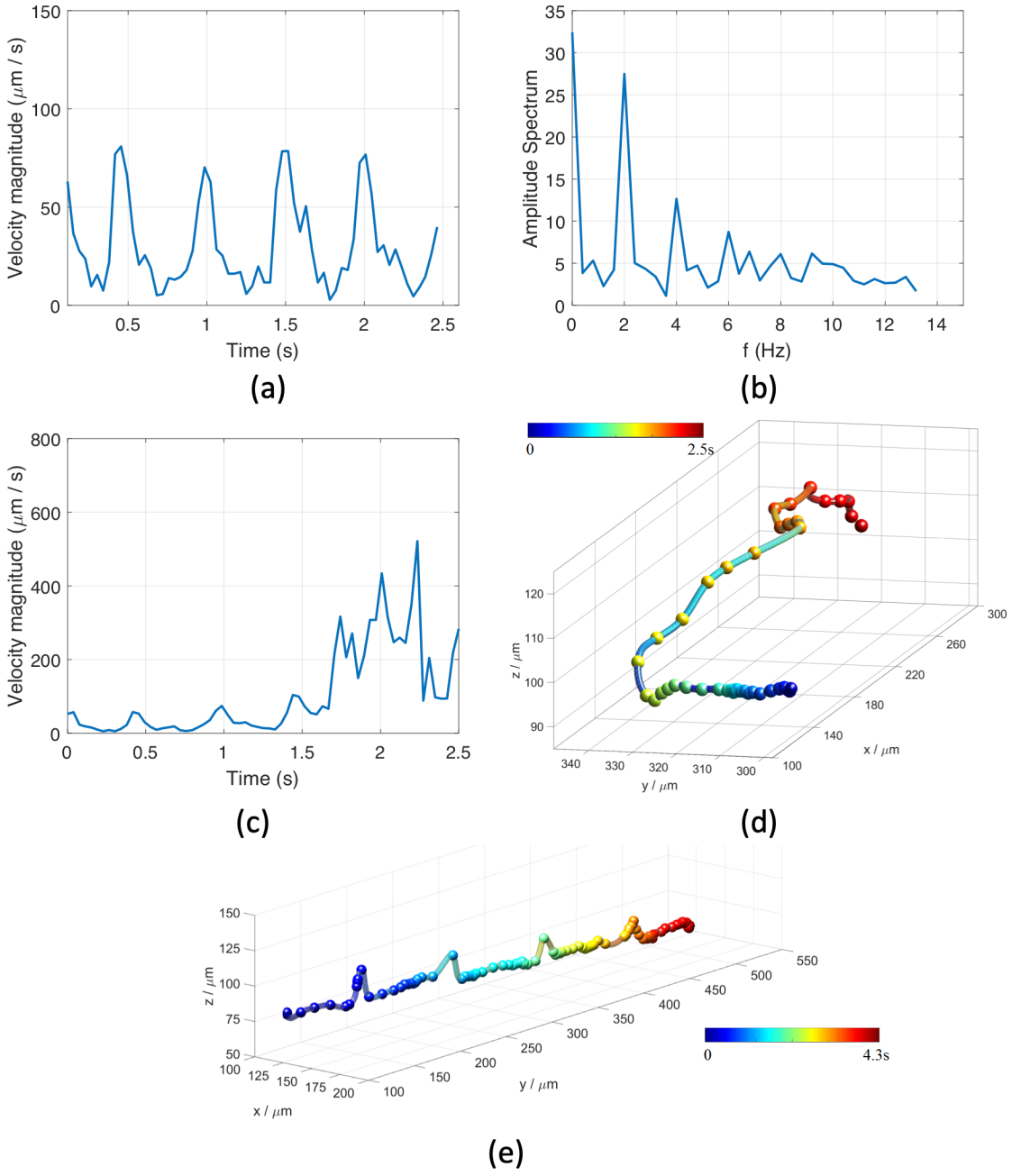

Fig. 4.6 Temporal and spatial variation of the tracer velocity. (a) Velocity of a tracer flowing within a cardinal vessel. (b) Fourier spectrum of the velocity profile in (a). (c) Velocity of a tracer that enters an intersegmental vessel from the cardinal vessel. (d) 3D trajectory of the tracer in (c), color-coded for time. (e) Trajectory of a bead flowing though a cardinal vessel. Significant variations in the z coordinate indicate non-uniformity in the tissue refractive index. (Adapted from Zhou et al. [66], materials under Creative Commons licence CC BY.)

With the 3D tracer trajectories obtained, one can investigate the spatial and temporal properties of the 3D blood velocity of the zebrafish. Fig. 4.6a shows the velocity magnitude of a single bead which flows within a cardinal vessel varying with time and Fig. 4.6b shows its Fourier spectrum. The velocity variation of the tracer can be seen to be quasi-periodic, with a fundamental frequency of about 2 Hz which represents the heart rate. Since injected tracers are relatively light and small compared to the blood cells, they have negligible influence on the function of the zebrafish heart and the stable heart rate also indicates unperturbed conditions throughout this experiment. Fig. 4.6c shows the changing in velocity of a tracer particle as it enters an intersegmental vessel from a cardinal vessel, of which the trajectory is shown in Fig. 4.6d. The peak velocity increased dramatically from below $100\,\mu m\,s^{-1}$ to about $600\,\mu m\,s^{-1}$, due to the fact that intersegmental vessels are much narrower.

The experiment also reveals that the recovered trajectories may exhibit systematic artefacts due to imaging through tissues and organs of dissimilar refractive indices which produce variations in the apparent locations of beads. For example, a predictable and deterministic modulation was observed in the z coordinate of beads flowing in the cardinal vessels (Fig. 4.6e) which may result from the periodic structure of the ribs, intercostal vessels, or the lymphatic vessels. These modulations are not present in trajectories recorded near the tail of the fish where the tissue macrostructure is more uniform. Imaging of the beads at the far side of a blood vessel containing randomly positioned and oriented blood cells also introduces irregular lensing and phase modulation of the apparent bead positions, resulting in a random uncertainty in the localization accuracy of about half a micron.

4.5 Validation with selective plane illumination microscopy

4.5.1 Generation of the light-sheet illumination

To validate the spatial accuracy of the 3D tracer trajectories obtained with the Airy-CKM technique, a SPIM imaging arm was built to enable the optical sectioning of the zebrafish blood vessels subsequent to the imaging of fluorescent beads, as illustrated in the blue boxes in Fig. 4.3. As has been discussed in the literature review, SPIM is a well-developed optical sectioning technique to image live samples that employs a thin sheet of light from the side of the sample as illumination[23, 107]. It provides a greatly increased acquisition speed and optical throughput compared to point-scanning confocal microscopy, and also reduced photobleaching and photodamage to the sample.

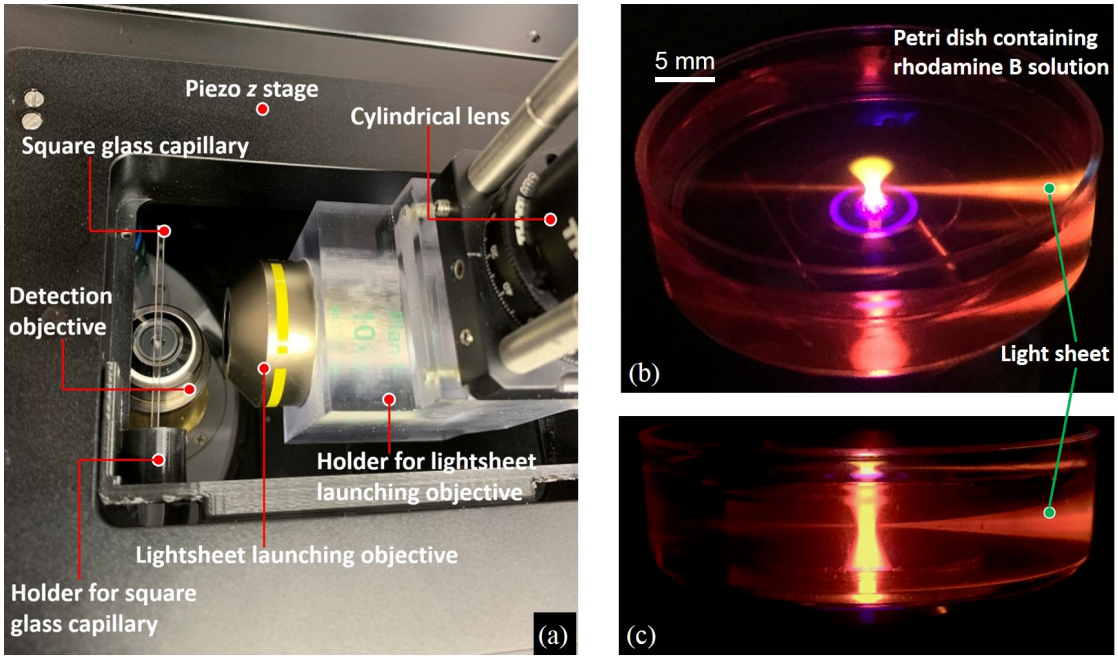

Fig. 4.7 (a) The experimental configuration of the SPIM illumination. (b) Visualization of the light sheet obtained and the focus of the detection objective using rhodamine B solution. (c) View from the side of the light sheet.

The SPIM system used here is based on the OpenSPIM[107] but modified to work with air objectives for both illumination and detection on an inverted microscope (Fig. 4.3). A fiber-coupled laser at 488 nm (Stradus VersaLase) was used for illumination with two telescopes expanding the beam diameter by twice and four times respectively. A 75 mm cylindrical achromat lens (Thorlabs ACY254-075-A) was focusing the beam in the top view at the back focal plane of a 10×, 0.3 NA Nikon CFI Plan Fluor objective (the light-sheet-launching objective) with a working distance of 16 mm. Thus, the illumination beam were focused in the front view but collimated in the top view, forming a thin sheet of light that was perpendicular to the z axis, i.e. optical axis of the detection objective. Mirror 1 was placed at the focal point of Lens 1 to enable z directional adjustment of the light sheet. The light-sheet-launching objective was mounted on a 3D-printed holder (Fig. 4.7a) then connected to the 30mm cage system on which the whole SPIM illumination arm was built. The cage system was built on a 2 inch pole, with a translation stage to adjust its height.

The thickness of the light sheet can be well described by Gaussian beam optics and is determined by the NA of the system, or equivalently, the incident beam diameter at the back aperture of the objective. With small angle approximation, the divergence of the Gaussian beam in the front view (Fig. 4.3) can be written as

$$\theta \approx \frac{\lambda_0}{\pi n \omega_0}, \quad NA = n \times \sin(\theta), \tag{4.1}$$

where λ_0 is the free-space wavelength, n is the refractive index of the media (air in this case) and the ω_0 refers to the beam waist in the front view, which is the thinnest part of the light sheet and determines the z resolution of the SPIM. Combine the above two equations we have

$$\omega_0 \approx \frac{\lambda_0}{\pi NA}. \tag{4.2}$$

A thinner light sheet can be obtained with higher NA, at the cost of a smaller Rayleigh length which determines the useful field of view and is defined as:

$$z_R = \frac{\pi n \omega_0^2}{\lambda_0}. \tag{4.3}$$

In this experiment, the back aperture of the light-sheet-launching objective was not filled with the excitation beam, the effective NA was measured to be about 0.15. Therefore, the thinnest light sheet achievable with this home-built SPIM system was about $2\omega_0 \approx 2\mu$m which agrees with the experimental measurement.

The generated light sheet needs to be aligned with the detection objective to provide the best imaging performance, i.e. (1) the alignment of the axes of the light sheet and the detection objective in the top view (Fig. 4.3) (2) the alignment of the optical axis of the detection objective with thinnest part of the light sheet in the front view. For the coarse alignment, rhodamine B solution was used to visualize the light sheet and the optical path of the detection objective as shown in Fig. 4.7b and 4.7c. For the fine alignment, the cylindrical lens was rotated by 90° so that the side of the light sheet was imaged on Cam2.

4.5.2 SPIM images and validation results

The transgenic zebrafish line (flk1:GFP) expresses GFP in the blood vessels, enabling the 3D structure of the blood vessels to be obtained with a z scan subsequent to the imaging of tracer beads. A piezo z stage was employed to move the sample with 1 µm step size over a scanning range of 200 µm. The 20×, 0.5 NA Nikon CFI Plan Fluor objective (the same one used for the Airy-CKM particle tracking) was used to detect the fluorescence signal. An image was then formed on camera 2 with the flipping mirror removed and corresponding filter set and dichroic mirror changed. Lastly, the image stack was processed to reconstruct the vessel structures and to compare with the particle tracking results.

Fig. 4.8 illustrates a superimposition of the 3D tracer trajectories obtained with the Airy-CKM method (green spheres) with the z stack images obtained with the SPIM (red)

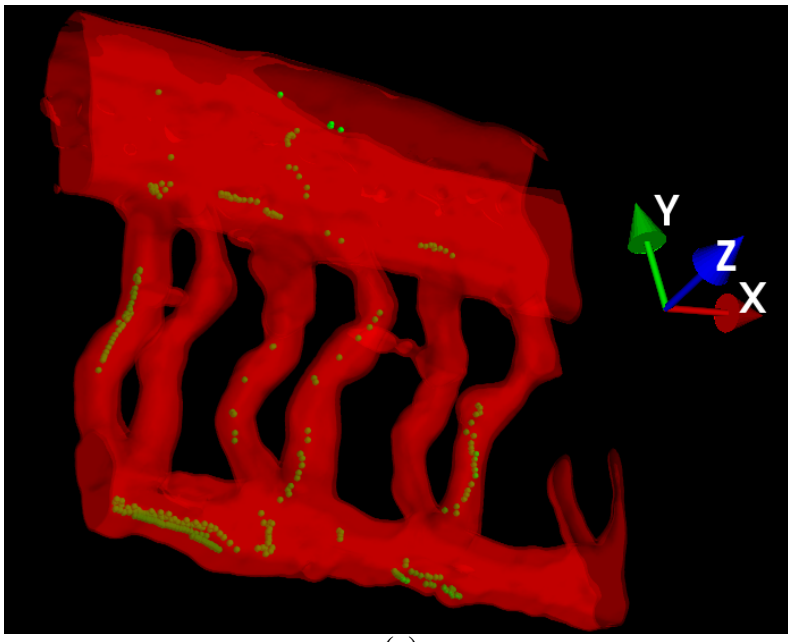

(a)

(b)

Fig. 4.8 Composite images showing detected tracer locations (green spheres) embedded within a surface rendering (red) of the 3D blood vessel structure obtained from quasi-simultaneous SPIM imaging. (a) View of several tail segments; (b) detail of a vessel junction. The recovered bead coordinates lie within the blood vessels, demonstrating that the Airy-CKM method is correctly identifying the 3D coordinates of the beads. Image adapted from Zhou et al.[66], materials under Creative Commons licence CC BY.

which was rendered with open source Mayavi package and displayed using maximum intensity projection. The fish was positioned such that the its left-right axis was along the optical axis of the detection objective (i.e. z direction) and its sagittal plane is parallel with the x and y axes. Fig. 4.8a shows several segments near the tail of the fish while Fig. 4.8b shows the detail of a vessel junction. As can be observed, the intersegmental vessels spread in 3D in a way similar to what was recorded in Fig. 4.5a. The fact that all the trajectories coincide with the blood vessels indicates that the proposed Airy-CKM technique has good spatial accuracy in both xy and z through turbid media and is a promising tool for the characterization of hemodynamics in thick samples. Multi-view animations of the composite image and beads flowing within SPIM-reconstructed blood vessels can be found online, published with ref[66].

4.6 Blood-flow imaging with TA-PSF

In addition to experiment with the Airy-CKM technique, the TA-PSF was also tested for the application of *in vivo* blood-flow measurement. The same sample preparation procedure was used as described in section 4.3.

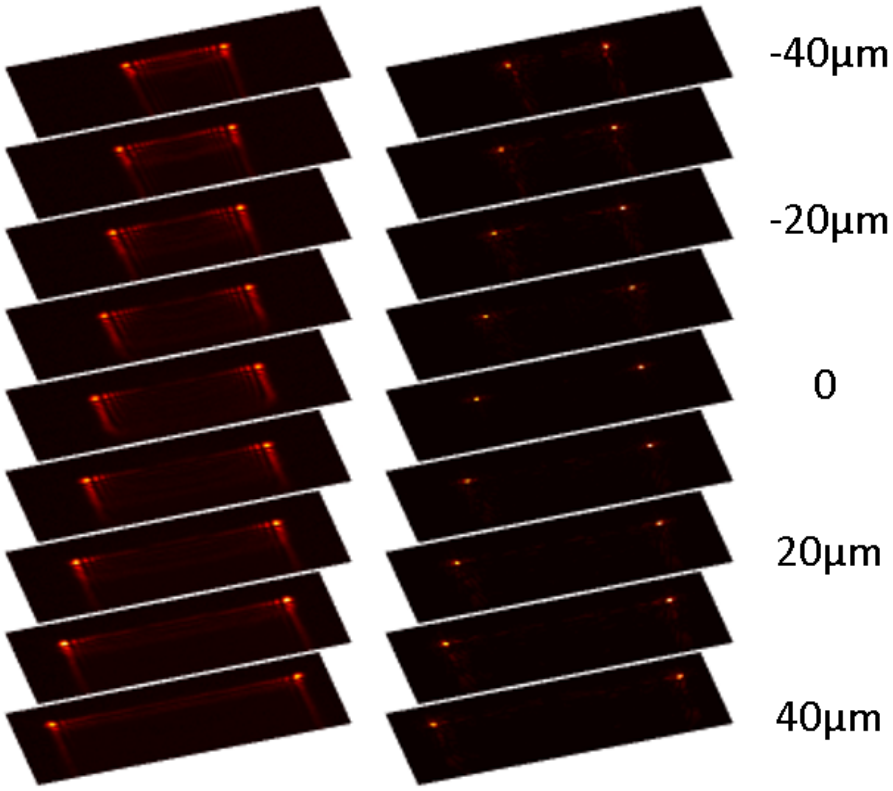

Fig. 4.9 (a) TA-PSFs from the 20x, 0.5NA system used for *in vivo* blood-flow measurement, recorded with 10 µm step. (b) corresponding deconvolved TA-PSFs.

4.6.1 Characterization of TA-PSF on a 20× 0.5NA system

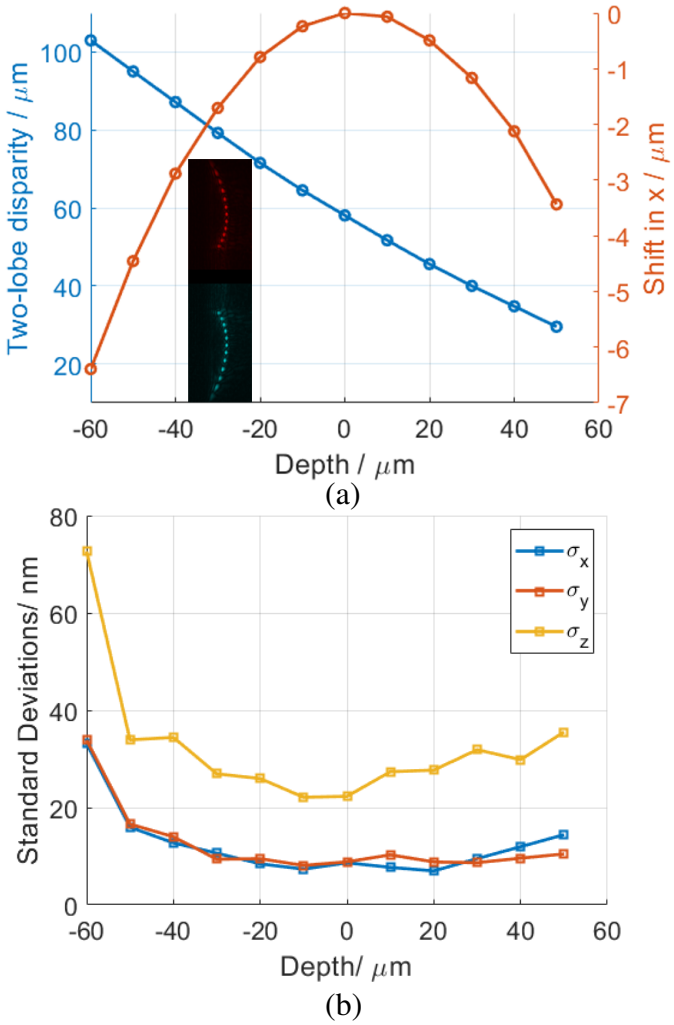

Fig. 4.10 (a) Calibrations for the 20X 0.5NA system with twin-Airy phase mask. Around 100 µm depth range can be achieved. (b) *in vitro* localization precision test, the standard deviations were calculated from 100 repeated measurements at each depth. A fluorescent bead was immobilized on the surface of a coverslip, and the same illumination and acquisition conditions as that for the *in vivo* experiment were used.

An $\alpha = 10\lambda$ refractive twin-Airy phase mask was utilized with the same 20x, 0.5NA objective for the blood-flow characterization. A relay lens with a focal length of 100 mm demagnified the pupil size to match the size of the phase mask. The depth range obtained with TA-PSF in this configuration was about 100 µm, which is 15 times greater than the nominal depth of field of 5.8 µm. The same fluorescent tracer beads and thus the same laser were used here as in the previously discussed experiment.

Fig. 4.9 shows a stack of TA-PSFs and the corresponding deconvolved PSFs over a depth range of 80 µm. The deconvolved PSFs exhibit a more compact profile which enables identification of overlapping TA-PSFs as will be shown in this experiment. The PSFs diverge in the image plane in a similar way compared to that in the high NA, high magnification scenario (section 3.3), which can be observed from the calibration curves

in Fig. 4.10a. The two-lobe disparity changes quasi-linearly with the changing depth, meaning the TA-PSF has a nearly uniform z sensitivity over its operable depth range.

In Fig. 4.10b, an estimate of the localization precision is shown for localization of *in vitro* fluorescent beads with photon fluxes similar to that can be achieved for imaging blood flow. As shown, an xy precision of better than 17 nm combined with a z precision better than 36 nm can be expected over more than 100 µm depth range for the blood-flow measurements.

4.6.2 Results

The chosen ROI (Fig. 4.11a) was more toward the tail of the fish compared to the results obtained with the Airy-CKM technique, so that the influence from non-uniformity in the tissue refractive index was not observed. A video of the microinjected tracers was recorded using a 2560×2160 sCMOS sensor (Andor Zyla with 6.5 µm pixel size) at a frame rate of 50 fps.

Fig. 4.11b shows a snapshot of the injected tracers flowing within the zebrafish blood vessels. Each '['-shaped image (the TA-PSF) represents a tracer bead. Most beads flow within or adhere to the cardinal artery and cardinal veins, resulting in most TA-PSFs appear clustered at the lower half of Fig. 4.11b. Following processing as previously explained and summarized in chapter 3, the 3D location, and thus the trajectory of each tracer can be obtained as shown in Fig. 4.11c. Each color denotes the trajectory of a single tracer bead that was recovered from a video sequence of 5000 frames. Fig. 4.11d is a view of the tracer trajectories in the xy plane where we can observe that the cardinal artery goes directly towards the posterior end of the fish while the cardinal veins spread like a net. Fig. 4.11e gives a view of the cross-section of the fish where the intersegmental vessels supplying nearby tissues around the body of the fish can be seen. The tracer locations conform to the expected 3D structures, providing additional validation of the 3D localization performance of the TA-PSF.

4.7 Possible extensions to these experiments

Provided that enough data points are collected, it is possible to reconstruct the 3D velocity field of the blood flow. The wall shear stress, which is a function of the velocity gradient of blood near the endothelial surface, can also be deduced. This will hopefully be useful for the study of cardiovascular disease and atherosclerosis. A challenge for achieving these goals comes from the continuous beating of the heart, meaning that the velocity field inside a blood vessel should be a time-varying but periodic flow. Thus to measure the blood flow at a specific phase of a heart beating cycle, a number of heart beat cycles

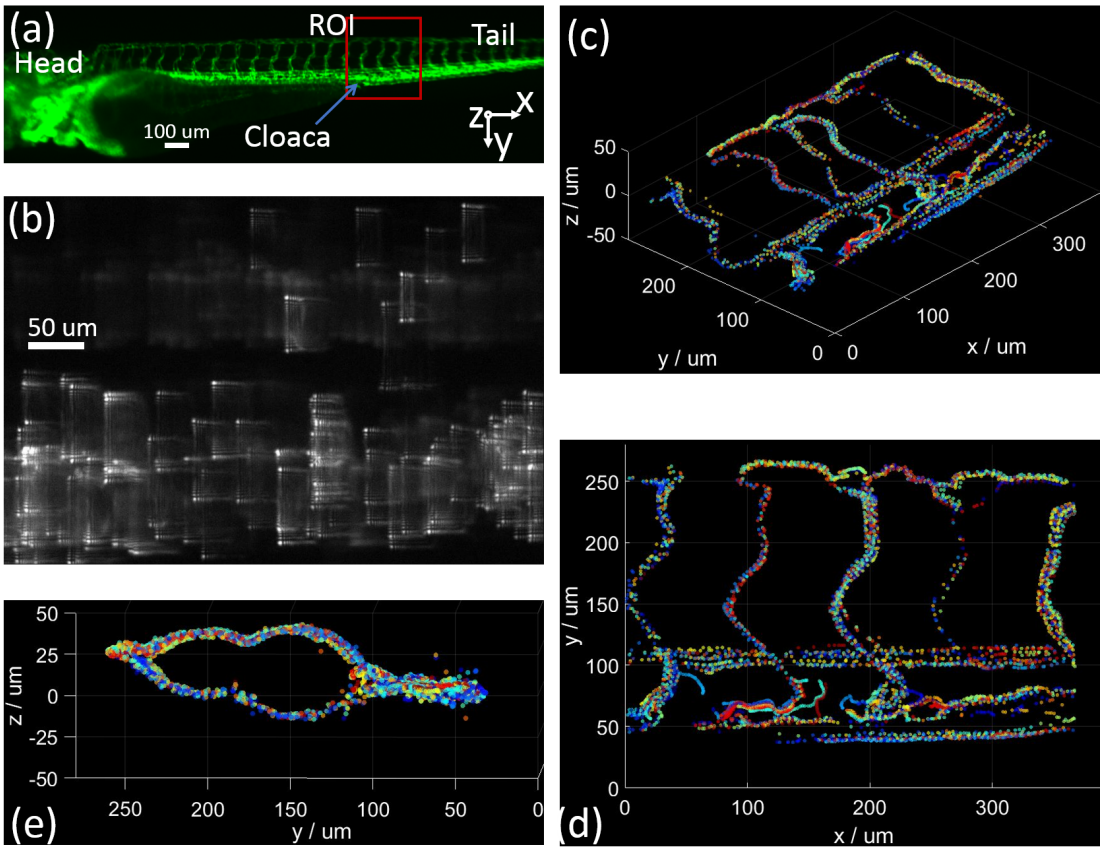

Fig. 4.11 3D blood-flow characterization in a live 3 dpf zebrafish. (a) Fluorescent image of zebrafish blood vessels. The region of interest (ROI) is near the cloaca of the zebrafish as indicated with the red rectangle. (b) A raw image frame showing injected tracer beads in blood vessels. (c) three-dimensional tracer trajectories. Each color corresponds to the trajectory of one tracer bead. (d)*xy* view of the 3D tracer trajectories. (e)*yz* view of the tracer trajectories (cross-section perpendicular to the anteroposterior axis of the fish).

need to be recorded, resulting in huge amount of data. A possible solution to this problem is to 'digitally freeze' the beating heart as reported in ref[26], where the heart beating is synchronized and images are only acquired at the desired phase of the heart beating.

Although the reported techniques were demonstrated to observe the blood flow in the specific ROIs, it is possible characterize the hemodynamics in other parts of the zebrafish, for example, in the zebrafish brain. Biologists have been interested in the formation of brain vasculature because the vasculature in the brain is composed of a highly ramified vessel network tailored to meet its physiological functions[118]. It has been shown that the developing vasculature in the zebrafish midbrain undergoes not only angiogenesis but also extensive vessel pruning, which is driven by changes in blood flow[118]. However, imaging in the brain is more challenging as the head of the zebrafish has irregular shapes and surfaces compared to the ROI selected in the previous sections. Therefore, it is more critical to match the refractive index of the agarose gel to the zebrafish to avoid refractive errors. More importantly, the fish needs to be carefully positioned so that denser tissues (e.g. cartilages or bones) are not in the imaging path.

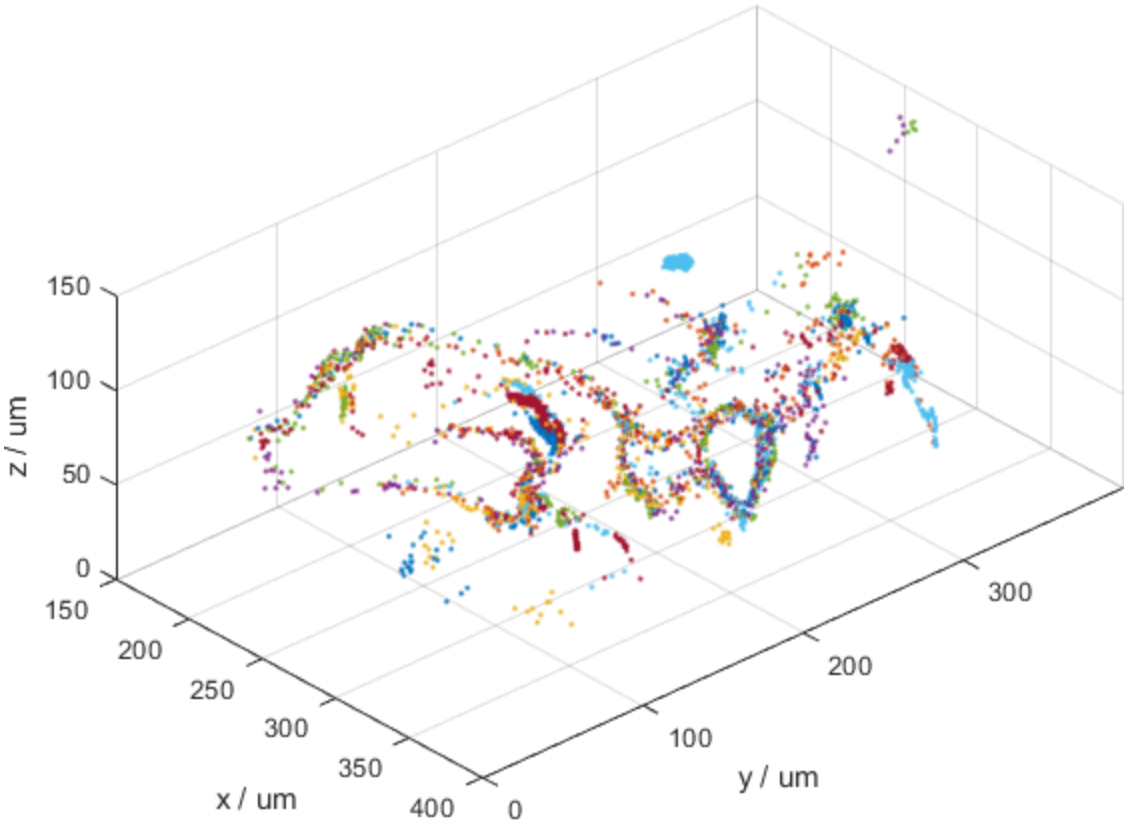

Fig. 4.12 Particle tracking within the blood vessels in the brain of a 3 dpf zebrafish. Each color indicates the trajectory of a single tracer bead.

Fig. 4.12 shows a preliminary result of the blood-flow tracking in the head of a 3 dpf zebrafish. More complicated vascular network can be observed compared to that near the cloaca of the zebrafish. The above mentioned vessel angiogenesis and pruning at a certain

location can be inferred from the probability of the bead appearance and the velocity of the local flow field. In this way, Airy-beam-based techniques are potentially useful for the study of the brain vasculature formation.

4.8 A note to high-speed imaging

High frame rate can be achieved (limited only by the camera) in these experiments for the following reasons: (1) Measurement of flow dynamics is usually not limited by photon flux since the tracers are bright; short exposure can be used. (2) The whole volume of interest can be imaged with the AB-PSF or the TA-PSF in a single snapshot. This is crucial for imaging of transient phenomena such as cell adhesion to blood vessel walls and arrhythmic heartbeats.

Modern sCMOS cameras are able to image at very high frame rate (>100fps) which can be further improved by reducing the active area on the sensor and binning the pixels. In the flow tracking experiment, Andor Neo or Zyla cameras are used with 2560×2160 sensor size. The highest speed with the full-chip activated is around 100fps and a frame rate higher than 200fps can be achieved with 2×2 pixel binning. Further pixel binning will provide higher frame rate. However, because image deconvolution requires the PSF to be well sampled to preserve the fine structure and high spatial frequency, further binning is not preferred as it will reduce the localization precision. In the zebrafish experiments, active area on the sensor can be set to the size of the specific region of interest to speed up the pixel readout.

4.9 Conclusion

In this chapter, the Airy-CKM and the twin-Airy techniques have been applied to achieve 3D particle tracking in the zebrafish circulatory system with sub-1 ms temporal resolution and sub-40 nm precision. To the best knowledge of the author, this is the first application of pupil-engineered PSFs in the field of *in vivo* blood-flow measurement.

The vastly extended detectable volume enables imaging through the whole thickness of the zebrafish without optical sectioning. The high spatial and temporal resolution and snapshot 3D-imaging nature of this technique will permit direct characterization of important biomechanical parameters such as wall shear stress that are highly challenging to measure *in vivo* and transient phenomena such as cell adhesion to blood vessels, immune cell locomotion and arrhythmic heartbeats. The particle tracking arm, i.e. the $4f$ relay, can be easily implemented as a plug-in for standard microscopes. In addition, the use of a refractive phase mask provides a much greater optical throughput compared to diffractive methods, such as a spatial light modulator, while also being much lower cost.

Beyond the specific illustrative application that has been presented here, the Airy-beam-based point-localization techniques also hold promise for a broader range of applications in biomedical imaging. This will be further discussed in the last chapter and preliminary results will be presented for time-resolved 3D traction-force microscopy to measure forces exerted by biological cells[11, 119].

Chapter 5

Conclusion and future work

The precise localization of point sources in optical microscopy enables nanometer-resolution imaging of single-molecules and biological dynamics. Existing approaches for point localization, however, suffer from limitations such as small depth ranges, low optical throughput, complicated implementations or degraded performance in presence of overlapping PSFs. This work utilizes the lateral translation property and the diffraction-free propagation of Airy-beam-based PSFs to localize point emitters in 3D space with the key advantages of extended depth range, high optical throughput and potential for imaging higher emitter densities than using other techniques. Two new approaches have been proposed, namely the Airy-CKM and the twin-Airy techniques which were validated and demonstrated for *in vivo* blood-flow imaging. In summary, the following aspects have been investigated:

- The extended axial range and the depth-dependent lateral translations of the AB-PSF and the deconvolved AB-PSF were investigated theoretically, experimentally and by simulation. It is shown that the AB-PSF generated with a cubic phase mask located at the pupil plane of the microscope exhibits lateral translations that are quadratic to the z coordinate of the emitter. In the cases of extremely high NA and small peak modulation α, the PSF translation curve differs from a parabola. Nevertheless, this translation can still be utilized for 3D point localization once it is calibrated.

- The Airy-CKM technique was developed employing a bi-plane configuration to deduce the AB-PSF translation and thus the xyz coordinates. A deconvolution-based algorithm was reported which yields compact recovered images of PSF. Such an algorithm works well with overlapping PSF and shows potential for high packing density scenarios. In addition, it is less computationally expensive than algorithms based on MLE. The bi-plane configuration gives nearly double the axial range than using complementary masks, as reported in Jia et al.[17].

- The Airy-CKM technique was validated in microfluidic experiments. Various experiments were performed by tracking fluid flow inside FEP capillaries that was seeded with fluorescent beads. Assessment of the localization precision was also performed under various SNR levels at different focal planes.
- The twin-Airy technique was developed for further simplicity, which combines two Airy-beam-like lobes in one PSF. The two lobes diverge on one side of the nominal focal plane and converge on the other, eliminating the sign ambiguity associated with a single AB-PSF or the SB-PSF. A deconvolution-based algorithm has also been proposed for the twin-Airy PSF, which deals well with most PSF overlapping scenarios.
- The twin-Airy PSF was implemented experimentally on both high magnification, high NA (100x, 1.45NA) and relatively low magnification, low NA (20x, 0.5NA) systems. With the former setup, a precision better than 30 nm was achieved in *xyz* over a depth range of 7 µm, showing its potential for single-molecule tracking and 3D super-resolution microscopy over extended depth ranges. The latter gives about 100 µm depth range with a precision better than 40 nm.
- Both proposed techniques have been utilized for *in vivo* imaging of blood flow dynamics in 3 dpf zebrafish. High-speed extended-volume blood flow tracking was performed in various types of blood vessels of the zebrafish. Tracer trajectories were reconstructed in three dimensions which show the spatial-temporal information of the blood flow. To the best of the author's knowledge, this is the first application of pupil-engineered PSFs to the field of blood-flow dynamics measurement. The single-snapshot volume imaging enables real-time imaging of the blood flow, which surpasses conventional techniques such as the optical coherent tomography. The extended depth range allows the whole thickness of the zebrafish to be imaged. Note that the reconstructed trajectories were also validated with the 3D reconstructed blood vessels imaged with a home-built SPIM system.
- A comparison of the proposed techniques to existing mainstream techniques has been performed in terms of Cramer-Rao lower bound (CRLB) simulation. It is shown that the Airy-beam-based PSFs give extended depth compared to most existing techniques including astigmatism, *parallax*, and the DH-PSF. Although the tetrapod PSF provides a slightly larger depth range, the Airy-beam-based PSFs have the advantage of faster localization algorithm and the capability to localize overlapping PSFs without compromising precision.
- The possibility of 3D point localization using a single intact AB-PSF was also discussed in this work. The fact that the 'center of intensity' is constant was utilized for deducing the lateral translation in the AB-PSF and thus the z coordinate.

Compared to the bi-plane configuration, this approach is simpler although it fails in low SNR scenarios and has sign ambiguity on the two sides of the focal plane.

5.1 Aspects to be improved

Despite that encouraging results have been achieved using the Airy-CKM and twin-Airy techniques developed in this work, the results could be further improved by addressing some experimental and computational aspects, these can be summarized as follows:

- Deconvolution-based algorithms have potential to recover high packing densities; within the time limit of this PhD, this was not fully investigated. This is a desirable property in flow dynamics characterization and experiments like dSTORM. A comparison with other techniques can be performed and there is room for algorithm and code to be improved.
- The frame-to-frame particle linking algorithm used in the data analysis was developed by John Crocker et al.[86] which minimizes the sum of the squared displacements of each tracer $\sum \delta_i$ between two successive frames. Such an algorithm works well when the displacement between two successive frames are smaller than the average spacing between the tracer particles, which requires higher frame rate for detecting faster motions. Other frame-to-frame particle tracking algorithms and software exist[85, 120, 121] which are not further investigated.
- In the zebrafish experiment, the wall shear stress is of more interest to biologists which can be calculated from the tracer trajectories provided that enough data points are acquired near the blood vessels wall. This is out of the scope of this thesis and was not performed within this work.

5.2 Ongoing and future work

Localization microscopy covers a broad spectrum of applications where the fast volume acquisition and the extended depth range are often desirable features. In addition to the *in vivo* characterization of hemodynamics, this work also explores the possibility of applying the Airy-beam-based PSFs to other biological or bio-engineering problems. In this section, we will briefly introduce the on-going experiments and future directions related to this research. First of all, the on-going work on time-resolved traction-force microscopy will be discussed, with some preliminary results. The samples used for this experiment are provided by Dr Oana Dobre, Dr Sara Trujillo and Ana San Felix Garcia-Obregon. Secondly, a brief discussion on the possibility of extended-depth single-molecule tracking and super-resolution microscopy using Airy-beam-based PSFs will be provided.

5.2.1 Time-resolved traction-force microscopy

It has been revealed recently that mechanical forces have an impact on a broad spectrum of cellular processes including proliferation, differentiation, gene expression, tumor metastasis and invasion, collective migration, wound healing and tissue morphogenesis[122]. The mechanical forces between cells and their embedding matrix are important for migration of cells, tissue maintenance and organ development. Therefore, measurement of these cellular forces with high spatiotemporal resolution is essential for understanding of cellular functions.

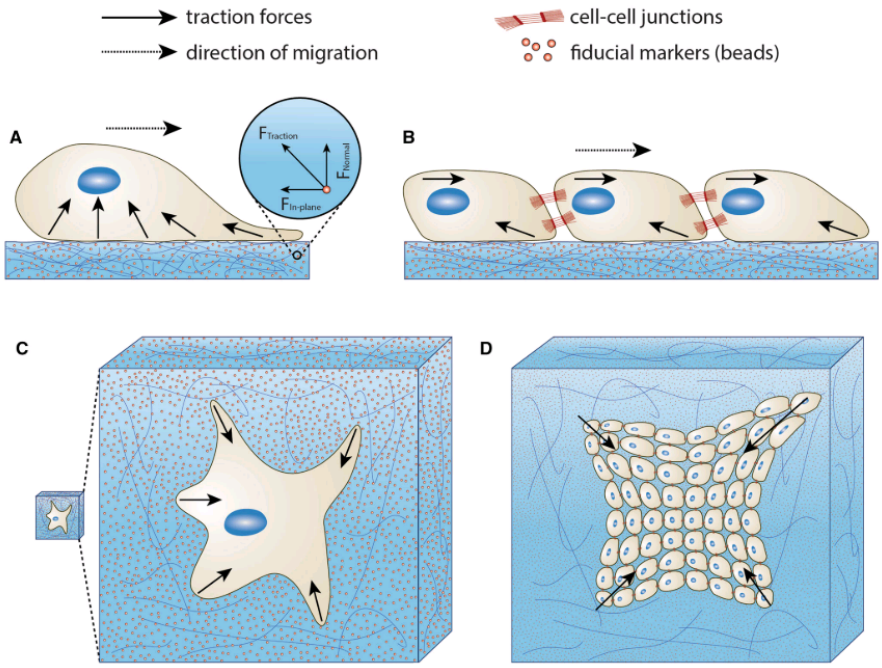

Fig. 5.1 Single cell and multicellular traction forces in 2D and 3D systems. Traction forces exerted by (a) single cell migrating on a 2D substrate, (b) population of cells migrating collectively on a 2D substrate, (c) single cell migrating in a 3D matrix, and (d) population of cells migrating collectively in a 3D matrix. Cell-generated traction forces displace fiducial markers embedded in the substrate or matrix as cells migrate. Traction forces can be quantified by measuring the displacement of beads. Image reprinted from Nerger et al.[122] with permission. Copyright 2016, Springer International Publishing.

Various ways have been utilized to measure the cell forces including the atomic-force microscopy, among which traction-force microscopy is the most successful and broadly-used probing technology of cell forces not only for the simplicity of its implementation, flexibility to mimic cellular conditions, but also for the well-established analysis pipeline[123]. In terms of interaction configurations between the cell and their embedding matrix, TFM can be divided into two main categories: the 2D configuration and the 3D configuration (Fig. 5.1). In 2D TFM experiments, cells interact with a thin elastic hydrogel by adhering to a protein functionalized surface[124]. The hydrogel is seeded with fluorescent beads as fiducial markers. When the cells apply forces on the hydrogel

substrate, imaging of the bead positions over time allows the elastic displacement of the gel to be quantified, which combined with knowledge about the mechanical properties of the hydrogel allows the forces applied by the cell to be recovered[123]. Note that the traction forces in the 2D configuration can be measured both in 2D and 3D depending on the approaches used, measuring the 3D traction field of a cell cultured on a 2D substrate is often referred to as 2.5D TFM. In the 3D TFM, the cell is completely embedded in a hydrogel. Compared to the 2D configuration which has been extensively investigated, far less is known about traction forces during the migration of cells in 3D microenvironments because of challenges associated with imaging and sample preparation[122]. Specifically, measuring bead displacement in 3D gels can be problematic because the working distance and operable depth range associated with high NA, high magnification objectives limit on deep imaging into the hydrogel.

In terms of imaging configurations, the majority of the reported TFM experiments are based on laser-scanning confocal microscopes that provide optical sectioning in 3D and good spatial resolution (about 200 nm in xy and 500 nm in z). In addition, confocal microscopes allow imaging of both the fluorescent beads and the cell membrane which is important for the analysis of force field close to the cell. However, confocal-based systems suffer from the following drawback: the point scanning nature of confocal microscopy slows the imaging process, although improved techniques like the spinning disk have been utilized, the imaging time required scales with the volume of interest. This makes it unsuitable for real-time imaging within large volumes of fast cellular interaction and of the extracellular matrix degradation dynamics, which are the two important aspects in studying the migration of cells[125].

Engineered PSFs provide ~ 10 nm precision, real-time imaging of the tracer beads in the 3D volume (up to 100 volumes per second), with which TFM can be accelerated thus cell forces can be monitored in real time. In addition, due to the need to image deep inside the 2D substrate or 3D matrix, extended-depth-range techniques are preferred. The Airy-beam-based techniques developed in this work meet the requirements of high acquisition speed, high spatial resolution and large detection volume; thus have potential for improving the acquisition speed of traction-force microscopy. As an extension of the work in this PhD, the developed techniques are utilized for characterization of the cell traction forces exerted by various type of cells interacting with various hydrogels. Both 2D and 3D hydrogel systems are investigated.

Using engineered PSFs for real-time high-resolution TFM is promising, yet it faces several challenges. The two main challenges and their possible solutions are: (1) For 3D systems, engineered PSFs can only provide precise measurement of the 3D locations of the embedded tracer beads, but not the cell membrane. This requires the combination of engineered PSFs with other imaging modalities such as confocal microscopy or SPIM. SPIM provides faster sectioning and less sample bleaching, and thus is a good candidate

for imaging the cells. In fact, several groups have demonstrated light-sheet microscopy as a tool capable of imaging 3D single cells in their extracellular matrix[126]. (2) Although Airy-beam-based PSFs perform well in PSF overlapping scenarios, to achieve the bead density necessary for generating the 3D displacement field and thus the traction-force field is still challenging. A solution to this challenge is to use a mixture of several types of beads that emit at dissimilar wavelengths. By combing the tracer bead locations from multi-channels, a high tracer density can be achieved.

Experiment setup and sample preparation

The same experimental configuration as used for the *in vivo* blood-flow measurements (Fig. 4.3) can be utilized for measuring cell traction forces. An objective with higher magnification and higher NA can be used due to the fact that individual cells are smaller than the vascular structure in zebrafish. In this experiment, the incubator on the microscope maintains the temperature to $37°C$ as the samples contain mouse cells.

For the 2D TFM system, the cells tend to spread flat on top of the hydrogel substrate. Therefore, they can be imaged using conventional wide-field microscopy combined with epi-illumination. Glass-bottom petri-dish is used here to hold the sample and the cell culture media. In the case of 3D TFM system, the cells keep their 3D shape, the light-sheet illumination arm is used to achieve 3D optical sectioning of the cell membrane. A special sample holder is designed to allow the light-sheet illumination from the side and the detection from the bottom of the sample at the same time. As shown in Fig. 5.2a, the sample holder is 3D printed with two glass windows (cover slips) glued on one side and the bottom. Aquarium silicone glue is used to avoid toxicity to the cells. The sample holder is fixed on a z piezo stage so that the sample can be scanned through the light-sheet illumination to enable 3D reconstruction of the cell membrane structure.

Preliminary results

Fig. 5.2 shows some preliminary results from the traction-force experiments. Fig. 5.2b illustrates a TA-PSF-encoded image of some tracer beads embedded in a hydrogel. Each '['-shaped TA-PSF is the image of a bead and the various two-lobe disparities indicate that they were at different depths. In fact, we can image through a thickness of 100 µm with a 20×, 0.5NA objective and about 40 µm with a 40×, 0.75NA objective. This is enough range to cover the size of most cells, even cell clusters within the hydrogel. Fig. 5.2c shows the 3D reconstructed tracer trajectories of mouse C2C12 cells from 48 to 60 hours. No significant displacement of the tracers has been observed at this stage, we reckon the following aspects may be the preclusion:

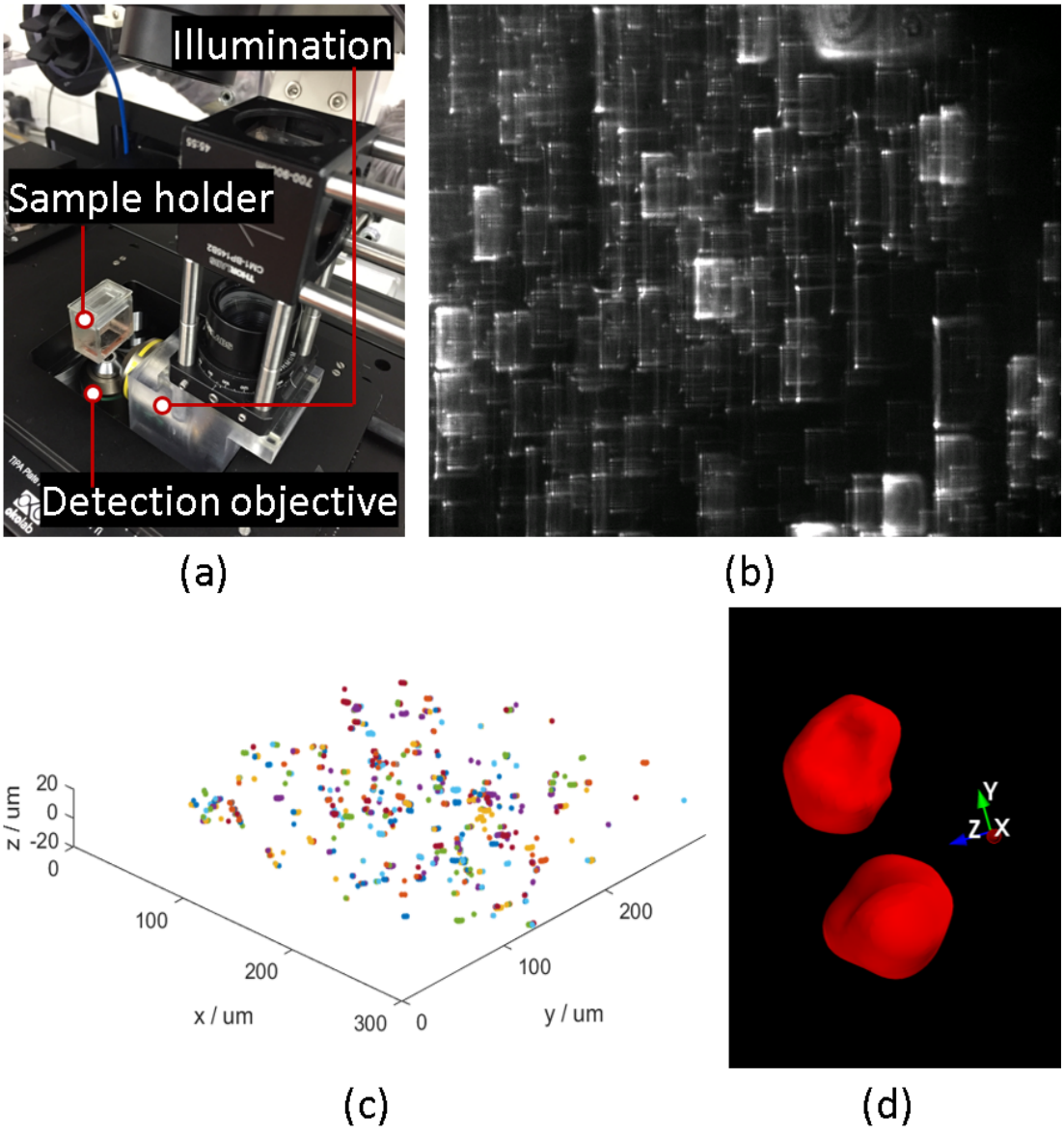

Fig. 5.2 Preliminary results of the tractio-force microscopy experiment. (a) The imaging configuration. (b) image of fluorescent beads embedded in the hydrogel. (c) 3D locations of the fluorescent beads. (d) light-sheet imaging of two nearby cells using SPIM.

- To avoid contamination, the lid of the sample holder was kept shut during the transportation of the sample between labs and during the whole imaging process. Thus the nutrition within the cell culture media may have run out, causing the C2C12 cells to be inactive.
- The stiffness of the hydrogel matrix affects the behavior of the cells inside. This gel may be too stiff for the cells to migrate or grow.
- The C2C12 cells do not migrate and grow as much as cells like cancer cells or fibroblast. It may be worth imaging a different type of cells.

Fig. 5.2d shows an image of the 3D reconstructed cell membranes obtained with the light-sheet imaging arm. As can be observed, the shapes of the cell membranes are well reconstructed which can be helpful for the determination of the 3D traction-force field.

To conclude, Airy-beam-based PSFs (or pupil-engineered PSFs in general) can potentially speed up the image acquisition of traction-force microscopy with higher precision measurement ($\sim$ 10nm) of the displacement field of the tracer beads. Combined with light-sheet microscopy, the cell membrane can also be imaged at a faster speed. This work is still ongoing, the preliminary results show that (1) The embedded tracer beads can be well imaged without obvious aberrations. (2) The tracer beads can be localized in 3D space in the presence of overlapping PSFs. (3) Imaging of cell membrane using light-sheet microscopy for TFM is also promising. We look forward to the demonstration of the first time-resolved TFM with engineered PSFs in the near future.

5.2.2 Extended-range single-molecule tracking and super resolution microscopy

There is also scope in considering the use of the Airy-beam-based PSFs for extended-range single-molecule tracking, or even localization-based super-resolution microscopy. These are the two main fields that engineered PSFs serve. The former has become a powerful tool to study fundamental biological dynamics such as folding and unfolding of proteins, protein-DNA interaction and dynamic processes on cell membranes[7]. The latter has enabled us to break the diffraction limit and super resolve 3D fine structures within cells that is impossible to resolve using conventional optical approaches.

Most existing techniques in these two fields as discussed in chapter 1 and chapter 3 (section 3.6.2) of this thesis suffer from a limited depth range of less than 3 µm for high magnification and high NA. This means that a molecule can not be tracked within large volumes (e.g. the whole volume of a cell, which is several microns thick) using conventional techniques; or in super-resolution microscopy, the cell needs to be scanned in focus to be imaged as a whole[127, 128]. The Airy-beam-based techniques provide more depth range than the DH-PSF, thus have potential for single-particle tracking over

extended depth range and 3D whole cell super-resolution microscopy. The main challenge remains in the very limited number of photons emitted from the single molecules. This is of less a problem for single-particle tracking as high quantum yield emitters like quantum dots have now been utilized for probing cell dynamics[129]. However, in super-resolution microscopy, only several thousand of photons can be collected from the standard dyes or antibodies. Nevertheless, CRLB simulations have shown great potential.

References

[1] M. G. L. Gustafsson, "Surpassing the lateral resolution limit by a factor of two using structured illumination microscopy," *Journal of Microscopy*, vol. 198, no. 2, pp. 82–87, 2000.

[2] M. J. Rust, M. Bates, and X. Zhuang, "Sub-diffraction-limit imaging by stochastic optical reconstruction microscopy (storm)," *Nat. Methods*, vol. 3, no. 10, pp. 793–796, 2006.

[3] E. Betzig, G. H. Patterson, R. Sougrat, O. W. Lindwasser, S. Olenych, J. S. Bonifacino, M. W. Davidson, J. Lippincott-Schwartz, and H. F. Hess, "Imaging intracellular fluorescent proteins at nanometer resolution," *Science*, vol. 313, no. 5793, pp. 1642–1645, 2006.

[4] E. B. Shera, N. K. Seitzinger, L. M. Davis, R. A. Keller, and S. A. Soper, "Detection of single fluorescent molecules," *Chem. Phys. Lett.*, vol. 174, no. 6, pp. 553 – 557, 1990.

[5] G. J. Schütz, G. Kada, V. P. Pastushenko, and H. Schindler, "Properties of lipid microdomains in a muscle cell membrane visualized by single molecule microscopy," *The EMBO journal*, vol. 19, no. 5, pp. 892–901, 2000.

[6] A. D. Douglass and R. D. Vale, "Single-molecule microscopy reveals plasma membrane microdomains created by protein-protein networks that exclude or trap signaling molecules in t cells," *Cell*, vol. 121, no. 6, pp. 937–950, 2005.

[7] H. Shen, L. J. Tauzin, R. Baiyasi, W. Wang, N. Moringo, B. Shuang, and C. F. Landes, "Single particle tracking: From theory to biophysical applications," *Chem. Rev.*, vol. 117, no. 11, pp. 7331–7376, 2017.

[8] D. R. Larson, W. R. Zipfel, R. M. Williams, S. W. Clark, M. P. Bruchez, F. W. Wise, and W. W. Webb, "Water-soluble quantum dots for multiphoton fluorescence imaging in vivo," *Science*, vol. 300, no. 5624, pp. 1434–1436, 2003.

[9] Y. Geng, P. Dalhaimer, S. Cai, R. Tsai, M. Tewari, T. Minko, and D. E. Discher, "Shape effects of filaments versus spherical particles in flow and drug delivery," *Nat. Nanotechnol.*, vol. 2, no. 4, p. 249, 2007.

[10] R. Lima, S. Wada, S. Tanaka, M. Takeda, T. Ishikawa, K.-i. Tsubota, Y. Imai, and T. Yamaguchi, "In vitro blood flow in a rectangular pdms microchannel: experimental observations using a confocal micro-piv system," *Biomed. Microdevices*, vol. 10, no. 2, pp. 153–167, 2008.

[11] W. R. Legant, J. S. Miller, B. L. Blakely, D. M. Cohen, G. M. Genin, and C. S. Chen, "Measurement of mechanical tractions exerted by cells in three-dimensional matrices," *Nat. Methods*, vol. 7, no. 12, pp. 969–971, 2010.

[12] S. Khetan, M. Guvendiren, W. R. Legant, D. M. Cohen, C. S. Chen, and J. A. Burdick, "Degradation-mediated cellular traction directs stem cell fate in covalently crosslinked three-dimensional hydrogels," *Nat. Mater.*, vol. 12, no. 5, p. 458, 2013.

[13] J. Westerweel, "Fundamentals of digital particle image velocimetry," *Meas. Sci. Technol.*, vol. 8, no. 12, p. 1379, 1997.

[14] A. K. Singh, E. B. Cummings, and D. J. Throckmorton, "Fluorescent liposome flow markers for microscale particle-image velocimetry," *Anal. Chem.*, vol. 73, no. 5, pp. 1057–1061, 2001.

[15] R. Lindken, M. Rossi, S. Große, and J. Westerweel, "Micro-particle image velocimetry (μpiv): recent developments, applications, and guidelines," *Lab Chip*, vol. 9, no. 17, pp. 2551–2567, 2009.

[16] S. R. P. Pavani and R. Piestun, "High-efficiency rotating point spread functions," *Opt. Express*, vol. 16, no. 5, pp. 3484–3489, 2008.

[17] S. Jia, J. C. Vaughan, and X. Zhuang, "Isotropic three-dimensional super-resolution imaging with a self-bending point spread function," *Nat. Photon.*, vol. 8, no. 4, pp. 302–306, 2014.

[18] S. G. Stanciu, G. A. Stanciu, and D. Coltuc, "Compensating light intensity attenuation in confocal scanning laser microscopy by histogram modeling methods," in *Digital Image Processing*, IntechOpen, 2012.

[19] M. Minsky, "Memoir on inventing the confocal scanning microscope," *Scanning*, vol. 10, no. 4, pp. 128–138, 1988.

[20] M. Eisele and B. Wolfring, "Next generation two-photon microscopy using the femtofiber ultra 920 fiber laser," application note, TOPTICA Photonics AG, Germany, 2019.

[21] W. Denk, J. Strickler, and W. Webb, "Two-photon laser scanning fluorescence microscopy," *Science*, vol. 248, no. 4951, pp. 73–76, 1990.

[22] C. Sheppard and M. Gu, "Image formation in two-photon fluorescence microcopy," *Optik*, vol. 86, no. 3, pp. 104–106, 1990.

[23] J. Huisken, J. Swoger, F. Del Bene, J. Wittbrodt, and E. H. K. Stelzer, "Optical sectioning deep inside live embryos by selective plane illumination microscopy," *Science*, vol. 305, no. 5686, pp. 1007–1009, 2004.

[24] A. H. Voie, D. H. Burns, and F. A. Spelman, "Orthogonal-plane fluorescence optical sectioning: Three-dimensional imaging of macroscopic biological specimens," *Journal of Microscopy*, vol. 170, no. 3, pp. 229–236, 1993.

[25] F. Pampaloni, B.-J. Chang, and E. H. K. Stelzer, "Light-sheet-based fluorescence microscopy (lsfm) for the quantitative imaging of cells and tissues," *Cell Tissue Res.*, vol. 360, no. 1, pp. 129–141, 2015.

[26] V. Zickus and J. M. Taylor, "3D + time blood flow mapping using spim-micropiv in the developing zebrafish heart," *Biomed. Opt. Express*, 2018.

[27] M. Speidel, A. Jonáš, and E.-L. Florin, "Three-dimensional tracking of fluorescent nanoparticles with subnanometer precision by use of off-focus imaging," *Opt. Lett.*, vol. 28, no. 2, pp. 69–71, 2003.

[28] M. Wu, J. W. Roberts, and M. Buckley, "Three-dimensional fluorescent particle tracking at micron-scale using a single camera," *Exp. Fluids*, vol. 38, no. 4, pp. 461–465, 2005.

[29] J. Park and K. Kihm, "Three-dimensional micro-ptv using deconvolution microscopy," *Exp. Fluids*, vol. 40, no. 3, p. 491, 2006.

[30] Z. Zhang and C.-H. Menq, "Three-dimensional particle tracking with subnanometer resolution using off-focus images," *Appl. Opt.*, vol. 47, no. 13, pp. 2361–2370, 2008.

[31] L. Gardini, M. Calamai, H. Hatakeyama, M. Kanzaki, M. Capitanio, and F. S. Pavone, "Three-dimensional tracking of quantum dot-conjugated molecules in living cells," in *Nanoscale Imaging*, pp. 425–448, Springer, 2018.

[32] R. S. W. E. S. Prabhat, P. and R. J. Ober, "Simultaneous imaging of different focal planes in fluorescence microscopy for the study of cellular dynamics in three dimensions," *IEEE T. Nanobiosci.*, vol. 3, no. 4, pp. 237–242, 2004.

[33] S. Ram, J. Chao, P. Prabhat, E. S. Ward, and R. J. Ober, "A novel approach to determining the three-dimensional location of microscopic objects with applications to 3D particle tracking," *Proc. SPIE*, vol. 6443, pp. 64430D–64430D–7, 2007.

[34] R. Velmurugan, J. Chao, S. Ram, E. S. Ward, and R. J. Ober, "Intensity-based axial localization approaches for multifocal plane microscopy," *Opt. Express*, vol. 25, no. 4, pp. 3394–3410, 2017.

[35] S. Ram, P. Prabhat, J. Chao, E. S. Ward, and R. J. Ober, "High accuracy 3D quantum dot tracking with multifocal plane microscopy for the study of fast intracellular dynamics in live cells," *Biophys. J.*, vol. 95, no. 12, pp. 6025–6043, 2008.

[36] M. F. Juette, T. J. Gould, M. D. Lessard, M. J. Mlodzianoski, B. S. Nagpure, B. T. Bennett, S. T. Hess, and J. Bewersdorf, "Three-dimensional sub-100 nm resolution fluorescence microscopy of thick samples," *Nat. Methods*, vol. 5, pp. 527–529, 2008.

[37] A. Tahmasbi, S. Ram, J. Chao, A. V. Abraham, F. W. Tang, E. S. Ward, and R. J. Ober, "Designing the focal plane spacing for multifocal plane microscopy," *Opt. Express*, vol. 22, no. 14, pp. 16706–16721, 2014.

[38] B. Huang, W. Wang, M. Bates, and X. Zhuang, "Three-dimensional super-resolution imaging by stochastic optical reconstruction microscopy," *Science*, vol. 319, no. 5864, pp. 810–813, 2008.

[39] H. P. Kao and A. S. Verkman, "Tracking of single fluorescent particles in three dimensions: use of cylindrical optics to encode particle position," *Biophys. J.*, vol. 67, no. 3, pp. 1291–1300, 1994.

[40] L. Holtzer, T. Meckel, and T. Schmidt, "Nanometric three-dimensional tracking of individual quantum dots in cells," *Appl. Phys. Lett.*, vol. 90, no. 5, p. 053902, 2007.

[41] S. Chen, N. Angarita-Jaimes, D. Angarita-Jaimes, B. Pelc, A. H. Greenaway, C. E. Towers, D. Lin, and D. P. Towers, "Wavefront sensing for three-component three-dimensional flow velocimetry in microfluidics," *Exp. Fluids*, vol. 47, no. 4, pp. 849–863, 2009.

[42] C. Cierpka and C. J. Kähler, "Particle imaging techniques for volumetric three-component (3D3C) velocity measurements in microfluidics," *J. Vis.*, vol. 15, no. 1, pp. 1–31, 2012.

[43] C.-H. Lien, C.-Y. Lin, S.-J. Chen, and F.-C. Chien, "Dynamic particle tracking via temporal focusing multiphoton microscopy with astigmatism imaging," *Opt. Express*, vol. 22, no. 22, pp. 27290–27299, 2014.

[44] L. Zhao, Y. Zhong, Y. Wei, N. Ortiz, F. Chen, and G. Wang, "Microscopic movement of slow-diffusing nanoparticles in cylindrical nanopores studied with three-dimensional tracking," *Anal. Chem.*, vol. 88, no. 10, pp. 5122–5130, 2016.

[45] Y. Ichikawa, K. Yamamoto, and M. Motosuke, "Three-dimensional flow velocity and wall shear stress distribution measurement on a micropillar-arrayed surface using astigmatism ptv to understand the influence of microstructures on the flow field," *Microfluid. and Nanofluid.*, vol. 22, no. 7, p. 73, 2018.

[46] F. C. Zanacchi, Z. Lavagnino, M. P. Donnorso, A. Del Bue, L. Furia, M. Faretta, and A. Diaspro, "Live-cell 3D super-resolution imaging in thick biological samples," *Nat. Methods*, vol. 8, no. 12, p. 1047, 2011.

[47] W. R. Legant, L. Shao, J. B. Grimm, T. A. Brown, D. E. Milkie, B. B. Avants, L. D. Lavis, and E. Betzig, "High-density three-dimensional localization microscopy across large volumes," *Nat. Methods*, vol. 13, no. 4, p. 359, 2016.

[48] J. S. Biteen, E. D. Goley, L. Shapiro, and W. Moerner, "Three-dimensional super-resolution imaging of the midplane protein ftsz in live caulobacter crescentus cells using astigmatism," *ChemPhysChem*, vol. 13, no. 4, pp. 1007–1012, 2012.

[49] H. Wang and P. Zhao, "Tracking microparticle motions in three-dimensional flow around a microcubic array fabricated on the wall surface," *Microfluid. and Nanofluid.*, vol. 22, no. 3, p. 30, 2018.

[50] C. E. Willert and M. Gharib, "Three-dimensional particle imaging with a single camera," *Exp. Fluids*, vol. 12, no. 6, pp. 353–358, 1992.

[51] F. Pereira, M. Gharib, D. Dabiri, and D. Modarress, "Defocusing digital particle image velocimetry: a 3-component 3-dimensional dpiv measurement technique. application to bubbly flows," *Exp. Fluids*, vol. 29, no. 1, pp. S078–S084, 2000.

[52] F. Pereira and M. Gharib, "Defocusing digital particle image velocimetry and the three-dimensional characterization of two-phase flows," *Meas. Sci. Technol.*, vol. 13, no. 5, pp. 683–694, 2002.

[53] S. Y. Yoon and K. C. Kim, "3D particle position and 3D velocity field measurement in a microvolume via the defocusing concept," *Meas. Sci. Technol.*, vol. 17, no. 11, pp. 2897–2905, 2006.

[54] F. Kiebert, J. König, C. Kykal, and H. Schmidt, "Measurements of streams agitated by fluid loaded saw-devices using a volumetric 3-component measurement technique (v3v)," *Phys. Procedia*, vol. 70, pp. 25–29, 2015.

[55] V. A. Troutman and J. O. Dabiri, "Single-camera three-dimensional tracking of natural particulate and zooplankton," *Meas. Sci. Technol.*, vol. 29, no. 7, p. 075401, 2018.

[56] S. R. P. Pavani, M. A. Thompson, J. S. Biteen, S. J. Lord, N. Liu, R. J. Twieg, R. Piestun, and W. E. Moerner, "Three-dimensional, single-molecule fluorescence imaging beyond the diffraction limit by using a double-helix point spread function," *Proc. Natl. Acad. Sci. U.S.A.*, vol. 106, no. 9, pp. 2995–2999, 2009.

[57] A. Greengard, Y. Y. Schechner, and R. Piestun, "Depth from diffracted rotation," *Opt. Lett.*, vol. 31, no. 2, pp. 181–183, 2006.

[58] G. Grover, S. Quirin, C. Fiedler, and R. Piestun, "Photon efficient double-helix psf microscopy with application to 3D photo-activation localization imaging," *Biomed. Opt. Express*, vol. 2, no. 11, pp. 3010–3020, 2011.

[59] M. D. Lew, S. F. Lee, M. Badieirostami, and W. E. Moerner, "Corkscrew point spread function for far-field three-dimensional nanoscale localization of pointlike objects," *Opt. Lett.*, vol. 36, no. 2, pp. 202–204, 2011.

[60] G. Grover, K. DeLuca, S. Quirin, J. DeLuca, and R. Piestun, "Super-resolution photon-efficient imaging by nanometric double-helix point spread function localization of emitters (spindle)," *Opt. Express*, vol. 20, no. 24, pp. 26681–26695, 2012.

[61] R. Berlich and S. Stallinga, "High-order-helix point spread functions for monocular three-dimensional imaging with superior aberration robustness," *Opt. Express*, vol. 26, no. 4, pp. 4873–4891, 2018.

[62] Y. Sun, J. D. McKenna, J. M. Murray, E. M. Ostap, and Y. E. Goldman, "Parallax: High accuracy three-dimensional single molecule tracking using split images," *Nano Lett.*, vol. 9, no. 7, pp. 2676–2682, 2009.

[63] J. Yajima, K. Mizutani, and T. Nishizaka, "A torque component present in mitotic kinesin Eg5 revealed by three-dimensional tracking," *Nat. Struct. Mol. Biol.*, vol. 15, no. 10, pp. 1119–1121, 2008.

[64] A. S. Backer, M. P. Backlund, A. R. Von Diezmann, S. J. Sahl, and W. E. Moerner, "A bisected pupil for studying single-molecule orientational dynamics and its application to three-dimensional super-resolution microscopy," *Appl. Phys. Lett.*, vol. 104, no. 19, pp. 161103–7150, 2014.

[65] Y. Zhou, P. Zammit, G. Carles, and A. R. Harvey, "Computational localization microscopy with extended axial range," *Opt. Express*, vol. 26, no. 6, pp. 7563–7577, 2018.

[66] Y. Zhou, V. Zickus, P. Zammit, J. M. Taylor, and A. R. Harvey, "High-speed extended-volume blood flow measurement using engineered point-spread functions," *Biomed. Opt. Express*, vol. 9, no. 11, 2018.

[67] M. V. Berry and N. L. Balazs, "Nonspreading wave packets," *Am. J. Phys.*, vol. 47, no. 3, pp. 264–267, 1979.

[68] G. A. Siviloglou, J. Broky, A. Dogariu, and D. N. Christodoulides, "Observation of accelerating airy beams," *Phys. Rev. Lett.*, vol. 99, p. 213901, 2007.

[69] S. Quirin, S. R. P. Pavani, and R. Piestun, "Optimal 3D single-molecule localization for superresolution microscopy with aberrations and engineered point spread functions," *Proc. Natl. Acad. Sci. U.S.A.*, vol. 109, no. 3, pp. 675–679, 2012.

[70] J. Chao, E. S. Ward, and R. J. Ober, "Fisher information theory for parameter estimation in single molecule microscopy: tutorial," *J. Opt. Soc. Am. A*, vol. 33, no. 7, pp. B36–B57, 2016.

[71] J. Schnitzbauer, R. McGorty, and B. Huang, "4Pi fluorescence detection and 3D particle localization with a single objective," *Opt. Express*, vol. 21, no. 17, pp. 19701–19708, 2013.

[72] Y. Shechtman, L. E. Weiss, A. S. Backer, S. J. Sahl, and W. E. Moerner, "Precise three-dimensional scan-free multiple-particle tracking over large axial ranges with tetrapod point spread functions," *Nano Lett.*, vol. 15, no. 6, pp. 4194–4199, 2015.

[73] Y. Shechtman, S. J. Sahl, A. S. Backer, and W. E. Moerner, "Optimal point spread function design for 3D imaging," *Phys. Rev. Lett.*, vol. 113, p. 133902, 2014.

[74] K. Adelsberger, *Design guidelines for wavefront coding in broadband optical systems*. PhD thesis, University of Rochester, 2014.

[75] P. Zammit, *Extended depth-of-field imaging and ranging in microscopy*. PhD thesis, University of Glasgow, 2016.

[76] B. M. Hanser, M. G. L. Gustafsson, D. A. Agard, and J. W. Sedat, "Phase retrieval for high-numerical-aperture optical systems," *Opt. Lett.*, vol. 28, no. 10, pp. 801–803, 2003.

[77] C. W. McCutchen, "Generalized aperture and the three-dimensional diffraction image," *J. Opt. Soc. Am.*, vol. 54, no. 2, pp. 240–244, 1964.

[78] E. R. Dowski and W. T. Cathey, "Extended depth of field through wave-front coding," *Appl. Opt.*, vol. 34, no. 11, pp. 1859–1866, 1995.

[79] W. T. Cathey and E. R. Dowski, "New paradigm for imaging systems," *Appl. Opt.*, vol. 41, no. 29, pp. 6080–6092, 2002.

[80] G. A. Siviloglou and D. N. Christodoulides, "Accelerating finite energy airy beams," *Opt. Lett.*, vol. 32, no. 8, pp. 979–981, 2007.

[81] P. Zammit, A. R. Harvey, and G. Carles, "Extended depth-of-field imaging and ranging in a snapshot," *Optica*, vol. 1, no. 4, pp. 209–216, 2014.

[82] J. W. Goodman, *Introduction to Fourier Optics*. McGraw-Hill, 1996.

[83] Y. Wu, L. Dong, Y. Zhao, M. Liu, X. Chu, W. Jia, X. Guo, and Y. Feng, "Analysis of wavefront coding imaging with cubic phase mask decenter and tilt," *Appl. Opt.*, vol. 55, no. 25, pp. 7009–7017, 2016.

[84] B. Shuang, J. Chen, L. Kisley, and C. F. Landes, "Troika of single particle tracking programing: Snr enhancement, particle identification, and mapping," *Phys. Chem. Chem. Phys.*, vol. 16, no. 2, pp. 624–634, 2014.

[85] K. Jaqaman, D. Loerke, M. Mettlen, H. Kuwata, S. Grinstein, S. L. Schmid, and G. Danuser, "Robust single-particle tracking in live-cell time-lapse sequences," *Nat. Methods*, vol. 5, no. 8, pp. 695–702, 2008.

[86] J. C. Crocker and D. G. Grier, "Methods of digital video microscopy for colloidal studies," *J. Colloid Interf. Sci.*, vol. 179, no. 1, pp. 298–310, 1996.

[87] J. Štigler, "Analytical velocity profile in tube for laminar and turbulent flow," *Engineer. Mechan.*, vol. 21, no. 6, pp. 371–379, 2014.

[88] G. Muyo and A. R. Harvey, "Decomposition of the optical transfer function: wavefront coding imaging systems.," *Opt. Lett.*, vol. 30, no. 20, pp. 2715–2717, 2005.

[89] G. A. Siviloglou, J. Broky, A. Dogariu, and D. N. Christodoulides, "Ballistic dynamics of airy beams," *Opt. Lett.*, vol. 33, no. 3, pp. 207–209, 2008.

[90] A. V. Abraham, S. Ram, J. Chao, E. S. Ward, and R. J. Ober, "Quantitative study of single molecule location estimation techniques," *Opt. Express*, vol. 17, no. 26, pp. 23352–23373, 2009.

[91] J. R. Hove, R. W. Köster, A. S. Forouhar, G. Acevedo-Bolton, S. E. Fraser, and M. Gharib, "Intracardiac fluid forces are an essential epigenetic factor for embryonic cardiogenesis," *Nature*, vol. 421, no. 6919, pp. 172–177, 2003.

[92] R. A. Jamison, C. R. Samarage, R. J. Bryson-Richardson, and A. Fouras, "In Vivo Wall Shear Measurements within the Developing Zebrafish Heart," *PLoS ONE*, vol. 8, no. 10, p. e75722, 2013.

[93] A. S. Forouhar, M. Liebling, A. Hickerson, A. Nasiraei-Moghaddam, H.-J. Tsai, J. R. Hove, S. E. Fraser, M. E. Dickinson, and M. Gharib, "The embryonic vertebrate heart tube is a dynamic suction pump," *Science*, vol. 312, no. 5774, pp. 751–753, 2006.

[94] S. K. Ramasamy, A. P. Kusumbe, M. Schiller, D. Zeuschner, M. G. Bixel, C. Milia, J. Gamrekelashvili, A. Limbourg, A. Medvinsky, M. M. Santoro, F. P. Limbourg, and R. H. Adams, "Blood flow controls bone vascular function and osteogenesis," *Nat Commun.*, vol. 7, no. 13601, pp. 1–13, 2016.

[95] S. Korzh, X. Pan, M. Garcia-Lecea, C. L. Winata, X. Pan, T. Wohland, V. Korzh, and Z. Gong, "Requirement of vasculogenesis and blood circulation in late stages of liver growth in zebrafish," *BMC Dev. Biol.*, vol. 8, no. 84, pp. 1–15, 2008.

[96] S. C. Watkins, S. Maniar, M. Mosher, B. L. Roman, M. Tsang, and C. M. St Croix, "High Resolution Imaging of Vascular Function in Zebrafish," *PLoS ONE*, vol. 7, no. 8, p. e44018, 2012.

[97] M. A. Mintun, B. N. Lundstrom, A. Z. Snyder, A. G. Vlassenko, G. L. Shulman, and M. E. Raichle, "Blood flow and oxygen delivery to human brain during functional activity: Theoretical modeling and experimental data," *Proc. Natl. Acad. Sci. U.S.A.*, vol. 98, no. 12, pp. 6859–6864, 2001.

[98] A. K. Dunn, H. Bolay, M. A. Moskowitz, and D. A. Boas, "Dynamic imaging of cerebral blood flow using laser speckle," *J. Cereb. Blood Flow Metab.*, vol. 21, no. 3, pp. 195–201, 2001.

[99] M. Fujishima, S. Ibayashi, K. Fujii, and S. Mori, "Cerebral blood flow and brain function in hypertension," *Hypertens. Res.*, vol. 18, no. 2, pp. 111–117, 1995.

[100] X. Pan, H. Yu, X. Shi, V. Korzh, and T. Wohland, "Characterization of flow direction in microchannels and zebrafish blood vessels by scanning fluorescence correlation spectroscopy," *J. Biomed. Opt.*, vol. 12, no. 1, p. 014034, 2007.

[101] X. Pan, X. Shi, V. Korzh, H. Yu, and T. Wohland, "Line scan fluorescence correlation spectroscopy for three-dimensional microfluidic flow velocity measurements," *J. Biomed. Opt.*, vol. 14, no. 2, p. 024049, 2009.

[102] X. Shi, L. S. Teo, X. Pan, S. W. Chong, R. Kraut, V. Korzh, and T. Wohland, "Probing events with single molecule sensitivity in zebrafish and Drosophila embryos by fluorescence correlation spectroscopy," *Dev. Dyn.*, vol. 238, no. 12, pp. 3156–3167, 2009.

[103] L. Fieramonti, E. A. Foglia, S. Malavasi, C. D'Andrea, G. Valentini, F. Cotelli, and A. Bassi, "Quantitative measurement of blood velocity in zebrafish with optical vector field tomography," *J. Biophotonics*, vol. 8, no. 1-2, pp. 52–59, 2015.

[104] M. P. Craig, S. D. Gilday, D. Dabiri, and J. R. Hove, "An Optimized Method for Delivering Flow Tracer Particles to Intravital Fluid Environments in the Developing Zebrafish," *Zebrafish*, vol. 9, no. 3, pp. 108–119, 2012.

[105] J. Lu, F. Pereira, S. E. Fraser, and M. Gharib, "Three-dimensional real-time imaging of cardiac cell motions in living embryos.," *J. Biomed. Opt.*, vol. 13, no. 1, p. 014006, 2010.

[106] F. Pereira and M. Gharib, "Defocusing digital particle image velocimetry and the three-dimensional characterization of two-phase flows," *Meas. Sci. Technol.*, vol. 13, no. 5, p. 683, 2002.

[107] E. J. Gualda, T. Vale, P. Almada, J. A. Feijó, G. G. Martins, and N. Moreno, "Openspinmicroscopy: An open-source integrated microscopy platform," *Nat. Methods*, vol. 10, no. 7, pp. 599–600, 2013.

[108] C. B. Kimmel, "Genetics and early development of zebrafish," *Trends Genet.*, vol. 5, pp. 283 – 288, 1989.

[109] K. N. Wallace, S. Akhter, E. M. Smith, K. Lorent, and M. Pack, "Intestinal growth and differentiation in zebrafish," *Mech. Dev.*, vol. 122, no. 2, pp. 157 – 173, 2005.

[110] F. R. Khan and S. S. Alhewairini, *Zebrafish (Danio rerio) as a Model Organism*. IntechOpen, 2018.

[111] G. J. Lieschke and P. D. Currie, "Animal models of human disease: zebrafish swim into view," *Nat. Rev. Genet.*, vol. 8, pp. 353–367, 2007.

[112] G. Kari, U. Rodeck, and A. P. Dicker, "Zebrafish: An emerging model system for human disease and drug discovery," *Clin. Pharmacol. Ther.*, vol. 82, no. 1, pp. 70–80, 2007.

[113] E. Hendel, "Zebrafish developmental stages." https://commons.wikimedia.org/wiki/File:Zebrafish_Developmental_Stages.tiff. Accessed: 2019-07-11.

[114] S. Gilbert, "Zebrafish help researchers study human genes." https://news.psu.edu/story/418819/2016/07/28/research/zebrafish-help-researchers-study-human-genes. Accessed: 2019-07-11.

[115] R. N. Kettleborough, E. M. Busch-Nentwich, S. A. Harvey, C. M. Dooley, E. De Bruijn, F. Van Eeden, I. Sealy, R. J. White, C. Herd, I. J. Nijman, F. Fényes, S. Mehroke, C. Scahill, R. Gibbons, N. Wali, S. Carruthers, A. Hall, J. Yen, E. Cuppen, and D. L. Stemple, "A systematic genome-wide analysis of zebrafish protein-coding gene function," *Nature*, 2013.

[116] J. Karlsson, J. von Hofsten, and P.-E. Olsson, "Generating transparent zebrafish: A refined method to improve detection of gene expression during embryonic development," *Mar. Biotechnol.*, vol. 3, no. 6, pp. 522–527, 2001.

[117] J. C. Crocker and D. G. Grier, "Methods of digital video microscopy for colloidal studies," *J. Colloid Interf. Sci.*, vol. 179, no. 1, pp. 298 – 310, 1996.

[118] Q. Chen, L. Jiang, C. Li, D. Hu, J.-w. Bu, D. Cai, and J.-l. Du, "Haemodynamics-driven developmental pruning of brain vasculature in zebrafish," *PLoS Biol.*, vol. 10, pp. 1–18, 2012.

[119] J. Steinwachs, C. Metzner, K. Skodzek, N. Lang, I. Thievessen, C. Mark, S. Münster, K. E. Aifantis, and B. Fabry, "Three-dimensional force microscopy of cells in biopolymer networks," *Nat. Methods*, vol. 13, no. 2, pp. 171–176, 2016.

[120] S. J. Baek and S. J. Lee, "A new two-frame particle tracking algorithm using match probability," *Exp. Fluids*, vol. 22, no. 1, pp. 23–32, 1996.

[121] D. Li, Y. Zhang, Y. Sun, and W. Yan, "A multi-frame particle tracking algorithm robust against input noise," *Meas. Sci. Technol.*, vol. 19, no. 10, p. 105401, 2008.

[122] B. A. Nerger, M. J. Siedlik, and C. M. Nelson, "Microfabricated tissues for investigating traction forces involved in cell migration and tissue morphogenesis," *Cell. Mol. Life Sci.*, vol. 74, no. 10, pp. 1819–1834, 2017.

[123] H. Colin-York, C. Eggeling, and M. Fritzsche, "Dissection of mechanical force in living cells by super-resolved traction force microscopy," *Nat. Protoc.*, vol. 12, 2017.

[124] M. Dembo and Y. L. Wang, "Stresses at the cell-to-substrate interface during locomotion of fibroblasts," *Biophys. J.*, vol. 76, no. 4, pp. 2307–2316, 1999.

[125] I. Albert-Smet, A. Marcos-Vidal, J. J. Vaquero, M. Desco, A. Muñoz-Barrutia, and J. Ripoll, "Applications of light-sheet microscopy in microdevices," *Front. Neuroanat.*, vol. 13, p. 1, 2019.

[126] K. M. Dean, P. Roudot, E. S. Welf, G. Danuser, and R. Fiolka, "Deconvolution-free subcellular imaging with axially swept light sheet microscopy," *Biophys. J.*, vol. 108, no. 12, pp. 2807 – 2815, 2015.

[127] B. Hajj, J. Wisniewski, M. El Beheiry, J. Chen, A. Revyakin, C. Wu, and M. Dahan, "Whole-cell, multicolor superresolution imaging using volumetric multifocus microscopy," *Proc. Natl. Acad. Sci. U.S.A.*, vol. 111, no. 49, pp. 17480–17485, 2014.

[128] A. R. Carr, A. Ponjavic, S. Basu, J. McColl, A. M. Santos, S. Davis, E. D. Laue, D. Klenerman, and S. F. Lee, "Three-dimensional super-resolution in eukaryotic cells using the double-helix point spread function," *Biophys. J.*, vol. 112, no. 7, pp. 1444 – 1454, 2017.

[129] K. Baba and K. Nishida, "Single-molecule tracking in living cells using single quantum dot appli-cations," *Theranostics*, vol. 2, no. 7, pp. 655–667, 2012.